Effect of Point and Line Defects on the Mechanical Behavior of Single Layer $MoTe_2$

A thesis presented to the Department of Mechanical and Production Engineering, Islamic University of Technology in partial fulfilment of the requirement for the award of the degree of Bachelor of science in Mechanical Engineering

Submitted By

Md. Jobayer Aziz (180011216)

Supervised By

Dr. Md. Rezwanul Karim

Islamic University of Technology

Department of Mechanical and Production Engineering

May, 2023

CANDIDATE'S DECLARATION

The presented thesis titled **"Effect of Point and Line Defects on the Mechanical Behavior of Single Layer $MoTe_2$"** authored by Md. Jobayer Aziz (180011216) serves as an authentic and comprehensive account of the research conducted to fulfill the academic requirements for the degree of B.Sc. in Mechanical Engineering at the Islamic University of Technology in Gazipur, Dhaka. The study was carried out under the expert guidance of Dr. Md. Rezwanul Karim, Associate Professor in the Department of Mechanical and Production Engineering (MPE) at IUT.

The content presented in the thesis has not been previously submitted, either partially or in its entirety, to any other institution for the purpose of obtaining any degree.

_____

Md. Jobayer Aziz

180011216

RECOMMENDATION OF BOARD OF EXAMINERS

The thesis titled “Effect of Point and Line Defects on the Mechanical Behavior of Single Layer $MoTe_2$” submitted by Md. Jobayer Aziz (180011216) , has been accepted as satisfactory in partial fulfillment of the requirements for the degree of B.Sc. in Mechanical Engineering on 18th May, 2023.

1. _____

Dr. Md. Rezwanul Karim (Supervisor)

Associate Professor

MPE Dept., IUT, Board Bazar, Gazipur-1704, Bangladesh.

2. _____

Dr. Arafat Ahmed Bhuiyan

Associate Professor

MPE Dept., IUT, Board Bazar, Gazipur-1704, Bangladesh.

3. _____

Dr. Mohammad Monjurul Ehsan

Associate Professor

MPE Dept., IUT, Board Bazar, Gazipur-1704, Bangladesh.

ACKNOWLEDGEMENT

I am deeply grateful to **Allah (SWT)** for His blessings and guidance throughout my research journey, enabling me to successfully complete this thesis. I extend my sincere appreciation to the Department of Mechanical and Production Engineering at the Islamic University of Technology, Bangladesh, for providing me with the opportunity and support to undertake this research.

I am thankful for the guidance, expertise, and unwavering support of my supervisor, **Dr. Md. Rezwanul Karim**, Associate Professor in the Department of Mechanical and Production Engineering at the Islamic University of Technology, Bangladesh. His invaluable contributions have been instrumental in shaping this research. I would also like to express my sincere appreciation to **Dr. Arafat Ahmed Bhuiyan**, Associate Professor in the same department, for their valuable insights and contributions to this thesis.

I am grateful to **Akibul Islam**, a PhD Candidate at the Nanomechanics and Materials Lab, University of Toronto, for his collaborative effort and guidance and **Dr. Jin-Wu Jiang**, Professor at the Shanghai Institute of Applied Mathematics and Mechanics, Shanghai University for enriching contributions to this research.

Lastly, I extend my appreciation to my parents. Their constant belief in my abilities have been invaluable to me. I would also like to thank my friends for their unwavering support and encouragement throughout this rewarding journey. Their collective effort and inspiration have been instrumental in the successful completion of this research.

ABSTRACT

Following the groundbreaking discovery of graphene, the scientific community has witnessed a surge of interest in two-dimensional (2D) materials during recent times, remarkable capabilities and versatility for technological applications. Apart from graphene, a lot of promising work has been reported from other two-dimensional materials, including boron nitrides (like hBN, or "white graphite"), dichalcogenides (like MoS_2), silicene, germanane, stanene, etc. To use these materials successfully in nanodevices and systems, it is important to figure out their elastic and mechanical properties. This will help define the limits of useful applications for flexible electronics. Two typical computational techniques for atomically thin models like 2D materials are molecular dynamics and density functional theory. Using the concepts of classical mechanics, molecular dynamics mimics the motion of atoms and molecules in a complicated system. In this study, the effect of point and line defects on the 2D transition metal dichalcogenides (TMDs) namely molybdenum ditelluride ($MoTe_2$) were investigated using the Sandia National Laboratory's Molecular Dynamics Program LAMMPS. Three distinct types of point defect structures were investigated: a 2-tellurium vacancy structure, a 4-tellurium vacancy structure, and a 6-tellurium vacancy accompanied by a 1-molybdenum vacancy structure. Line defects were placed along armchair axis and zigzag axis. We characterized their mechanical characteristics, including axial stiffness, ultimate strength, and ultimate strain, as well as their thermal behavior at temperatures ranging from 1 Kelvin to 600 Kelvin, using atomistic computational techniques.

TABLE OF CONTENTS

TABLE OF FIGURES

LIST OF TABLES

NOMENCLATURE

LAMMPS	Large atomic/molecular massive parallel simulator
MD	Molecular Dynamics
TMDs	Transition metal dichalcogenides
GPU	Graphics processing unit
CPU	Central processing unit
$MoTe_2$	Molybdenum ditelluride
MoS_2	Molybdenum disulfide
AFM	Atomic force microscopy
SEM	Scanning electron microscope
NEMS	Nanoelectromechanical systems
TEM	Transmission Electron Microscopy
UTS	Ultimate tensile stress
MPI	Message-passing library
Atomsk	Visualization for electronic and structural analysis
VESTA	Atom, Molecule, Material Software Kit
FET	Field Effect Transistor

AFM	Atomic Force Microscopy
CAFM	Current Atomic Force Microscopy
ML	Monolayer
DG	Double Gate
KS	Kohn-Sham
HKS	Hohenberg-Kohn-Sham
DFT	Density Functional Theory
KSDFT	Kohn-Sham Density Functional Theory
OFDFT	Orbital-Free Density Functional Theory
LDA	Local Density Approximation
UFF	Universal Force Field
CHARMM	Chemistry at Harvard Macromolecular Mechanics
AMBER	Assisted Model Building with Energy Refinement
GROMOS	Groningen Molecular Simulation
OPLS	Optimized Potentials for Liquid Simulations
COMPASS	Condensed Phase Optimized Molecular Potentials for Atomistic Simulation Studies
Y_m	Young's Modulus
UTS	Ultimate Tensile Strength

FS	Fracture Strain

SYMBOLS

$L_x - Instraneous\ length\ along\ x\ axis$

$L_{x0} - Instraneous\ length\ along\ x\ axis\ before\ deformation$

$L_y - Instraneous\ length\ along\ y\ axis$

$L_{y0} - Instraneous\ length\ along\ x\ axis\ before\ deformation$

$L_z - Instraneous\ length\ along\ z\ axis$

$L_{zo} - Instraneous\ length\ along\ z\ axis\ before\ deformation$

$P_{xx} - Tensile\ Load$

$\sigma - Stress$

$\varepsilon - Strain$

$\Omega - Summation\ of\ total\ volume\ occupied\ by\ atoms$

$r_{ij} - Reference\ Position\ of\ i\ atom\ with\ respect\ to\ j$

$\otimes - Cross\ Product$

$f_{ij} - Interatomic\ Force\ on\ i\ atom\ exerted\ by\ j\ atom$

$r_{max}, r_{maxij}, r_{maxik} - Cutoff\ Ratios$

$\theta_0 - Angle\ between\ two\ bonds\ at\ equilibrium\ position$

$\phi - One\ of\ the\ constituents\ of\ virial\ stress$

$V_2, V_3 - Two\ body\ angle\ bending\ and\ bond\ stretching\ terms$

$A - Energy\ Parameter$

$K - \ Energy\ Parameter$

CHAPTER 1 : INTRODUCTION

1.1. Two Dimensional Materials and Transition Metal Dichalcogenides

Two-dimensional (2D) materials are crystalline substances that only have one or a few layers of atoms. The exceptional properties and distinctive structure of 2D materials have made them the subject of significant interest. 2D materials exhibit a wide spectrum of traits, including superconductivity, mechanical flexibility, high carrier mobilities, strong thermal conductivity, favorable optical properties, and effective UV absorption [1].The mechanical strength of 2D materials is one of their numerous desirable properties. It is of great interest to investigate possible new applications that involve a coupling between mechanical and electronic properties [2].Since the breakthrough of graphene, the number of 2D materials has expanded to encompass over a thousand distinct substances. In general, there are four distinct classes of 2D materials (graphene family, chalcogenides, xenes and 2D oxides) [3].

The exceptional qualities of graphene have prompted a burgeoning interest in the exploration of additional 2D nanomaterials that can enhance and complement its properties. While graphene has semi-metallic characteristics, the development of semiconducting and insulating 2D materials with comparable structural properties is crucial for their integration into nanoelectronic devices. In recent years, semiconducting 2D materials such as single layer transition metal dichalcogenides (TMDs), including MoS_2, WS_2, $MoSe_2$, and WSe_2, have been discovered. Since TMDs are so unusual in their mechanical, optical and electrical features, they have attracted a lot of research interest [4]. Two-dimensional nanostructures with atomic-scale layers may display intriguing new characteristics that are at odds with their bulk parent substances. Both theoretical and experimental findings agree that 2D semiconductors possess unique characteristics that might lead to significant advances in nanotechnology [5].

1.2. Background and Motivation

Semiconductors are found in all sort of electronic devices ranging from small LED to large supercomputers. Silicon stands out as one of the commonly utilized semiconductor materials [6]. However due to the global scarcity of silicon researchers are looking for alternatives [7]. MoS_2,

$MoTe_2$ and other 2D-TMD materials can be possible replacements for amorphous silicon in low-cost flexible electronics [8]. Considering the high cost and limited availability of platinum, researchers have looked at other materials to provide low-priced platinum-free counter electrodes. Alternative counter electrodes based on abundantly found 2D TMDs like, WS_2, , FeS_2, CoS_2 ,FeS_2, TiS_2, NiS_2, $MoSe_2$, $TaSe_2$, $NbSe_2$, $NiSe_2$, CoS_2, MoS_2, SnS_2, Bi_2Se_3 have shown prospect for making low-cost Pt-free DSSCs (Dye-sensitized solar cells). [9]. A distinguishing characteristic of monolayer $MoTe_2$ is its minimal energy barrier between semiconducting and metallic 2H and 1T' phases respectively, setting it apart from other Mo- and W-based TMDs [10]. But for using these materials in electronic devices, it is imperative to figure out their mechanical properties.

1.3. Defect Engineering

Some 2D materials may have intrinsic faults, while others may have extrinsic defects like foreign atoms. In this context, defects are mainly classified based on their dimensional characteristics, with zero-dimensional defects (including adatoms, Stone-Wales defects, impurities, and vacancy) and one dimensional defects constituting the majority of the defect types (line defect ,edges and GBs) [11]. They can happen by accident or on purpose during the process of making something. During simulations of molecular statics and dynamics, these flaws are made by taking atoms out of the 2D structure [12]. Defects have a major role in dictating the fracture behavior of two-dimensional materials. Substantially lower failure stress is required to break 2D materials with defects than it would for defect-free pristine structure for the same material. Uniaxial tensile test on defective 2D materials helps us to learn more about the failure process [13].

1.4. Scopes and Current Problem

Knowing how 2D materials behave mechanically is crucial for using them in new nanodevices and for assessing their serviceability limits of promising applications like flexible electronics. Having a comprehensive knowledge of the mechanical characteristics of a material enables us to assess its compatibility with other constituent components. Recent studies on 2D materials have shown that temperature and rippling have big effects on both planar stiffness and bending stiffness. Defects in 2D materials determine their fracture mechanics [2]. The way 2D materials behave mechanically

changes when they are doped [14]. To confirm these effects, further experiments are necessary. MD simulations can predict how elastic 2D materials will behave at certain temperatures, and as better force fields are made, they can give a more accurate picture of 2D systems.

However, the demand for 2D materials such as TMDs has yet to be sufficient for them to be mass produced. That makes it expensive. Furthermore, we do not have the essential experimental facilities that would be necessary to carry out research on 2D materials. In order to study the properties of 2D materials, viable options for us were to simulate the system. There are two computational methods mostly used for analyzing the properties of 2D materials. These methods are density functional theory and molecular dynamics. DFT adheres to quantum mechanics principles, whereas MD adheres to classical mechanics principles. Due to the slower and more computationally expensive nature of DFT, molecular dynamics was chosen for the simulation of this study. Molecular dynamics software LAMMPS (Large Atomic Molecular Massively Parallel Simulator) was used as our simulation tool. With the aid of this software, the stress-strain responses for vacancy-induced single-layer $MoTe_2$ of 2H (semiconducting) and 1T (metallic) phases were determined at 3 different temperatures, i.e., 100K, 300K and 500K.

1.5. Research Objectives

The objective of this study is to examine the impact of point and line defects on the mechanical behavior of single-layer $MoTe_2$. To accomplish this, olecular dynamics simulations were employed to model the structures of 2H and 1T $MoTe_2$ with three types of point defects and two types of line defects. The mechanical characteristics of both defective and non-defective pristine $MoTe_2$ were analyzed, including stress-strain response and Young's modulus. The defects were created by removing atoms from the perfect sheet, with three types of point defects and two types of line defects identified. The point defects are (i) 2 Tellurium vacancy , (ii) 4 Tellurium vacancy and (iii) 6 Tellurium vacancy accompanied by a Molybdenum vacancy. The line defects are (i) pre crack along armchair axis & (ii) pre crack along zigzag axis. The study investigated the impact of temperature and the direction of strain on the fracture mechanics of single-layer $MoTe_2$, with simulations performed at 100K, 300K, and 500K. The impact of strain rate on the mechanical response was also investigated using strain rates of 5e7, 1e8, and 5e8 along both armchair and zigzag axes. The Stillinger Weber potential was used for all simulations.

1.6. Methodology

LAMMPS was selected as the molecular dynamics simulation software for this study because of its wide application in the field of materials science. The LAMMPS program requires three essential files to execute a simulation: a structural file, an interatomic potential file, and an input script. The structural file stores crystallographic data for specific structures in a desired format, while the potential file outlines the interaction between two atoms, as well as the interaction between one atom and numerous atoms in a condensed phase. The interatomic potential consists of both attractive and repulsive interactions between atoms and molecules. Upon providing all the necessary information, LAMMPS performs calculations by reading one line at a time from the input script. The input script also includes the governing equations for the respective simulation to be performed. The calculation process terminates when the input script ends. [15].

1.7. Outline of the Thesis

The manuscript comprises 5 chapters and follows this structure: Chapter 1 provides a brief introduction to 2D materials and outlines the research objectives and scope. In Chapter 2, an overview of the current state of research and state of art is presented. Chapter 3 delves into the fundamental concepts of Molecular Dynamics and relevant simulation modelling tools. Chapter 4 offers a detailed insight of the research, including the research results and necessary validation of existing literature. Finally, Chapter 5 summarizes the previous sections, presents the conclusions of the study and discusses potential avenues for future research.

CHAPTER 2 : LITERATURE REVIEW

In this section, an overview is provided for Single layer $MoTe_2$ ($SLMoTe_2$), encompassing its chemical composition, properties, and applications. Subsequently, a more detailed review explores its mechanical behavior. The chapter explains the fundamentals of interatomic potentials and the concept of Molecular Dynamics. It also examines the current use of MD simulation to study the deformation of both pristine $SLMoTe_2$ and $SLMoTe_2$ with defects.

2.1. Composition of $SLMoTe_2$

Single layer $MoTe_2$ is a member of the class of materials termed Transition Metal Dichalcogenides (TMDs). It is composed of two elements: a transition metal called Molybdenum from group 6, and a chalcogen called Tellurium from group 16 of the periodic table. The structure of $SLMoTe_2$ consists of layers that are about 6 to 7 angstroms thick. Its layers are composed of metal atoms that form a hexagonal pattern and are bonded by weak van der Waals forces. [16]. The metal atoms contribute four electrons to form bonds, resulting in an oxidation state of +4 for the metal and -2 for the chalcogen. This information is illustrated in Figure 1, which depicts the location of Molybdenum and Tellurium on the periodic table [5].

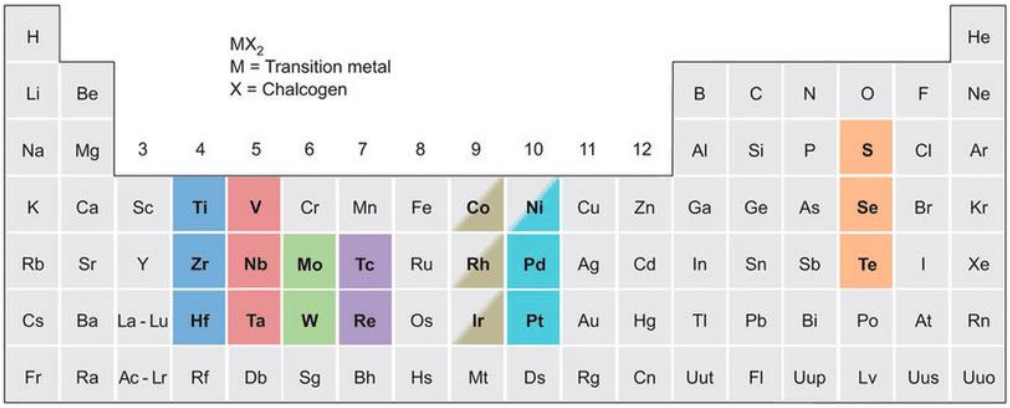

Figure 1: Arrangement of approximately 40 distinct layered transition metal dichalcogenide (TMD) compounds in the periodic table. The highlighted regions represent the transition metals and three chalcogen elements that commonly form crystalline structures within these layered compounds [104] .

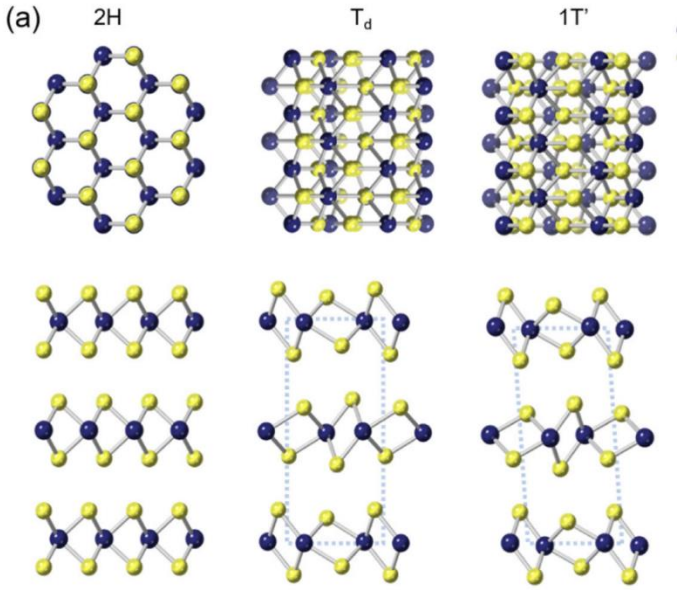

Figure 2: Three phases of 2D $MoTe_2$

$SLMoTe_2$ can exist in various phases such as the trigonal-prismatic 2H or α-phase, semimetallic orthorhombic γ-structure, and monoclinic 1T′ or β-phase [17]. The atomic structures of 2H, 1T, and 1T' $MoTe_2$ are illustrated in Figure 2, which also shows that $MoTe_2$ has two main directions of armchair and zigzag, similar to graphene. The atomic arrangement in the 2H structure follows an ABA layer sequence, whereas in the 1T and 1T' structures, the atoms are arranged in an ABC stacking sequence. The dimensions of the hexagonal lattice constant (α) and Mo-Te bond length are commonly used to characterize the atomic lattice of both 2H and 1T $MoTe_2$, where the lattice constant of 2H-$MoTe_2$ is 3.551 Å, and the Mo-Te bond length is 2.731 Å and 2.756 Å for 2H and 1T-$MoTe_2$, respectively. In a recent experimental study conducted by Wang et al, it was reported that the unit cell of 1T'-$MoTe_2$ structure contains a rectangular lattice with side lengths of 3.452 Å and 6.368 Å. The structure includes two separate Mo-Te bonds, measuring 2.718 Å and 2.823 Å in length [18] .

2.2. Properties and Application of $SLMoTe_2$

Single layer $MoTe_2$ exhibits unique electronic properties, including a transition from direct to indirect electron transition as it goes from monolayer to bulk. It also exhibits optic coupling effects, and the highest binding strength of excitons and tritons, as reported in previous studies [19]. The semiconductor and semimetal properties of $SLMoTe_2$ are of great importance and practical

significance. $MoTe_2$ behaves as a direct bandgap semiconductor in its single-layer or few-layer state, while transitioning to a bulk state introduces an indirect bandgap of approximately 1 eV, which is similar to Si. Due to this, 2H-$MoTe_2$ is highly suitable for electronic and optoelectronic applications [20][21].

The presence of distinct phases in $MoTe_2$ offers opportunities for creating innovative devices and architectures. Transforming the 1T'-$MoTe_2$ phase to the 2H-phase has the potential to create single-material circuits that serve both as semiconducting channels and metallic interconnects, thus presenting an opportunity for significant technological advancements [22]. By achieving better control over the phase conversion, it may also be possible to reduce the semiconductor-metal Schottky barrier and enhance optoelectronic performance by evolving the electronic band structure continuously [23]. Recently phase engineering of $MoTe_2$ has been achieved through laser processing [24] and chemical modification of its contact [25].

The ability to manipulate the phases of $MoTe_2$ holds great promise for various applications. Doping, temperature fluctuations, strain manipulation, and the application of electric fields are among the methods that can be utilized to induce transitions from metallic to insulating states. These transitions hold potential for applications in the fields of sensors and nonvolatile information storage [26][27][28][29]. Furthermore, it has been suggested that monolayers of $MoTe_2$, which have semimetallic properties, potentially exhibit a Z_2 topological invariant. This characteristic indicates a ground state that exhibits a quantum spin Hall effect, with edge states that are nondissipative and a bulk gap [30]. If confirmed, these edge states may have the potential to be utilized as non-dissipative nano interconnects between logic elements that rely on 2H-$MoTe_2$ semiconductors for energy-efficient electronics. [31].

Recent advancements in theory suggest that both the orthorhombic forms of $MoTe_2$ could potentially be utilized as a novel type of Weyl semimetal. This is characterized by linear touching points between the electron- and hole-Fermi surfaces, where the Berry phase exhibits topological singularities [32][33][34][35][36][37]. The unconventional transport properties arising from the singularities observed in the $MoTe_2$ orthorhombic phase, which recent theoretical developments propose as a potential candidate for a Weyl semi metallic state characterized by linear meeting points between hole and electron-Fermi surfaces and topological singularities in Berry-phase, have been suggested to be of significant interest [38].

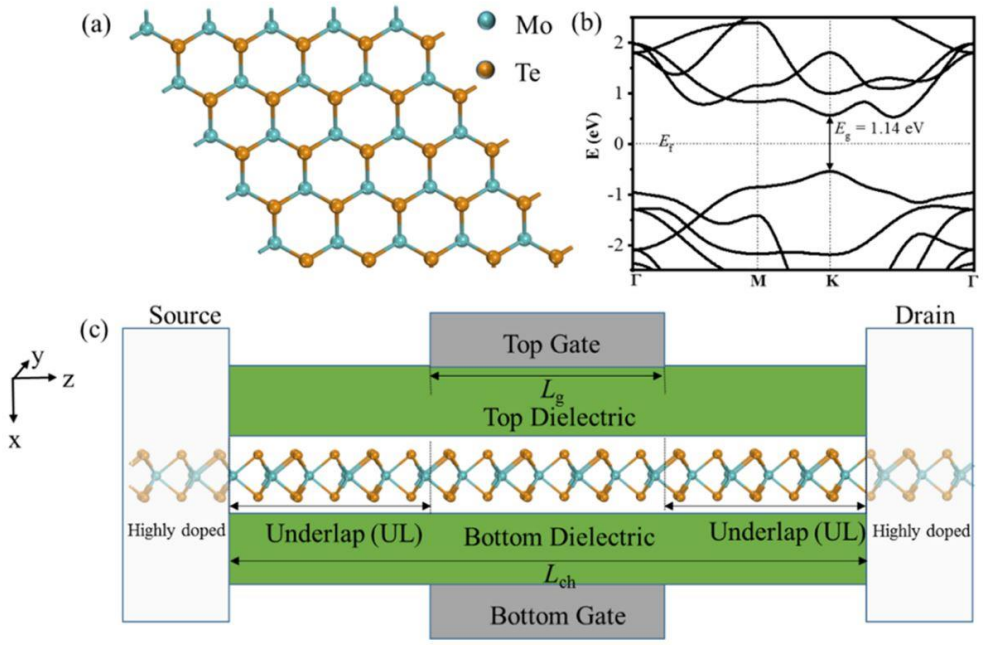

Figure 3: (a) Illustration of the lattice structure of monolayer (ML) $MoTe_2$. (b) Representation of the single layer $MoTe_2$ band structure. (c) Illustration of the double-gate (DG) monolayer $MoTe_2$ field-effect transistors (FETs).

At present, researchers are placing their attention on $MoTe_2$ to create memory devices with adjustable phases, taking advantage of the tiny energy gap between its 2H and 1T' phases, and validated experimental observations of phase alteration under strain, gating, and heating [39][40][18][29][31]. However, creating large-scale $MoTe_2$ thin films for use in electronic applications is still challenging, as is precisely controlling the number of layer depositions [41].

$MoTe_2$ is a highly promising material for phase-engineered applications, owing to its minimal energy gap ($\Delta E < 50$ meV) between the semiconducting 2H phase and the metallic 1T' phase [26][24]. The disparity between the 2H and 1T' phases of $MoTe_2$ results from the configuration of Te atoms in space. While the 2H phase has a bandgap of roughly 1.0 eV, making it promising for use in photonics, silicon-integrated optoelectronics, and Field Effect Transistors, the potential for transitioning from the 2H to the 1T' phase is also noteworthy [21][42][43][44].

Researchers have proposed two-dimensional semiconductors as promising candidates for channel materials as silicon-based field-effect transistors (FETs) are nearing their scaling threshold. Recently, experimental fabrication of air-stable 2D trilayer (TL) $MoTe_2$ FETs with a 4 nm gate length has been achieved [45]. A DG SL$MoTe_2$ FET is shown in the Figure 3. A novel method to switch $MoTe_2$ between its semimetallic 1T' phase and a semiconducting phase has been proposed

by utilizing electric-field-induced strain in a field-effect transistor configuration. Nanoscale strain engineering using thin films and ferroelectrics provides a means to accomplish this desired outcome. This approach presents a remedy for the issues of static and dynamic power consumption encountered by traditional field-effect transistors [46][47].

2.3. Mechanical Behaviour of SL$MoTe_2$

The existence of multiple crystal structures of 2D transition metal dichalcogenides (TMDs), including 2D $MoTe_2$, presents significant opportunities for the advancement of 2D electronics. The Ohmic behavior of the metallic-semiconducting homojunction in TMDs has been experimentally demonstrated [48], presenting a promising solution to the contact problem in the domain of two-dimensional (2D) electronics [49]. However, the exploration of phase transitions and the consequent semiconductor-metal transition has been largely overlooked due to the high temperature requirements. Recent developments have shown that strain can be a useful tool to regulate the transition temperature [50][51][52][53][54][55]. The planar configuration of TMDs provides an easy method to apply tensile strain in the thin film, making it an appealing means to regulate phase engineering [49].

In a recent study [49], Manipulation of the phase transition temperature of $MoTe_2$ has been achieved by applying mechanical strain, leading to a reversible phase transition under ambient conditions at room temperature, as demonstrated by researchers as illustrated in Figure 4. The researchers employed an AFM tip to apply a slight tensile strain, enabling the identification of the phase transition using CAFM. The study reveals that the level of strain applied affects the phase transition temperature, which can be reduced from approximately 900°C to room temperature. The researchers demonstrated that the phase transition from the SM phase at room temperature exhibited complete reversibility upon strain release.

Numerous studies have been conducted to explore the mechanical characteristics of monolayer $MoTe_2$ in both its 2H and 1T phases. Experimental investigations suggest a Young's modulus of around 110 GPa [56], while theoretical studies predict a range of values between 60-115 GPa [17][57][58]. However, researchers have not yet achieved a thorough comprehension of the elastic properties and fracture dynamics of $MoTe_2$.

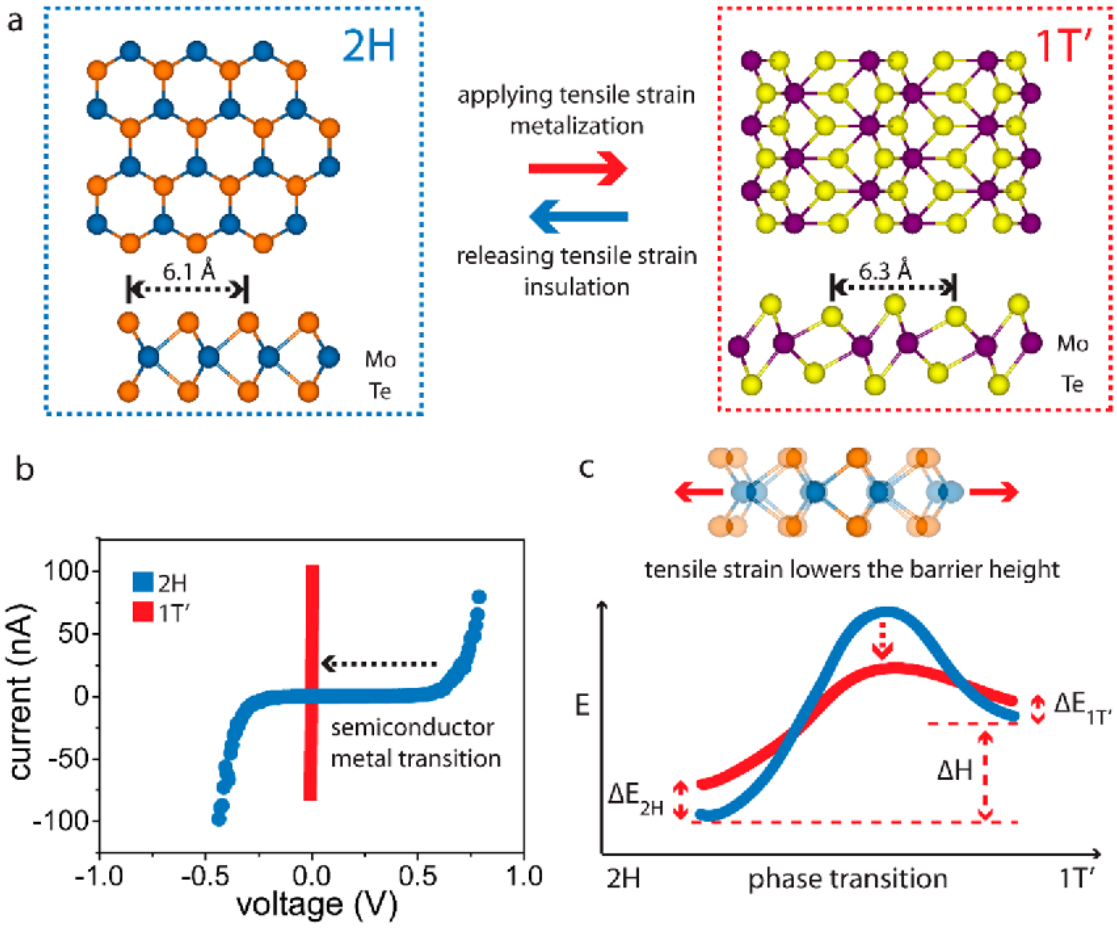

Figure 4: Strain-induced control of phase transition and transition from semiconductor to metal in $MoTe_2$ (a) Atomic structures of 2H and 1T' $MoTe_2$, where the polymorphic behavior is regulated by planar tensile strain. (b) Semiconductor to metal transition observed through changes in the IV curves during the 2H to 1T' phase transition. (c) Schematic representation of strain-modulated phase transition barrier, leading to a reduced phase transition temperature due to decreased activation energy under tensile strain.

The Young's modulus of 2H $MoTe_2$ was determined by Without considering the thickness of the 1H-$MoTe_2$ monolayer, a linear fitting analysis was conducted on the stress-strain relationship within a narrow strain range of [0, 0.01]. The isotropic Young's modulus values were found to be

79.8 N/m and 78.5 N/m for the armchair and zigzag directions, respectively, and showed good agreement with experimental results such as 79.4 N/m from Ref. [59] and 87.0 N/m from Ref. [60]. Likewise, for 1T $MoTe_2$, the stress was calculated without accounting for the quasi-two-dimensional structure for the single-layer 1T-$MoTe_2$, and the Young's modulus was obtained by linear fitting of the stress-strain relationship within the small strain range of [0, 0.01]. The resultant isotropic Young's modulus values were 81.6 N/m and 81.2 N/m for the armchair and zigzag directions, respectively. However, the fitted value of the Young's modulus was approximately 10% smaller than the ab initio result of 92 N/m [61] due to the limited consideration of short-range interactions in a recent study [62].

In recent studies, reactive potential molecular dynamics simulations were employed to examine the elastic properties and fracture dynamics of $MoTe_2$ membranes in both the 2H and 1T phases. These investigations have shown that the fracture mechanism of $MoTe_2$ involves rapid crack propagation followed by a sudden rupture of the membranes into fragments that maintain a high level of integrity. Cumulative findings that the structural stability of $MoTe_2$ monolayers could be higher than that of MoS_2 monolayers.

Moreover, the structural stability of the 1T phase of $MoTe_2$ is lower compared to the 2H phase due to the translated layout of chalcogen atoms [63]. The 1T phase also exhibits lower tensile strength. Recent research has revealed that $MoTe_2$ exhibits anisotropic mechanical properties, and the orientation of its atomic lattice can have a profound effect on its tensile properties. [17].

A recent investigation using atomistic simulations has explored the mechanical behavior of monolayer and multilayer $MoTe_2$ at the nanoscale. The researchers were able to develop an empirical potential that accurately predicted both the elastic and failure properties of $MoTe_2$, comparable to first-principles calculations and experimental findings. The study found –

1. The nonlinear mechanical response of $MoTe_2$ under uniaxial tensile loading reveals significant directional anisotropy.
2. Strain transfer in the out-of-plane direction occurs mainly in the top four layers of multilayered $MoTe_2$ films, and the Raman peak shifts calculated from simulations correspond well with experimental observations.

3. The elastic and failure properties of $MoTe_2$ are considerably influenced by macroscopic factors, including crystal orientation and temperature [64].

2.4. Computational Methods

Computational methods, including DFT and MD, offer valuable insights into thin-film deformation. Although DFT can incorporate quantum mechanical information, its practical use is constrained to a few thousand atoms, and alternative techniques are needed for larger-scale analysis, such as nanoscale deformation mechanisms. Molecular Dynamics simulations are well-suited for length scales ranging from nanometers to microns and can effectively model macroscopic factors, including temperature and various complex mechanical loads [65]. To accurately describe the forces between atoms in MD models, the choice of interatomic potential is crucial [66][67]. The Stillinger-Weber (SW) potential is a viable option for modeling single layer TMD systems, as it has the ability to precisely capture the main bond-stretching and angle bending interactions, including their nonlinear impacts [68]. Furthermore, in terms of computational efficiency, the Stillinger-Weber (SW) potential outperforms bond-order potentials , such as REBO and Tersoff [69][70], making it a more efficient choice for modeling larger structures with reasonable accuracy [71].

2.5. Density Functional Theory

Density Functional Theory (DFT) is a method that allows for efficient computation and provides precise descriptions of chemical bond correlation in various systems [72][73]. It can be difficult to experimentally determine the stress-strain behavior of single layer systems, particularly in cases where manufacturing specific two-dimensional materials is not possible or where defects may occur during the preparation process. However, DFT can establish correlation between the internal energy of the atomic system and the external energy exerted on it. The Hohenberg-Kohn theorems form the foundation of DFT and is comprised of 2 theorems:

(i) the Hohenberg theorem and
(ii) the Kohn theorem [74]

In the context of the Hohenberg-Kohn theorems, the first H-K theorem asserts that the electron density governs all the characteristics of a non-degenerate ground state of a molecule or an atom. This means that electrons are deemed to be moving within a confined box, which is a fundamental principle of the H-K theorems.

In the study of electrons, they move in a random manner while being influenced by an external potential v(r) and mutual Coulomb repulsion. The ground-state energy is achieved through an external potential, and this process is evaluated using the Hamilton equation. This equation involves the Hamiltonian (H), which includes the kinetic energy (T), potential energy from the external field caused by positively charged nuclei (V), and the interaction energy between electrons (U). In the context of electronic structure calculations, the probability of finding electrons in a small volume element around a specific configuration xi is expressed by the many-electron wave-function. This wave-function is assumed to represent the system in an electronic eigenstate, while the nuclei remain fixed at their positions.

$$H = T + V + U \tag{1}$$

$$T = \sum_{i=1}^{N} \left(-\frac{h}{2m_i^2} \nabla^2 \right) \tag{2}$$

$$V = \sum_{i=1}^{N} v(r_i) \tag{3}$$

$$U = \sum_{i<j}^{N} u\left(r_i \,/\, r_j\right) \tag{4}$$

$$H\phi = (T + V + U)\phi = E\phi \tag{5}$$

After previous DFT methods were established, a new strategy known as Hohenberg-Kohn-Sham (HKS) DFT was introduced, which follows the second H-K theorem that establishes an energy functional for the system and indicates that the energy functional is minimized by the electron density of the ground state [75]. Another method called Kohn-Sham (KS) DFT was introduced, following shortly after the HKS DFT. This method addresses the challenge posed by interacting electrons in a fixed external potential [76]. However, modelling these interactions can be a challenge in KS DFT. To address this, the local-density approximation (LDA) is often used for approximation. Orbital-free density functional theory (OFDFT) is a less commonly utilized alternative to KS DFT but is computationally efficient and applicable to large systems. However, OFDFT is less accurate than KS DFT. Despite the widespread use of DFT in material science, it has some limitations, including computational expense, errors due to deficiencies of the exchange-correlation functional, and the impact of the potential on the accuracy of the calculation. Therefore, molecular dynamics simulation is preferred in some cases.

2.6. Molecular Dynamics

In order to study the behavior of particles in a system over a period of time, researchers often employ molecular dynamics (MD) simulations, which are capable of generating true dynamical observables and sampling equilibrium distributions. Initially used to simulate small numbers of molecules, MD has been extended to study liquids, solids, and materials with the advancement of computer technology [77]. A. Rahman performed the first MD simulation for atoms interacting through an interatomic potential in 1964 [78]. MD follows a deterministic approach to mimic the movement of atoms, where Newton's equation of motion is solved in successive time steps. In every time, the forces among all atoms within the system are evaluated and utilized to compute new velocities and positions. Based on these values, the material properties of the system can be derived.MD is essential for studying large systems of more than thousands of atoms, as it allows for the calculation of processes such as melting, deformation, sintering, and crack propagation in materials. However, MD relies on two primary approximations, namely the Born-Oppenheimer approximation [79] and the assumption that atoms are point particles following classical Newtonian dynamics. In molecular dynamics simulations, interatomic potentials are employed to move atoms based on Newton's laws of motion. [80], shown in the Eq. (6)

$$-\nabla\phi = \vec{F} = m\frac{d^2\vec{r}}{dt^2} \quad (6)$$

The overall empirical potential energy of a molecule is made up of various energies related to bond, angle, van der Waals force and electrostatic interactions. This composition is used in molecular simulations to determine the behavior of the system. To understand the mechanical and thermal properties of 2D materials using MD, the energy correlation of the entire system must be considered.

2.7. Force Fields

Force fields are essential mathematical models utilized in MD simulations to predict the forces and energies existing between atoms or molecules within a given system [81]. These models represent the potential energy of the system by factoring in the arrangement and orientation of its constituent atoms or molecules. By using force fields, scientists can examine and predict the behavior of complex molecular systems, which are otherwise challenging to analyze experimentally.

During the 1960s, researchers first developed force fields to predict the vibrational spectra, molecular structures, and enthalpies of isolated molecules. As researchers extended these models to more complex systems, new and more broadly applicable force fields were developed. Examples of these include Dreiding [82], Universal (UFF) [83], CHARMM [84], AMBER [85], GROMOS [86], OPLS [87], and COMPASS [88]. The force fields are not static, but rather dynamic in nature and are subject to ongoing development, with numerous versions available.

Force fields can be classified as 1st generation or class I force fields, and second-generation or class II force fields, which include cross terms. The performance of general force fields varies depending on the system and properties being simulated. In the scientific literature, comparisons have been made between the accuracy of biomolecular simulations using the CHARMM, AMBER, and OPLS force fields, but no definitive conclusions have been reached. The choice of a specific force field is influenced by the particular strengths and limitations that stem from the data and procedure used for its parametrization. As a result, the selection of an appropriate force field is highly dependent on the particular problem under investigation.

In the literature, various potential models (Shown in Figure 5) have been proposed for covalent materials, ranging from straightforward and computationally affordable to intricate and computationally expensive models. In the modeling of covalent materials, several potentials have been developed, including the the Stillinger-Weber (SW) potential, valence-force field (VFF) model, Tersoff potential, Brenner potential, and ab initio methods. These force fields are useful

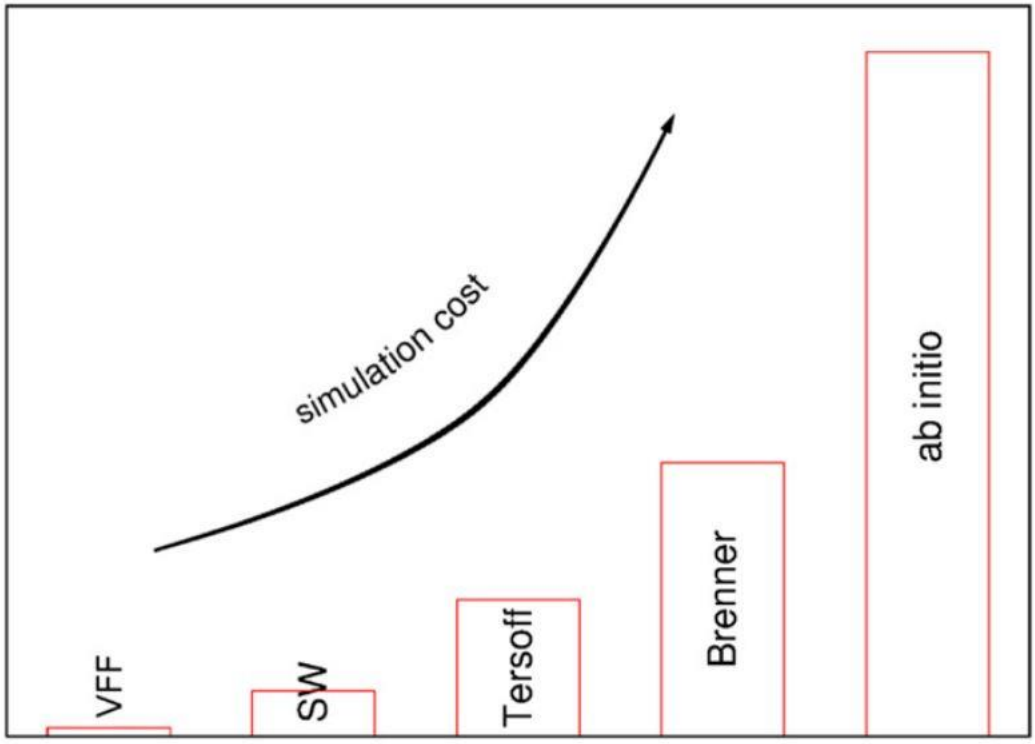

Figure 5: A comparative schematic illustrating the computational cost of various interatomic potentials [105].

in capturing the angle-bending and bond stretching motions observed in these materials. Although they can also model bond-twisting motion, it is generally associated with a relatively small amount of energy. The choice of potential model is contingent upon the specific research objective and computational resources available [89].

The Stillinger-Weber (SW) potential is a well-established interatomic potential that has been extensively employed in simulating various materials, including two-dimensional (2D) materials such as $MoTe_2$ [62]. The SW potential is particularly beneficial for studying 2D materials because it can precisely account for the interlayer interactions that play a vital role in determining their mechanical, electronic, and thermal properties [90].

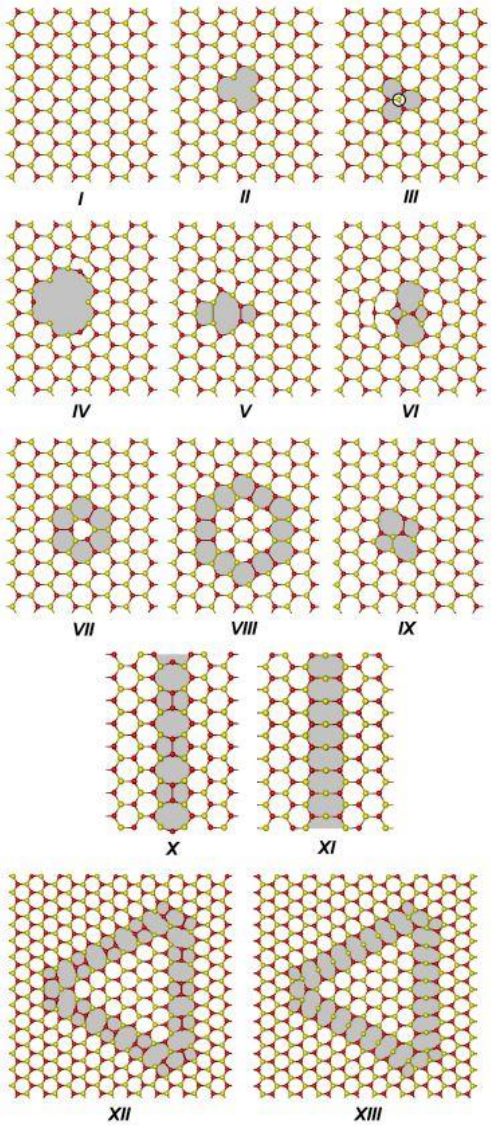

Figure 6: Depiction of local defects in MoS_2 monolayer (ML): (I) ideal structure, (II to IX) defective structures containing point defects, (X & XI) line defects and (XII & XIII) grain boundary defects. The defective regions are indicated, with Mo and S atoms represented in red and yellow, respectively. These figures display part of the simulated supercells. [91]

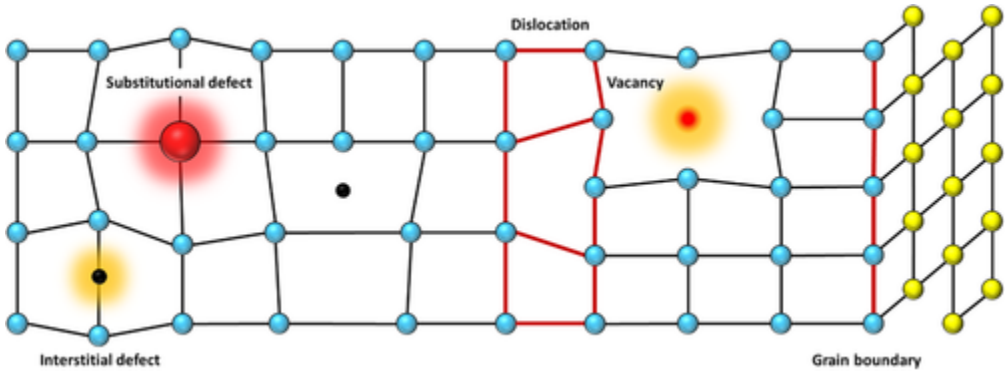

Figure 7: Visualization showcasing the common defects observed in the crystal lattices of solution-processed transition metal dichalcogenides (TMDs) [92].

2.8. Structural Defects

Defects are commonly observed in 2D materials, including $MoTe_2$, and can result from various sources such as impurities, vacancies, adatoms, or dislocations [93]. These defects (See Figure 6 and Figure 7) can be categorized into four types : point defects [91], line defects [94][95], grain boundaries [91], and edge defects [96]. Point defects occur due to impurities or vacancies, line defects arise from a missing line of atoms in the crystal lattice, grain boundaries result from different crystal orientations, and edge defects occur at the abrupt termination of the crystal lattice. Investigating defects in 2D $MoTe_2$ is crucial as these defects can considerably affect the optical, electronic, and mechanical characteristics of the material. Examining such defects can give us valuable insights into the behavior and performance of 2D $MoTe_2$ in different applications. [97][95].

CHAPTER 3 : METHODOLOGY

Since the structure (2D $MoTe_2$) we are going to study is in nanoscale, molecular dynamics emerges as the preferred simulation method. Molecular dynamics analyses movement of atoms and molecules to calculate overall deformation, force and potential energy of the system. From the numerical data obtained, different parameters like engineering stress, strain, bond strain, bond stress or young's modulus can be calculated for specific timestep interval for different boundary conditions. Molecular dynamics abides by the principles of classical mechanics. That implies that small atoms' and molecules' trajectories are deduced from Newton's equation of motion for the complex systems made of particles that interact with each other. The interaction between atoms and molecules are defined by their attraction force as well as repulsion force. The interplay parameters are contained in a potential file. One of the commonly used interatomic potential is Stillinger weber potential. We have used Stillinger weber potential for our simulation. Figure 8 shows a comprehensive flow diagram of how molecular dynamics simulation is done.

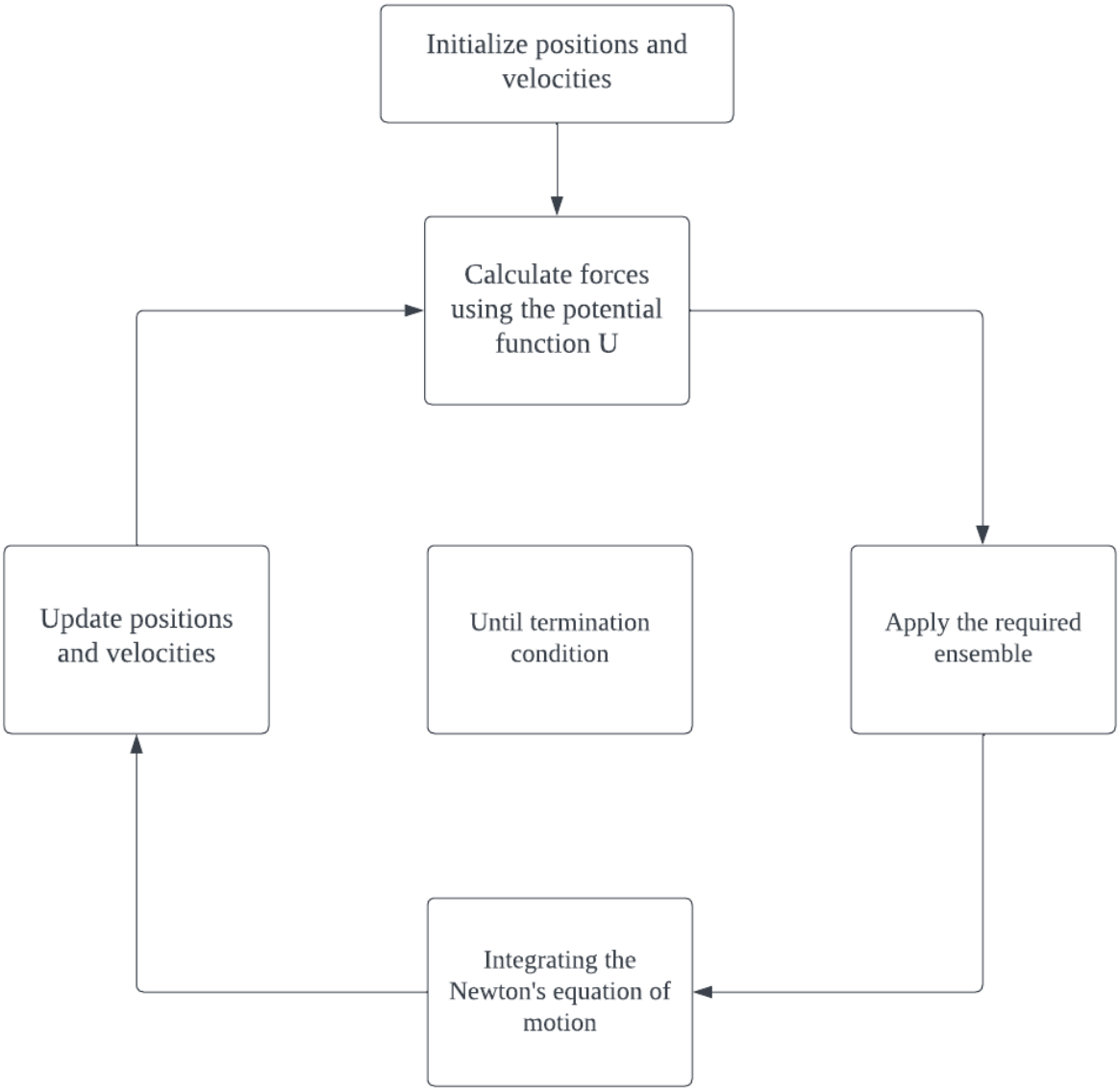

Figure 8: Molecular Dynamics Simulation Flow Diagram

3.1. Molecular Dynamics

In Molecular Dynamics simulations, the movement of atomic entities is determined by numerically integrating Newton's second law of motion. Like Monte Carlo simulations, Molecular Dynamics calculations involve computing thermodynamic averages at uncorrelated time points to obtain statistical significance. Molecular dynamics is utilized across a broad spectrum of disciplines from molecular biology to material science. It enables us to dig into thermodynamic and kinetic properties inherent to a system and to calculate pressure temperature, reaction or energy in molecular level.

Maintaining temperature and pressure within the system is a vital aspect of molecular dynamics simulations. Temperature plays a crucial role in dictating the kinetic energy of the atoms, which consequently influences their motion and interaction with one another. It is therefore imperative to control the temperature to ensure that the system samples the correct phase space and attains the desired thermodynamic state. The pressure of the system, on the other hand, affects the intermolecular distances and the interaction between the atoms. Proper control of pressure helps maintain the desired density and prevents uncontrolled expansion or contraction of the system. In molecular dynamics simulations, temperature and pressure can be regulated by employing a thermostat and barostat. There are various techniques for doing so, with three main methods commonly employed in the literature –

1. Nose Hoover Thermostat-Barostat:

In MD simulations, the Nose-Hoover Thermostat-Barostat is a widely used method to control the temperature and pressure of the system. This method adjusts the velocities of the atoms to achieve a desired temperature distribution and generates momentum in the system. It is the only thermostat among the three principal methods that is derived from statistical mechanics. The Nose-Hoover Thermostat-Barostat is particularly useful for studying liquids and solids with slow relaxation times, as it efficiently calculates thermodynamic properties such as heat capacity, thermal expansion coefficient and compressibility.

2. Brendensen Thermostat-Barostat

The Brendensen thermostat-barostat adjusts velocity proportionally using the same factor to obtain the desired temperature. It is a simple and commonly used method in molecular dynamics simulations, particularly for controlling very large velocities. This thermostat is especially useful for non-equilibrium systems that involve reactions and is compatible with reaxff potential. One of its main advantages is its ease of implementation and computational efficiency, making it a popular choice for researchers.

3. Langevin Thermostat

In molecular dynamics simulations, the Langevin thermostat simulates the effect of collision with solvent molecules to create a non-Gaussian velocity distribution that results in random diffusion of particles. This thermostat is commonly used for equilibrating unstable systems by reducing the magnitude of velocity and adding random forces in different directions. It is particularly useful for simulating biological macromolecules in solution and can also be coupled with a barostat to regulate the temperature and pressure of the system simultaneously.

3.2. LAMMPS

The molecular dynamics simulations for this study were conducted using the LAMMPS software, which is founded on the principles of molecular dynamics. The LAMMPS software, which stands for Large-scale Atomic/Molecular Massively Parallel Simulator, was created in the 1990s by Sandia National Laboratory as an open-source code. Initially, LAMMPS was written in Fortran, but later versions were written in C++. This software is compatible with CPU and GPU, and parallel computing can be employed for improved performance. The developers' package of LAMMPS provides users with the flexibility to modify the code to fit their needs. LAMMPS allows us to couple it with other third-party software. For example, VESTA and OVITO software, along with LAMMPS, were utilized for visualization purposes. The process is illustrated in the flowchart in Figure 8.

3.3. Initialization

The initial step in our simulation process involves defining the thermodynamic activity unit in LAMMPS. LAMMPS offers a variety of styles, such as real and metal, which are typically used for simulating 2D materials. Following the unit definition, the simulation boundary conditions were set up.. These conditions are defined by styles p, f, s, and m. In particular, style p indicates that the simulation box is periodic, allowing particles to interact with their mirror images across the boundary. On the other hand, styles f, s, and m signify that the simulation box is non-periodic, fixed, and shrink-wrapped, respectively.

3.4. Periodic Boundary Condition

The periodic boundary condition is implemented in the study using the style p in the simulation, which allows particles to interact across the boundary and allows for the box to be infinitely extended in all directions. To avoid any potential impact of artificial boundaries on simulation outcomes and enable large system studies, periodic boundary conditions are typically employed in MD simulations. In this approach, particles interact with their mirrored images across the boundary, which allows them to exit the box from one side and re-enter from the opposite side (see Figure 9) . The periodic dimension of the box can be adjusted through constant pressure boundary conditions or box deformation. This is particularly useful for mechanical deformation of 2D materials as it enables the material to deform without encountering artificial boundaries that could affect the simulation results. Moreover, periodic boundary conditions facilitate the simulation of larger systems, which is crucial for studying the mechanical properties of materials accurately. It is essential to know that the dimensions of the periodic box may experience alterations in size owing to constant pressure boundary conditions or box deformation.

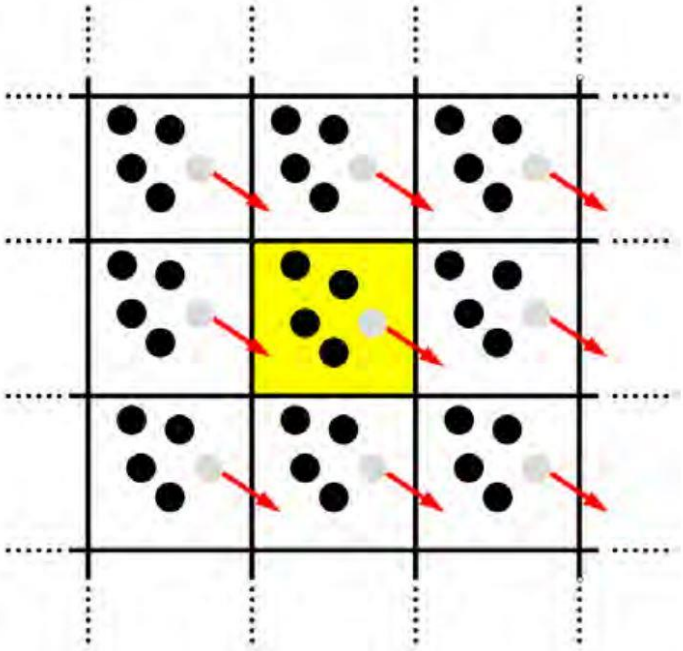

Figure 9: A two-dimensional representation illustrating the implementation of periodic boundary conditions. The particle paths within the main simulation box are mirrored in all directions.

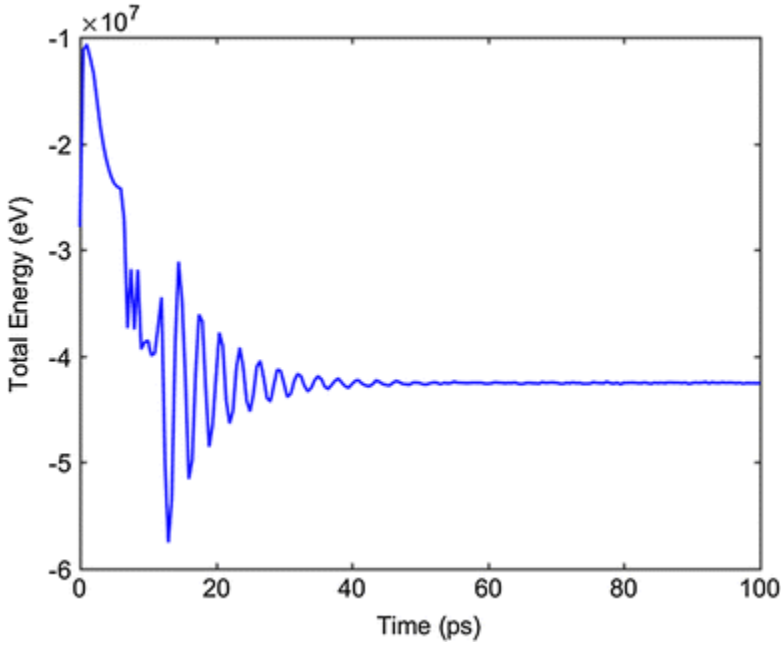

Figure 10: Relationship between total energy and time during the process of energy minimization [98].

3.5. Energy Minimization

The process of energy minimization in LAMMPS simulation involves the a step-by-step adjustment of atom positions, the potential energy of the system is systematically reduced until it reaches its minimum (Shown in Figure 10). This process not only optimizes the initial structure but also corrects overlap in atoms and fixes broken bonds or angles. LAMMPS offers several energy minimization techniques, including conjugate gradient (CG), steepest descent (SD), and Newton's method (QM), which can be used alone or in combination, depending on the complexity of the system and user preference. The CG technique was employed for the simulation. Energy minimization is an essential step in MD simulations, especially for studying mechanical properties in 2D materials. It ensures that the simulation begins with a stable configuration, which allows for accurate and reliable results.

3.6. Molecular Modelling

Molecular modeling involves computer simulations to investigate atomic-level changes in materials. While early simulations were limited to small systems like diatomic gases and simple interatomic potentials due to computational constraints, advancements in computer technology now enable us to study much larger systems, potentially consisting of millions of atoms. By simulating the mechanical, thermal, and chemical properties of materials, molecular modeling can offer insights into their fundamental behavior. Additionally, this technique can be practiced to project the behavior of new materials even before they are synthesized, thereby enabling their optimization for specific applications.

3.7. Ensembles

Ensembles are used in MD simulations to analyze and describe the behavior of a system in different thermodynamic states. They are a collection of all possible positions and momentum of atoms in a given state and are a crucial aspect of the phase space. Ensembles satisfy specified thermodynamic values, such as temperature, pressure, volume, and energy. Their importance lies in allowing for the study of various physical systems under diverse conditions. In molecular dynamics, ensembles refer to the collection of particles or molecules that interact with one another and their surroundings. There are multiple types of ensembles, including the microcanonical

(NVE), canonical (NVT), and isobaric-isothermal (NPT) ensembles, which differ in their means of controlling the system's temperature, energy, and pressure. For our simulation, the NVT and NPT ensembles were employed.

NVE (Microcanonical Ensemble):

The microcanonical ensemble, also known as NVE, is a type of ensemble used in molecular dynamics simulations where the energy within the system is conserved due to the oscillation between the atoms' kinetic energy and the bonds' potential energy. This type of ensemble maintains a fixed number of atoms and fixed volume all over the simulation.

NVT (Canonical Ensemble):

In the NVT (Canonical Ensemble), the atom count and volume of the system are kept constant, while the total energy of the system is allowed to change by exchanging kinetic energy with the surroundings. This allows for the maintenance of a constant temperature throughout the simulation.

NPT (Isobaric-isothermal Ensemble):

In the NPT ensemble, the system's volume is tuned to maintain a user-specified pressure, while the number of atoms and temperature remain constant. The ensemble is useful for simulating systems in which pressure plays an important role, such as liquids and gases.

3.8. Interatomic Potential

In order to numerically investigate physical and mechanical properties, it is essential to account for atomic interactions in MD simulations (see Figure 11). The force exerted on each atom is determined by Newton's second law of motion, with various interatomic potential models employed, including Valence Force Field (VFF), Tersoff, Brenner, Stillinger-Weber (SW) and ab initio potentials.

The linear model of the Valence Force Field (VFF) was sidespread in the decades leading up to the 1980s due to its computational efficiency. However, its accuracy is restricted to evaluating the elastic properties of linear models. In contrast, the ab initio approach is known for its high accuracy in predicting a wide range of physical properties, including nonlinear effects. However, it is computationally intensive and requires significant computational resources, even for simulations involving only a few thousand atoms.

Hence, it is essential to close the divide between affordable linear models like VFF and the computationally intensive but highly precise ab initio method, as numerous research studies necessitate efficient simulation that balances accuracy with nonlinear treatment. In response to this challenge, several interatomic potential models have been suggested to span this intermediate range, such as the Tersoff potential, SW potential and Brenner potential. These potential models offer reasonably accurate representations of nonlinear effects and are particularly well-suited for conducting molecular dynamics simulations.

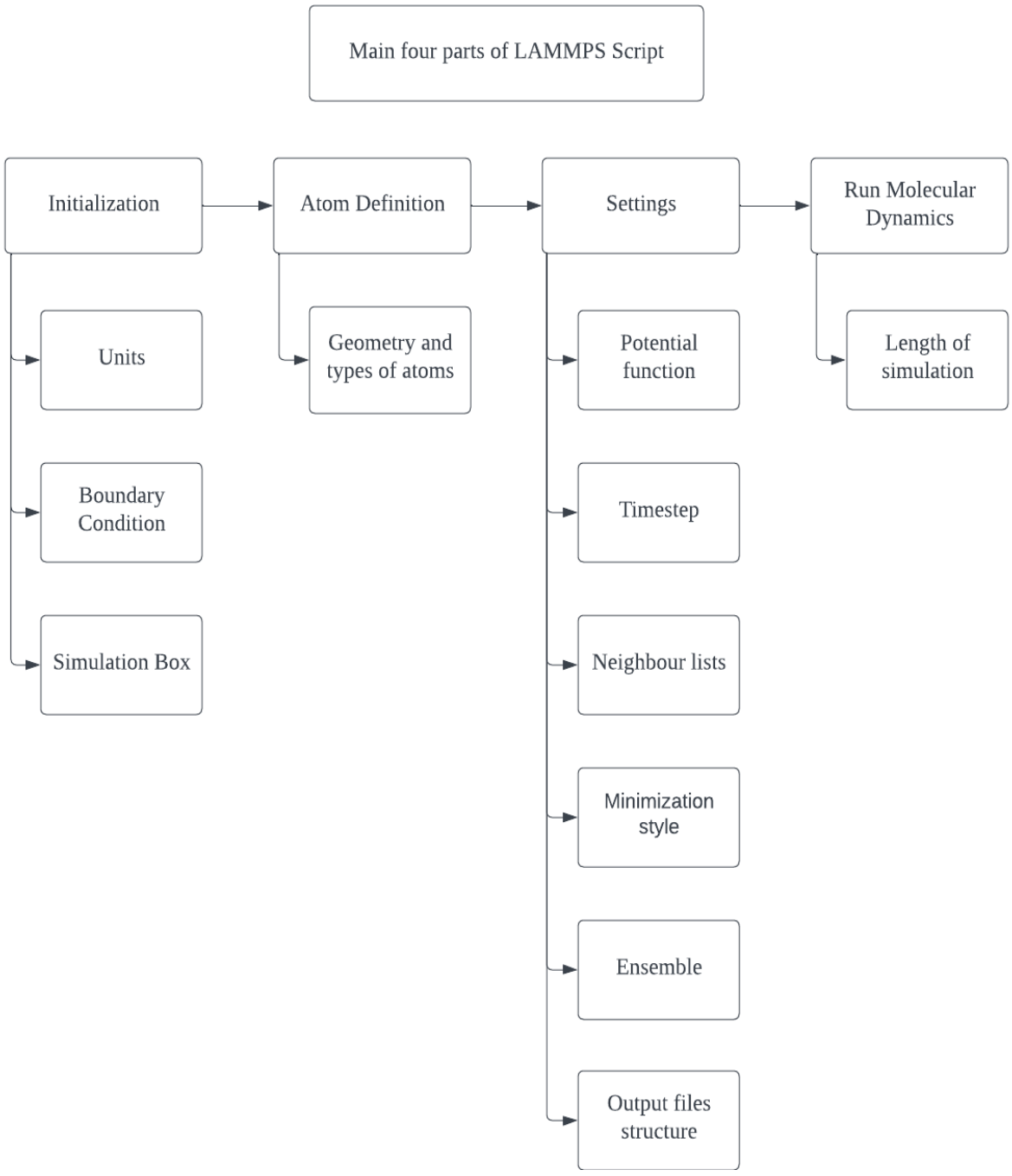

Figure 11: Simplification of parts of LAMMPS Script

3.9. Objectives of this Study

The topic of our thesis was to study the impact of point and line defects on the mechanical behaviour of single layer $MoTe_2$. To study the mechanical behaviour, determination of Young's modulus and ultimate tensile strength is required. That implies the necessity of knowing the stress-strain response of $MoTe_2$ with point and line defects. To determine the stress-strain response we have to perform tensile test using LAMMPS.

The tensile test is to performed for both phases of $MoTe_2$ and for 3 types of defective structures of $MoTe_2$ with –

(i) 2 Tellurium vacancy

(ii) 4 Tellurium vacancy

(iii) 6 Tellurium vacancy accompanied with one Molybdenum vacancy

(iv) Line vacancy defect along armchair axis

(v) Line vacancy defect along zigzag axis

The tensile test is to be performed at both uniaxially in armchair and zigzag axes and also biaxially.

3.10. Mechanical Deformations

The mechanical, electronic, and optoelectronic properties of electronic components can be significantly influenced by the loading conditions they experience during manufacturing and usage. Understanding these loading conditions is crucial for establishing a functional relationship between the applied loads and the resulting properties of these components. Specifically, it is important to determine parameters such as fracture strength, fracture criteria and Young's modulus.

Generally, there are two main types of loading conditions that 2D materials, which electronic components often comprise, are subjected to:

(i) Static Loading: This refers to a loading condition where the applied load remains constant over time. In this scenario, the components experience a consistent level of stress or strain without any significant variations. Static loading is commonly encountered during the manufacturing process or in steady-state operating conditions. By studying the response of 2D materials to static loading,

insights into their mechanical and functional properties under constant stress or strain conditions can be gained.

(ii) Dynamic Loading: Unlike static loading, dynamic loading involves the application of loads that vary over time. These loads can be periodic, cyclic, or transient in nature. Dynamic loading conditions are encountered in various scenarios, such as during the operation of electronic components subjected to vibrations, thermal expansion and contraction, or other dynamic environmental conditions. The response of 2D materials to dynamic loading provides valuable information on their ability to withstand fluctuating or time-dependent stresses, strains, and external forces. Dynamic loading is also classified into harmonic, non-periodic and periodic loading. Mechanical behaviour of 2D materials also varies with these loading conditions.

3.11. Computational Methodology

LAMMPS requires 3 files to run the tensile test simulation which is also depicted in Figure 7 and Figure 8. These files are atomic structure file, interatomic potential and input script. The output files obtained are log file that contains all the numerical information of the simulation. The stress-strain plot can be generated using Excel from this file. Another output file is dump file for visualization of the simulation. OVITO is used for the visualization

3.12. Molecular Modelling

This file encompasses comprehensive details concerning the material intended for utilization. The bond distance, bond length, bond angle between atoms and dihedral angle between planes are provided in the structure file. Both phases (2H and 1T) of $MoTe_2$ were used for our study. The structural information is provided below –

3.13. 2H $MoTe_2$ Structure:

The layer of 2H $MoTe_2$ sheet was of 15 nm on both sides. The lattice parameters and structure parameters of 2H $MoTe_2$ structure are given in the following Table 1 and 2 respectively.

Table 1: Lattice Parameters of 2H $MoTe_2$ Supercell

a	3.47 Å
b	3.47 Å
c	14.65 Å
α	90^o
β	90^o
γ	120^o

Table 2: Structure Parameters of 2H $MoTe_2$

Element	x	y	z
Te	1/3	2/3	0.859
Te	1/3	2/3	0.236
Te	2/3	1/3	0.671
Te	2/3	1/3	0.048
Mo	1/3	2/3	0.717
Mo	1/3	2/3	0.094

3.14. 1T $MoTe_2$ Structure:

For monolayer 1T $MoTe_2$ sheet that is 15 nm dimension was used on both sides. The lattice parameters and structure parameters of 1T $MoTe_2$ structure are given in the following Table 3 and 4 respectively.

Table 3: Lattice Parameters of 1T $MoTe_2$ Supercell

a	6.35 Å
b	3.49 Å
c	14.87 Å
α	90°
β	90.12°
γ	90°

Table 4: Structural Paramaters of 1T $MoTe_2$

Element	x	y	z
Te	0.58	0	0.098
Te	0.09	1/2	0.138
Te	0.567	1/2	0.361
Te	0.063	0	0.401
Mo	0.28	0	0.069
Mo	0.32	1/2	0.506

3.15. Input Script

The input script is made of commands to be executed for the simulation. The feature lets a user change portion of the input script or add new interatomic constraints, diagnostics, potential files and to a model to make it fit their needs. The three most important things about flexibility:

(i) Flexibility through input script: Tailoring without coding

(ii) Flexibility through source code: Adding codes to extend performance capability.

iii) The flexibility by using reference library of LAMMPS

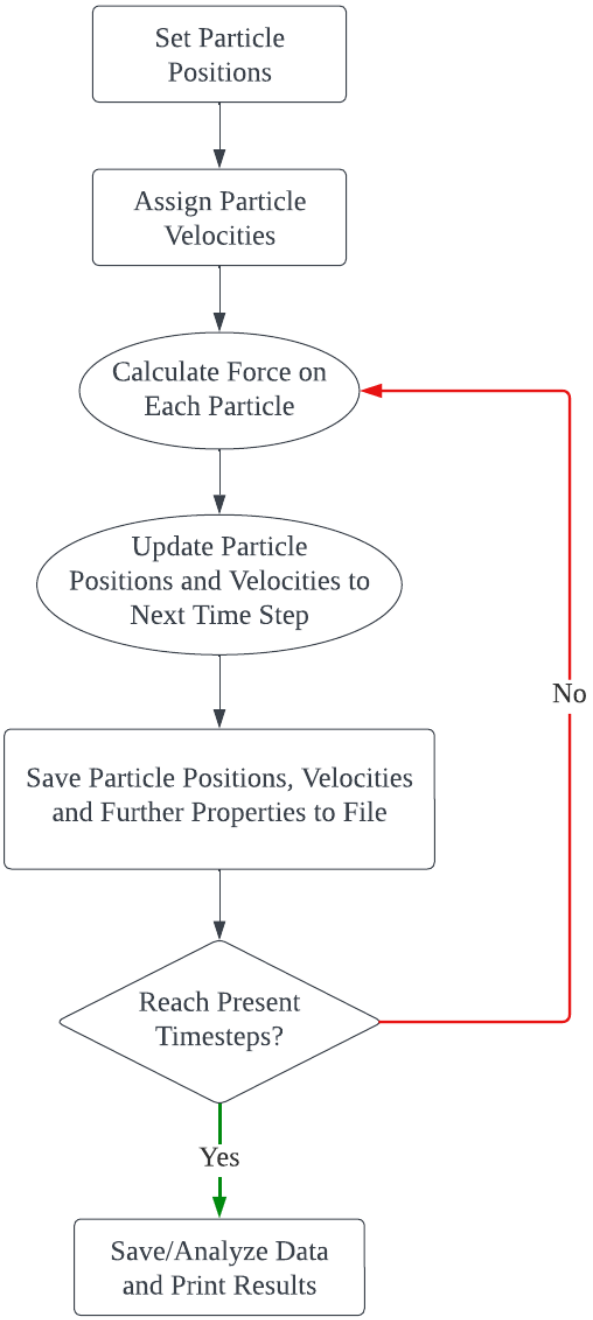

Figure 12: Flowchart of Molecular Dynamics Simulation

Employing cutting-edge setups of CPUs and GPUs equipped with multiple threads can significantly enhance computational performance. Incorporating algorithms such as the rendezvous algorithm [99] proves beneficial in generating data decomposition, allowing processors situated at entry and exit points to efficiently locate intermediate data. This facilitates the distribution of computational tasks across a substantial computer system, thereby optimizing resource utilization. To execute simulations on multiple CPUs utilizing parallel computing capabilities, the LAMMPS software can be integrated with the MPI parallel protocol. This protocol facilitates seamless communication and data exchange among processors, enabling collaborative

execution of intricate calculations and simulations. Through the synergistic employment of advanced hardware, efficient data decomposition algorithms, and the MPI parallel protocol in LAMMPS, computational simulations are accelerated, enabling researchers to tackle complex scientific challenges and attain results in a time-efficient manner.

Iterative simulations can be used to test different conditions in molecular dynamics (MD) simulations. First, the right ensemble format is used with a set of governing equations. In NPT ensemble, everything else stays the same except for the volume. NVE, NPH and NVT ensembles are some ensembles commonly used in LAMMPS. The next part is the boundary conditions. Boundary conditions can periodic or non-periodic. The periodic boundary condition maintains the material within a single box, which can be reproduced indefinitely in all dimensions. Other information includes settings for thermosetting, control of pressure, harmonic constraints, bond angle constraints, and so on.

MD uses time integration algorithms to run simulations . The algorithm combines the equations that describe how moving atoms affect each other and makes their path. A velocity verlet integrator, a rigid body integrator, are instances of well-known integrators that are used in LAMMPS.

After adding randomness to break up the symmetry of the material, the simulation starts. LAMMPS executes one command line at a time in a sequence shown in the flowchart in Figure 9. When the simulation is finished, the simulator gives us two distinct files. The calculations for each atom is found in a log file. This data file needs to be worked on before graphs and other empirical relationships can be derived from it. The video of the whole simulation process is in another file. The video can be played with OVITO [100], which is a 3D visualization program that processes the atomistic data after it has been collected.

3.16. Governing Equations

The stress is calculated using Eq. 7 :

$$\sigma = \frac{P_{xx} * L_y * L_z}{L_{y0} * L_{z0}} \tag{7}$$

P_{xx} *is the Tensile load*

The strain is calculated using Eq. 8 :

$$\varepsilon = \frac{L_x - L_{x0}}{L_{x0}} \tag{8}$$

L_x $-$ *instantenous length of* $MoTe_2$ *along x axis.*

L_{x0} $-$ *undeformed length of* $MoTe_2$ *along x axis.*

The stress generated was divided by the thickness to determine the plane stress, as outlined in Eq. 9 :

$$Planar\ Stress = \frac{Stress}{thickness} \tag{9}$$

3.17. Interatomic Potential

Interatomic potential file information regarding the interaction between atoms such as the attraction as well as the repulsion force that act between 2 atoms as well as between atoms and molecules. The possible interaction between atoms are shown in Figure 12. There are different interatomic potentials developed that are used in different fields. AIREBO, REBO, Morse, Lennard Jones, Stillinger Weber are a few of these interatomic potentials.

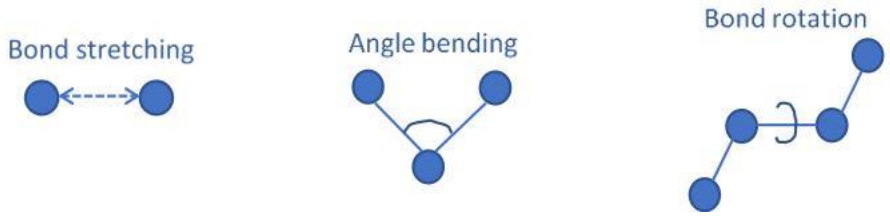

Figure 13: Interaction between bonds

3.18. Stillinger Weber Potential

For our molecular dynamics simulation, we applied Stillinger Weber potential. This potential is computationally cheap as well as more accurate than some other potentials like Lennard jones. The virial theorem gives a general equation that shows how the average total kinetic energy of settled system comprised of distinct particles held together by potential forces corresponding to the system's total potential energy. Atomic Stress for the system was calculated based on virial stress.

Components for virial stress [101] can be calculated using Eq. 10 [102][95].

$$\sigma_{\text{Virial}}(r) = \frac{1}{\Omega}\sum_{\text{i}}\left[\left(-m_i\dot{u}_i \bigotimes \dot{u}_i + \frac{1}{2}\sum_{j\neq \text{i}} r_{\text{i}j} \otimes f_{ij}\right)\right] \tag{10}$$

The mathematical expressions used to calculate the components of the virial stress.:

$$\phi = \sum_{\text{i}<j} V_2 + \sum_{\text{i}>j<k} V_3 \tag{11}$$

$$V_2 = Ae^{\left[\frac{\rho}{r-r_{max}}\right]}\left(\frac{B}{r^4} - 1\right) \tag{12}$$

$$V_3 = K\varepsilon e^{\frac{\rho_1}{r_{ij}-r_{maxij}} - \frac{\rho_2}{r_{ik}-r_{maxik}}}(\cos\theta - \cos\theta_0)^2 \tag{13}$$

Here,

$\Omega - Summation\ of\ total\ volume\ occupied\ by\ atoms$

, $r_{ij} - Reference\ Position\ of\ i\ atom\ with\ respect\ to\ j$

$\otimes - Cross\ Product$

$f_{ij}\ -Interatomic\ Force\ on\ i\ atom\ exerted\ by\ j\ atom$

$r_{max}, r_{maxij}, r_{maxik} - Cutoff\ Ratios$

$\theta_0 - Angle\ between\ two\ bonds\ at\ equilibrium\ position$

$\phi - One\ of\ the\ constituents\ of\ virial\ stress$

$V_2, V_3 - Two\ body\ angle\ bending\ and\ bond\ stretching\ terms$

$A - Energy\ Parameter$

$K -\ Energy\ Parameter.$

3.19. Defect Engineered Structures

Defect engineering is a complicated process that is used to induce vacancy as well as change the shape and volume of target compounds. Defects might have different kind of effects on the target structure's mechanical behaviour that we want to study. In this study, the effect of five types of defects on the mechanical properties of 2H and 1T $MoTe_2$ was examined through molecular dynamics simulations. Specifically, 2H and 1T $MoTe_2$ structures with the following defects were considered: (i) 1 Molybdenum 6 Tellurium Vacancy, (ii) 2 Tellurium Vacancy, (iii) 4 Tellurium Vacancies, (iv) a line vacancy defect along the armchair axis, and (v) a line vacancy defect along the zigzag axis. The top view of all the defective structures of 2H $MoTe_2$ and 1T $MoTe_2$ used for the simulation is shown in Figure 14 and 15, respectively.

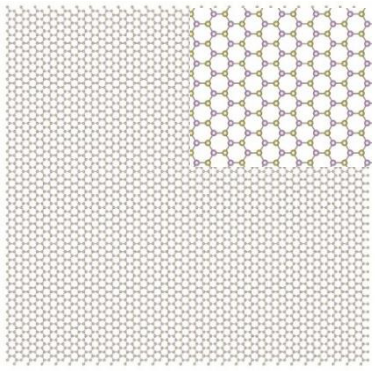

(a)

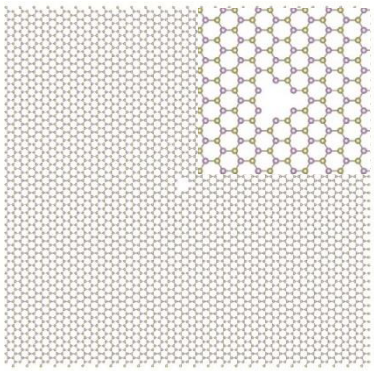

(b)

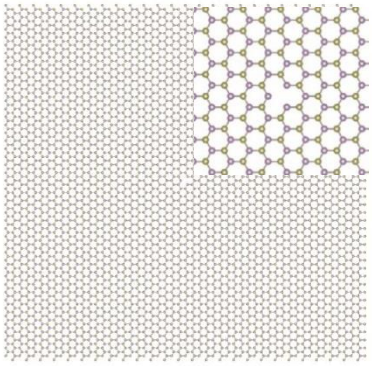

(c)

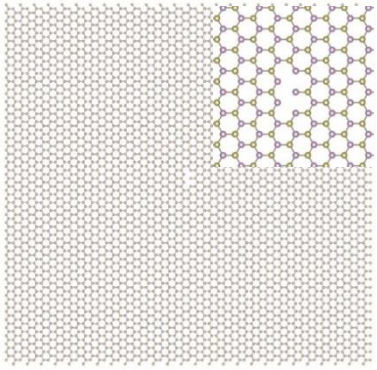

(d)

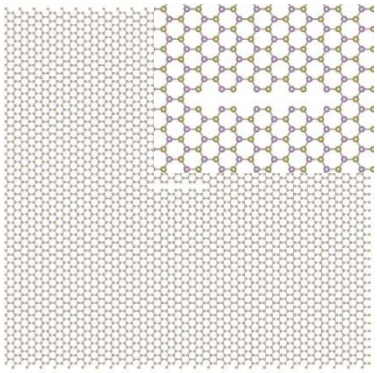

(e)

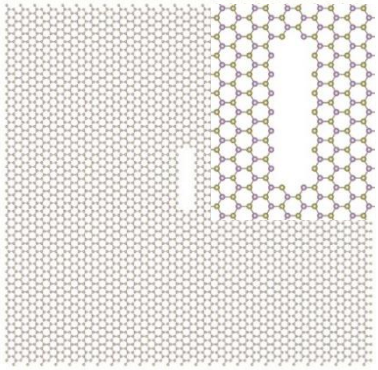

(f)

Figure 14 : Molecular Structure of 2H $MoTe_2$ with (a) Pristine structure (b) 2 Tellurium vacancy (c) 4 Tellurium vacancy (d) 6 Tellurium vacancy accompanied with one Molybdenum vacancy (e) Line vacancy defect along armchair axis (f) Line vacancy defect along zigzag axis

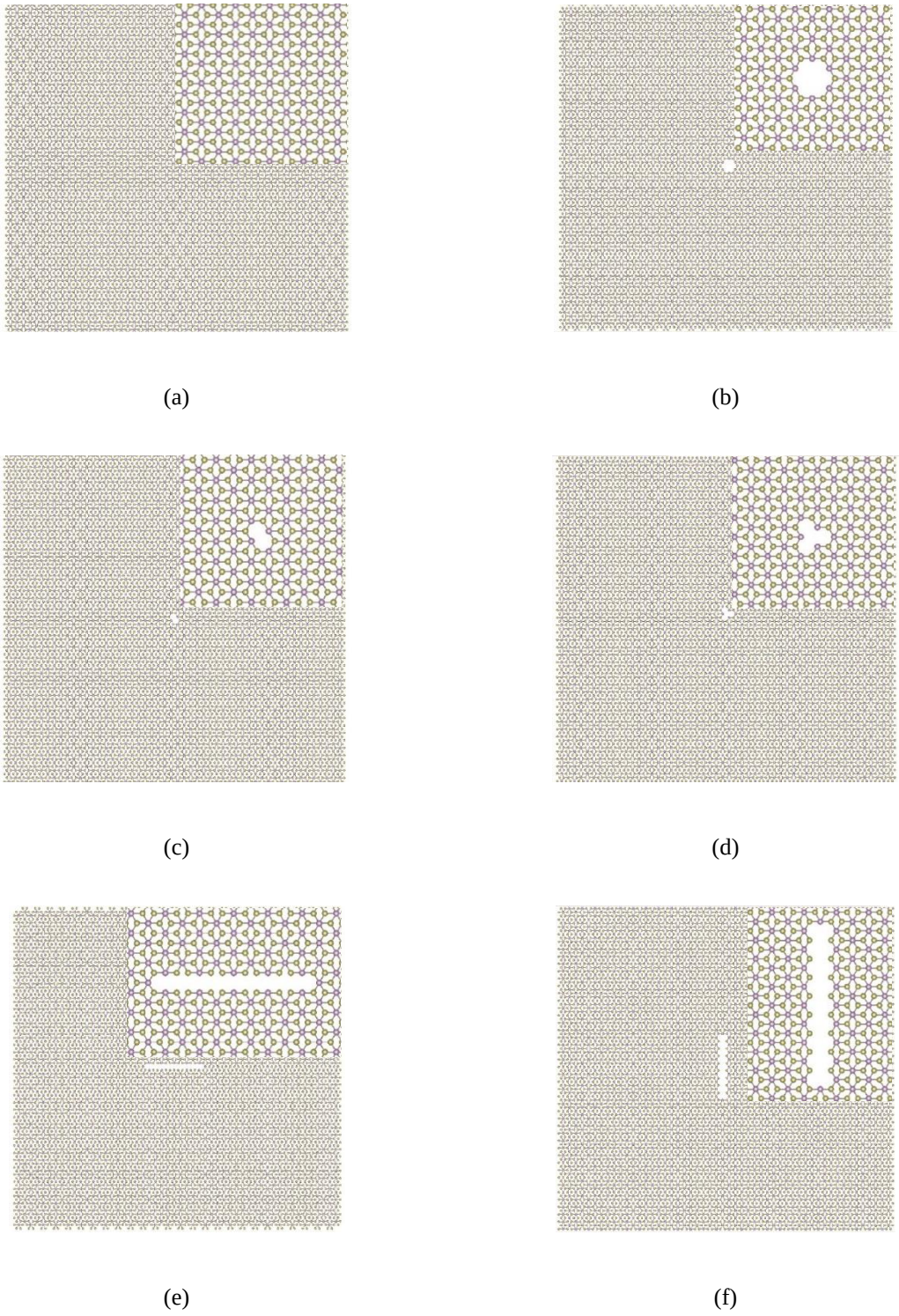

Figure 15: Molecular Structure of 2H $MoTe_2$ with (a) Pristine structure (b) 2 Tellurium vacancy (c) 4 Tellurium vacancy (d) 6 Tellurium vacancy accompanied with one Molybdenum vacancy (e) Line vacancy defect along armchair axis (f) Line vacancy defect along zigzag axis

The Defective structures were prepared in VESTA by deleting atoms to get desired defect induced structures. After obtaining the defect-induced structures in VESTA, the file was converted into an LMP file for utilization in LAMMPS simulation. The inclusion of these defects can significantly alter the mechanical characteristics of $MoTe_2$, and understanding their impact is crucial for optimizing the performance of $MoTe_2$-based devices. By conducting molecular dynamics simulations of uniaxial and biaxial tensile tests on these defect-containing structures, insights into the mechanical behavior of $MoTe_2$ under different loading conditions is gained, and the role of defects in governing its properties is better understood.

3.20. Validation

Once the atomic structure of the material has been prepared, the subsequent step involves conducting the planned simulation experiments. However, prior to commencing the experiments, it is imperative to ensure the code and file structure align with the established standards and reproduce the accepted results documented in reputable journals. This serves the purpose of validating the simulation setup by comparing it against previous research. By examining the accuracy and consistency of the codes and files, it becomes feasible to utilize the existing simulation setup.

The simulations were specifically conducted to probe the uniaxial tensile response of pristine samples of both phases of $MoTe_2$ in both the armchair and zigzag directions, as illustrated in Figure 16. Two different temperatures, namely 1K and 300K, were employed during the simulations. Following the completion of the simulations, the stress-strain responses were plotted, and these plots were subsequently validated by comparing them to the plots published by Jiang et al [62]. This validation process serves as a crucial step in ensuring the reliability and accuracy of the simulation results obtained in this study, thereby establishing a solid foundation for further analysis and interpretation.

3.21. Validation of 2H $MoTe_2$ Pristine Sample

Figure 17 and 18 showcase the stress strain plot for single-layer 2H-$MoTe_2$ of 10 nm × 10 nm along armchair and zigzag axes [62]. This plot in Figure 17 is depicted in Jiang et al. The same test was conducted using our code in LAMMPS, and the data was post-processed in MS Excel to obtain the plot shown in Figure 18. It was observed that the stress-strain response obtained in our study is consistent with the findings reported in the literature (see Table 5).

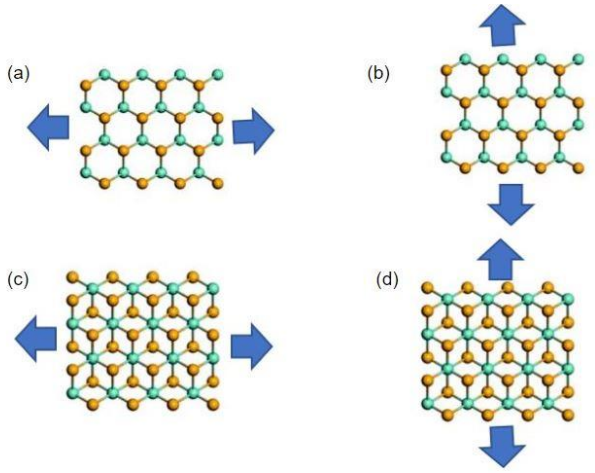

Figure 16: Force is applied for 2H $MoTe_2$ in (a) Armchair (b) Zigzag Axes for 1T $MoTe_2$ in (a) Armchair (b) Zigzag Axes

Table 5: Young's Modulus, Fracture Strength and Ultimate Tensile Strength values of 2H $MoTe_2$ at 1K and 300K temperatures when strain is applied in armchair and zigzag direction were obtained in our present study is compared with literature standard.

Temperature	2H $MoTe_2$									
	Strain-Armchair					Strain-Zigzag				
	Y_m (N/m)			FS (%)	UTS (N/m)	Y_m (N/m)			FS (%)	UTS (N/m)
	Present Study	Ref [62]	Ref [59]			Present Study	Ref [62]	Ref [59]		
1K	79.12	79.8	79.4	25.39	11.6	78.67	79.8	79.4	29.49	11.14
300K	75.01	79.8	79.4	17.34	9.8	74.35	79.8	79.4	19.05	9.61

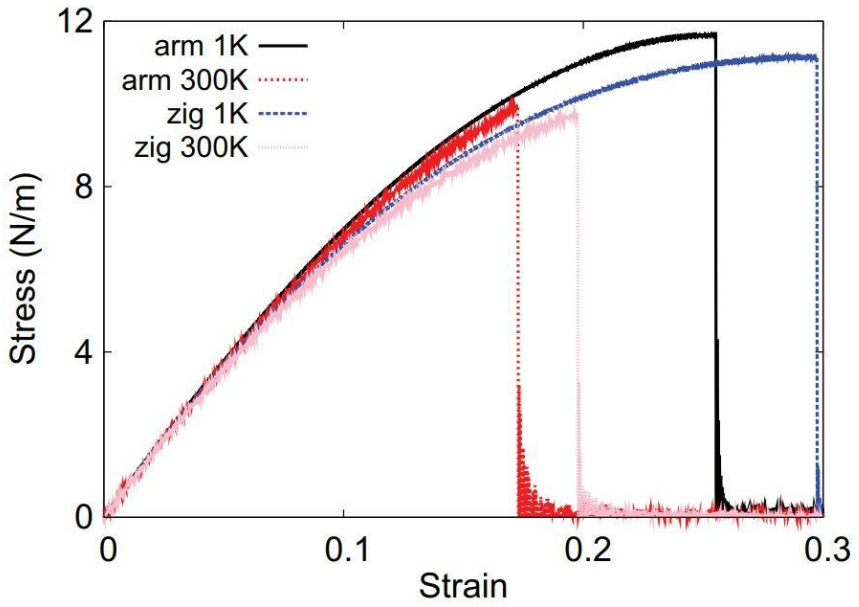

Figure 17: Stress-strain plot for single-layer 2H-$MoTe_2$ of 10 nm × 10 nm along armchair and zigzag axes [62].

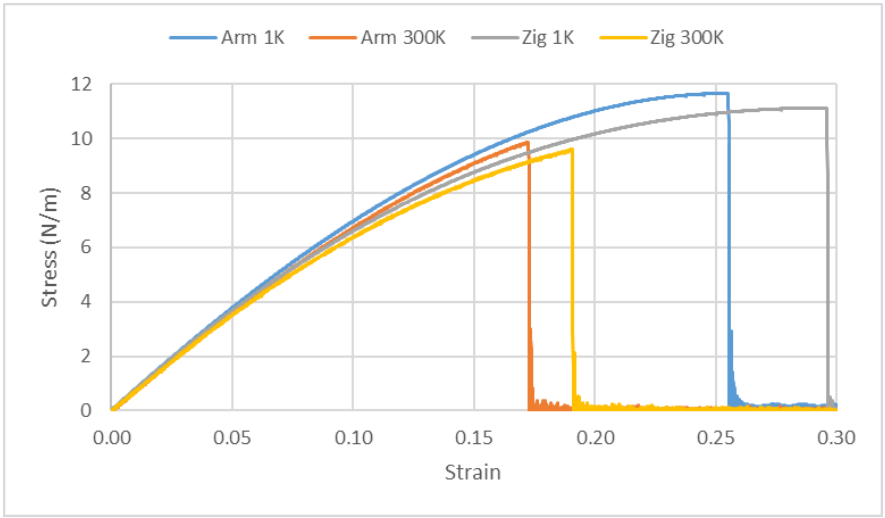

Figure 18:Stress-strain plot for single-layer 2H-$MoTe_2$ of 10 nm × 10 nm along armchair and zigzag axes from present study.

3.22. Validation for 1T $MoTe_2$ Pristine Sample

Figure 19 and 20 shows the stress strain plot for single-layer 1T-$MoTe_2$ of 10 nm × 10 nm along armchair and zigzag axes [62]. This plot in Figure 19 is depicted in Jiang et al. By utilizing our code in LAMMPS, we executed the identical test and obtained the stress-strain plot shown in Figure 20 after processing the data in MS Excel. The stress-strain response we obtained was found to be consistent with the findings documented in the literature (see Table 6).

Table 6: Young's Modulus, Fracture Strength and Ultimate Tensile Strength values of 1T $MoTe_2$ at 1K and 300K temperatures when strain is applied in armchair and zigzag direction were obtained in our present study is compared with literature standard.

Temperature	1T $MoTe_2$									
	Strain-Armchair					Strain-Zigzag				
	Y_m (N/m)			FS (%)	UTS (N/m)	Y_m (N/m)			FS (%)	UTS (N/m)
	Present Study	Ref [62]	Ref [103]			Present Study	Ref [62]	Ref [103]		
1K	80.57	81.6	92	13.93	6.03	80.09	81.2	92	16.45	6.02
300K	64.42	81.6	92	7.72	4.24	64.04	81.2	92	8.11	4.19

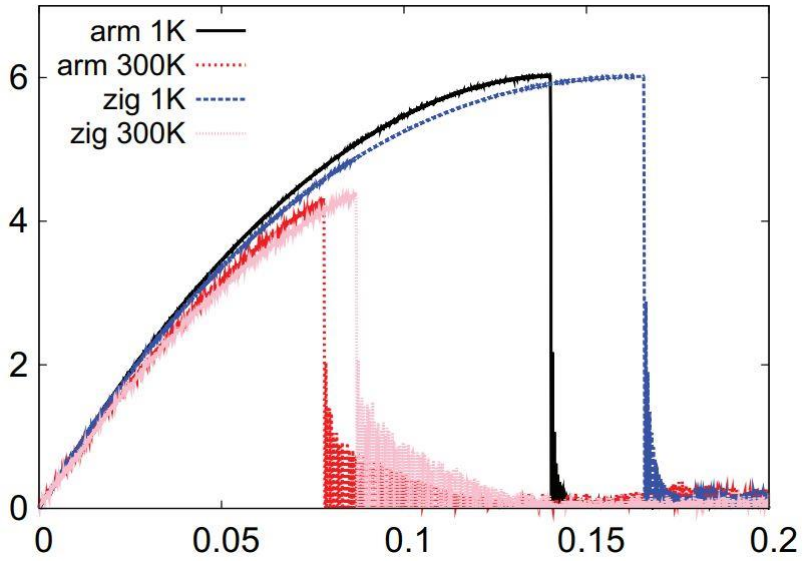

Figure 19: Stress-strain plot for single-layer 1T-$MoTe_2$ of 10 nm × 10 nm along armchair and zigzag axes [62]

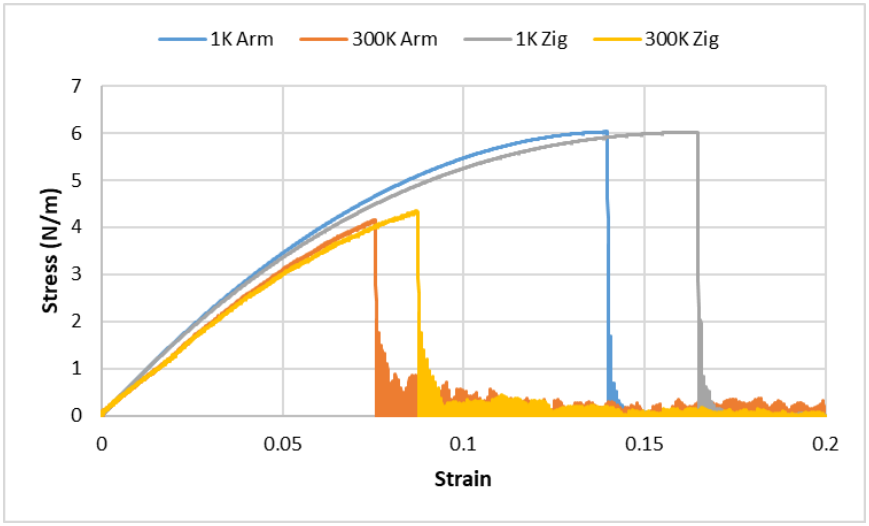

Figure 20: Stress-strain plot for single-layer 1T-$MoTe_2$ of 10 nm × 10 nm along armchair and zigzag axes from present study.

CHAPTER 4: RESULTS AND DISCUSSION

4.1. Exploration into Mechanical Behaviour of Defective $MoTe_2$

The elastic properties of pristine $MoTe_2$ in both phases were confirmed by comparing them with previous studies. Subsequently, Molecular Dynamics simulations were carried out using LAMMPS to investigate the mechanical behavior of defect induced $MoTe_2$. Uniaxial and biaxial tensile tests were performed on the structures of both 2H and 1T $MoTe_2$ during the simulations. The defective structures considered in the simulations included various types of vacancies: 2 Tellurium atom vacancies, 4 Tellurium atom vacancies, and 6 Tellurium atom vacancies accompanied by 1 Molybdenum atom vacancy, line defect along armchair axis and line defect along zigzag axis for both phases. The simulation codes were successfully converged, and the resulting stress-strain responses were plotted using Excel.

4.2. Uniaxial Tensile Test

The uniaxial tensile test is a mechanical testing technique that involves applying a stretching force to a material in one direction while keeping it fixed in all other directions. The LAMMPS software was utilized in this investigation to perform uniaxial tensile tests on monolayers of 2H and 1T $MoTe_2$. The simulation was conducted by applying stress opposite ends of the $MoTe_2$ sheet to simulate the uniaxial stretching process. Throughout the simulation, the stress and strain trends were monitored and recorded to generate the stress vs strain curve for the material. This allowed us to investigate the mechanical properties of 2H and 1T $MoTe_2$, such as their ultimate strength and elastic modulus, when subjected to uniaxial tension. These results were compared (see Figure 21-32, Table 7,8) to those obtained from the biaxial tensile tests (see Figure 33-44, Table 9,10) to enhance our comprehension of the mechanical response of the materials.

Table 7: Mechanical Properties of 2H SL$MoTe_2$ determined using uniaxial tensile test at 300K

	2H $MoTe_2$					
	Strain-Armchair			**Strain-Zigzag**		
	Y_m (N/m)	**FS (%)**	**UTS (N/m)**	**Y_m (N/m)**	**FS (%)**	**UTS (N/m)**
Pristine 2H $MoTe_2$	75.01	17.24	9.88	74.35	19.04	9.61
2 Te Vacancy $MoTe_2$	74.97	12.91	8.19	74.31	13.79	8.03
4 Te Vacancy $MoTe_2$	74.68	10.14	6.79	74.22	15.69	8.69
1 Mo 6 Te Vacancy $MoTe_2$	74.94	13.59	8.48	71.19	7.16	4.65
$MoTe_2$ with Line Defect along Armchair axis	74.94	13.59	8.48	71.19	7.16	4.65
$MoTe_2$ with Line Defect along Zigzag axis	70.68	6.50	4.37	73.43	10.77	6.67

Table 8: Mechanical Properties of 2H SL$MoTe_2$ determined using uniaxial tensile test at 300K

	1T $MoTe_2$					
	Strain-Armchair			**Strain-Zigzag**		
	Y_m (N/m)	**FS (%)**	**UTS (N/m)**	**Y_m (N/m)**	**FS (%)**	**UTS (N/m)**
Pristine 2H $MoTe_2$	64.03	7.72	4.24	64.04	8.10	4.19
2 Te Vacancy $MoTe_2$	64.48	5.84	3.51	64.14	7.31	3.93
4 Te Vacancy $MoTe_2$	64.46	5.17	3.17	63.83	6.24	3.54
1 Mo 6 Te Vacancy $MoTe_2$	64.28	5.4	3.29	64.00	5.35	3.16
$MoTe_2$ with Line Defect along Armchair axis	64.15	6.67	3.85	60.60	3.41	2.07
$MoTe_2$ with Line Defect along Zigzag axis	60.08	3.13	1.93	63.48	6.53	3.66

Figure 21 to 26 presents the stress-strain plots obtained from the LAMMPS uniaxial tensile test simulations conducted on 2H $MoTe_2$. Figure 21 illustrates the stress-strain plot for the pristine 2H $MoTe_2$ structure. On the other hand, Figures 22 to 26 depict the stress-strain plots for the five different defective structures that were investigated in this study.

Analyzing the stress-strain plots for the point defects, it was observed that as the number of vacancies increased, the ultimate tensile strength decreased. This indicates that the presence of vacancies within the $MoTe_2$ structure affects its mechanical strength. Additionally, a decrease in the fracture strain was observed in conjunction with the increase in the number of vacancies. This suggests that the presence of vacancies also influences the material's ability to withstand deformation before failure.

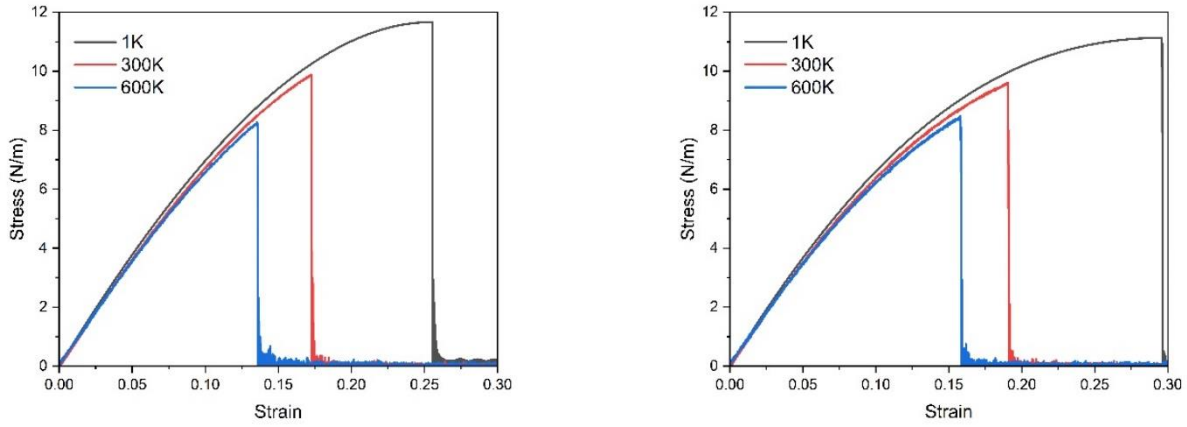

(a) (b)

Figure 21: The uniaxial tensile stress–strain curves of Pristine 2H $SLMoTe_2$ at different temperatures of 1K, 300K and 600K in (a) armchair, and (b) zigzag directions.

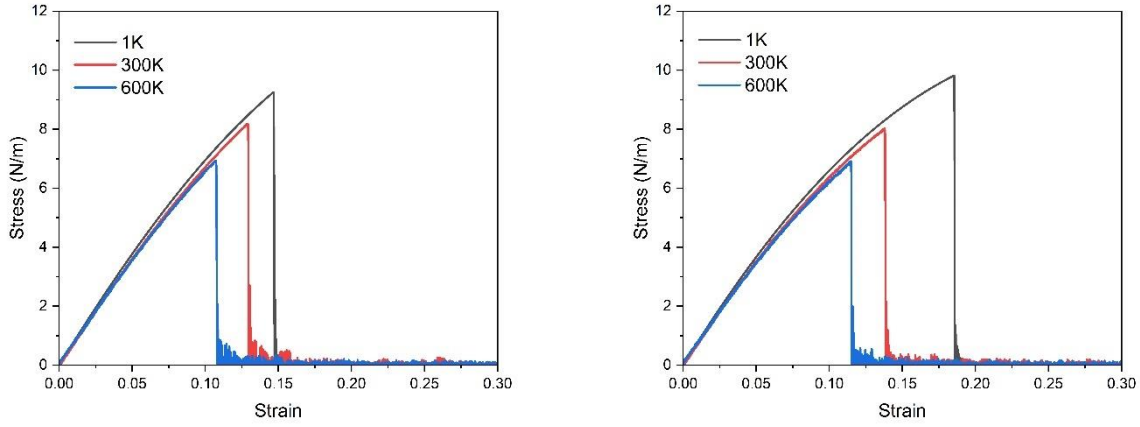

(a) (b)

Figure 22:The uniaxial tensile stress–strain curves of 2H SLMoTe$_2$ with 2 Tellurium vacancy at different temperatures of 1K, 300K and 600K in (a) armchair, and (b) zigzag directions.

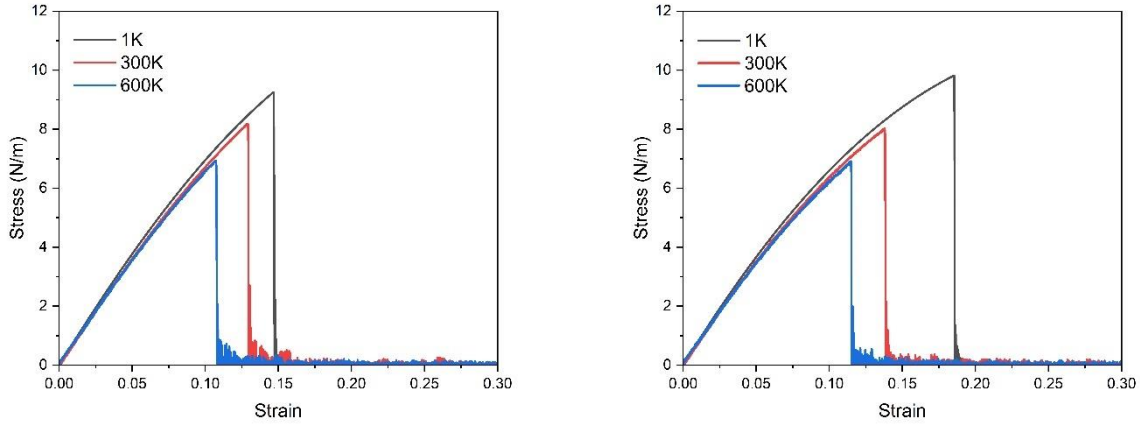

(a) (b)

Figure 23:The uniaxial tensile stress–strain curves of 2H SLMoTe$_2$ with 4 Tellurium vacancy at different temperatures of 1K, 300K and 600K in (a) armchair, and (b) zigzag directions.

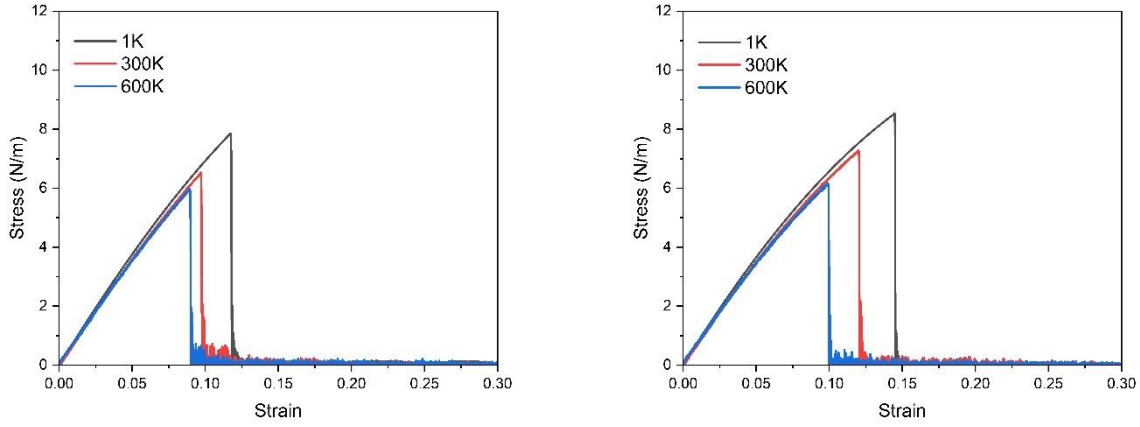

(a) (b)

Figure 24: The uniaxial tensile stress–strain curves of 2H $SLMoTe_2$ with 1 Molybdenum 6 Tellurium vacancy pre-crack in armchair direction at different temperatures of 1K, 300K and 600K in (a) armchair, and (b) zigzag directions.

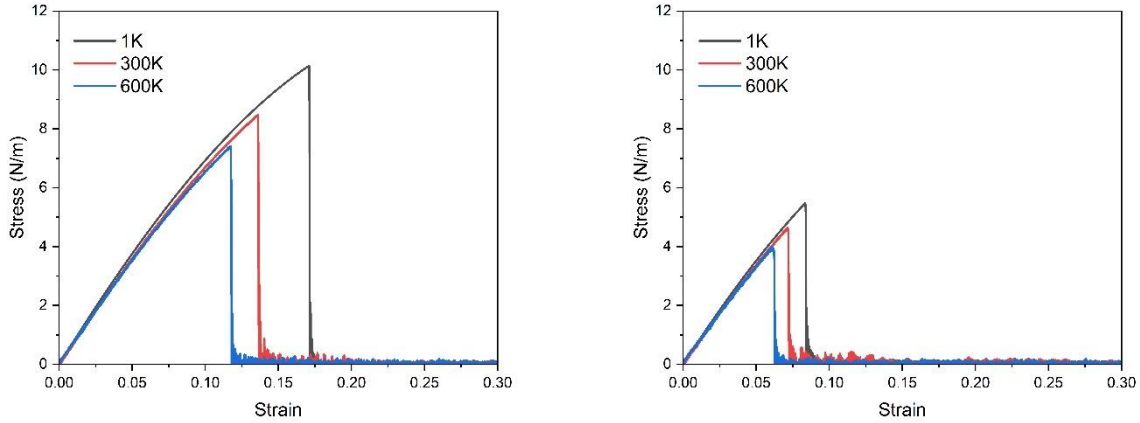

(a) (b)

Figure 25: The uniaxial tensile stress–strain curves of 2H $SLMoTe_2$ with pre-crack in armchair direction at different temperatures of 1K, 300K and 600K in (a) armchair, and (b) zigzag directions.

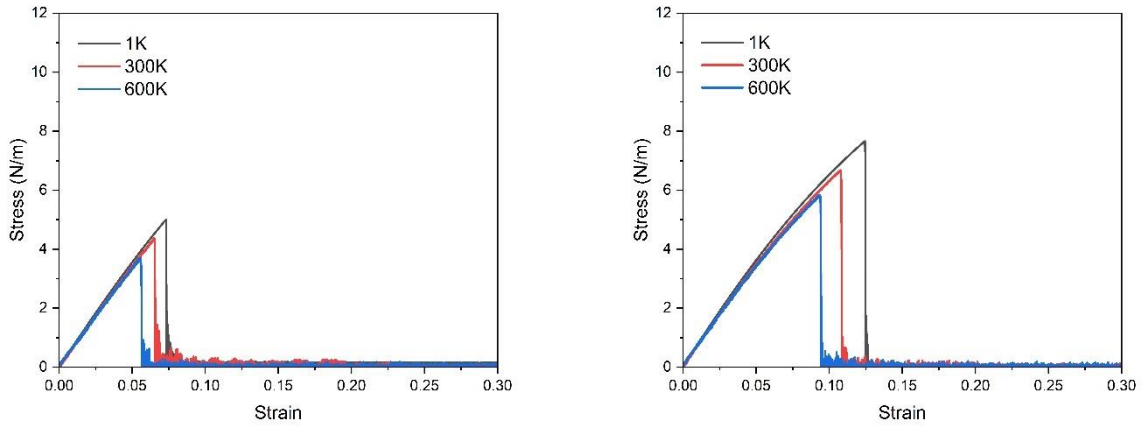

(a) (b)

Figure 26: The uniaxial tensile stress–strain curves of 2H SL$MoTe_2$ with pre crack in zigzag direction at different temperatures of 1K, 300K and 600K in (a) armchair, and (b) zigzag directions.

Figures 27 to 32 display the stress-strain plots obtained from the LAMMPS uniaxial tensile test simulations conducted on 1T $MoTe_2$. Figure 27 specifically illustrates the stress-strain plot for the pristine 1T $MoTe_2$ structure. Meanwhile, Figures 28 to 32 showcase the stress-strain plots for the five different defective structures examined in this study.

Upon analyzing the stress-strain plots for the point defects in 1T $MoTe_2$, observations were made. As the number of vacancies increased, a corresponding decrease in the ultimate tensile strength was observed. This suggests that the presence of vacancies within the 1T $MoTe_2$ structure has a detrimental effect on its mechanical strength. Moreover, a decrease in the fracture strain was also observed alongside the increase in the number of vacancies. This indicates that the presence of vacancies influences the material's capability to withstand deformation before failure.

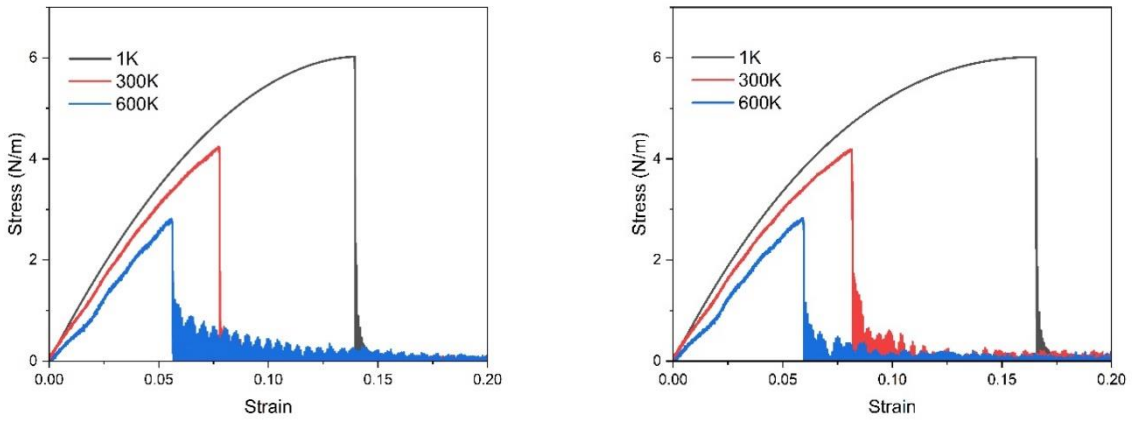

(a) (b)

Figure 27: The uniaxial tensile stress–strain curves of pristine 1T SLMoTe$_2$ at different temperatures of 1K, 300K and 600K in (a) armchair, and (b) zigzag directions.

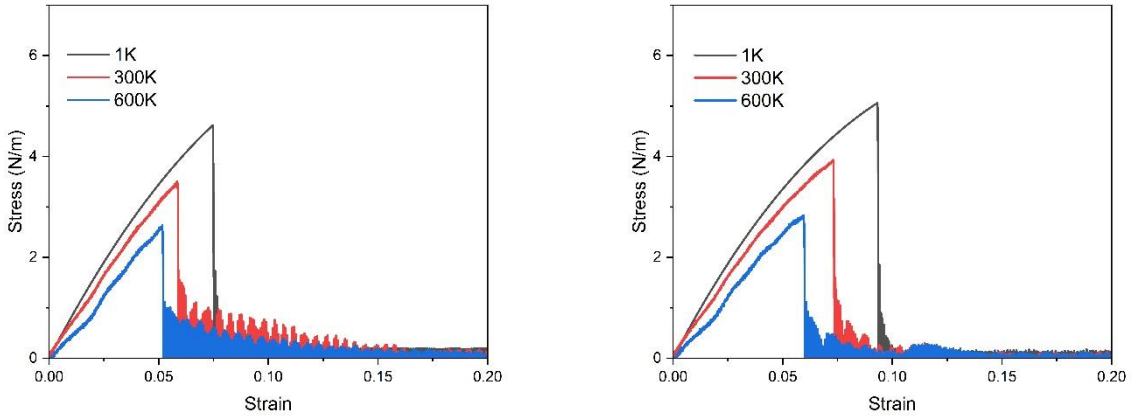

(a) (b)

Figure 28: The uniaxial tensile stress–strain curves of 1T SLMoTe$_2$ with 2 Tellurium vacancy at different temperatures of 1K, 300K and 600K in (a) armchair, and (b) zigzag directions.

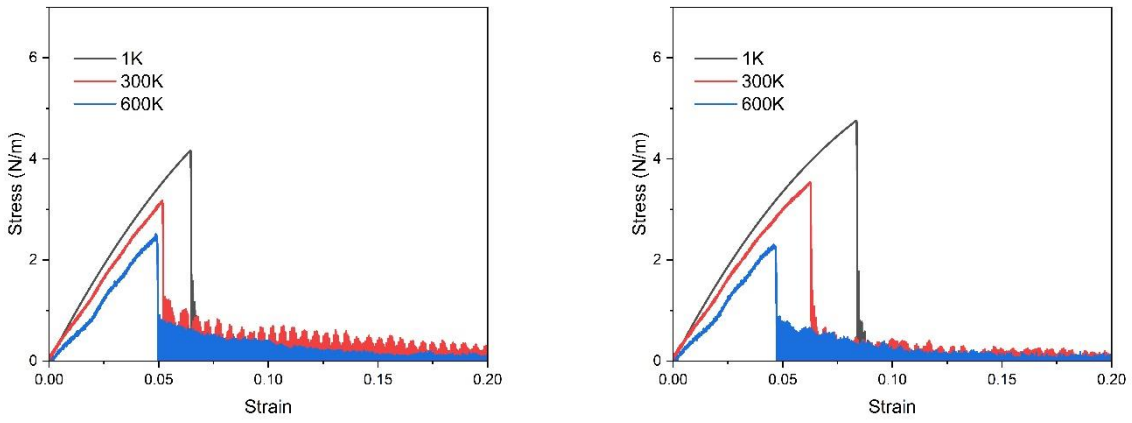

(a) (b)

Figure 29: The uniaxial tensile stress–strain curves of 1T SLMoTe$_2$ with 4 Tellurium vacancy at different temperatures of 1K, 300K and 600K in (a) armchair, and (b) zigzag directions.

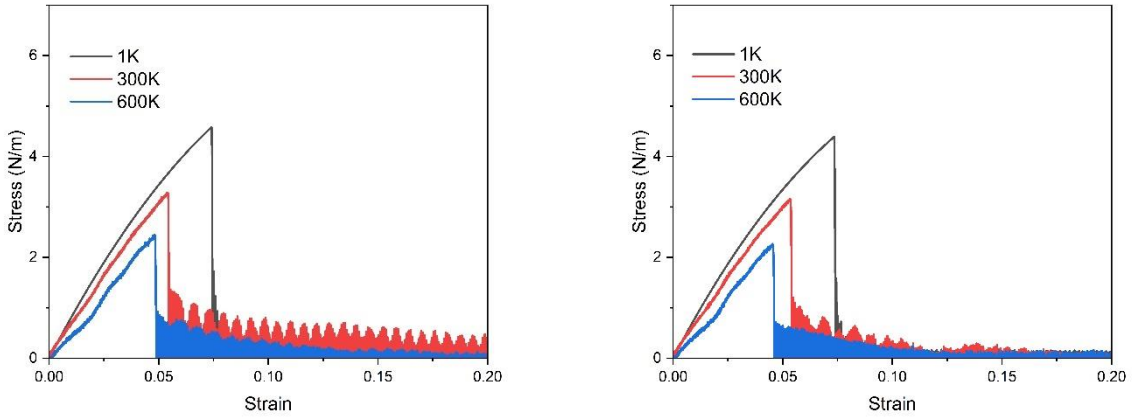

(a) (b)

Figure 30: The uniaxial tensile stress–strain curves of 1T SLMoTe$_2$ with 1 Molybdenum and 6 Tellurium vacancy at different temperatures of 1K, 300K and 600K in (a) armchair, and (b) zigzag directions.

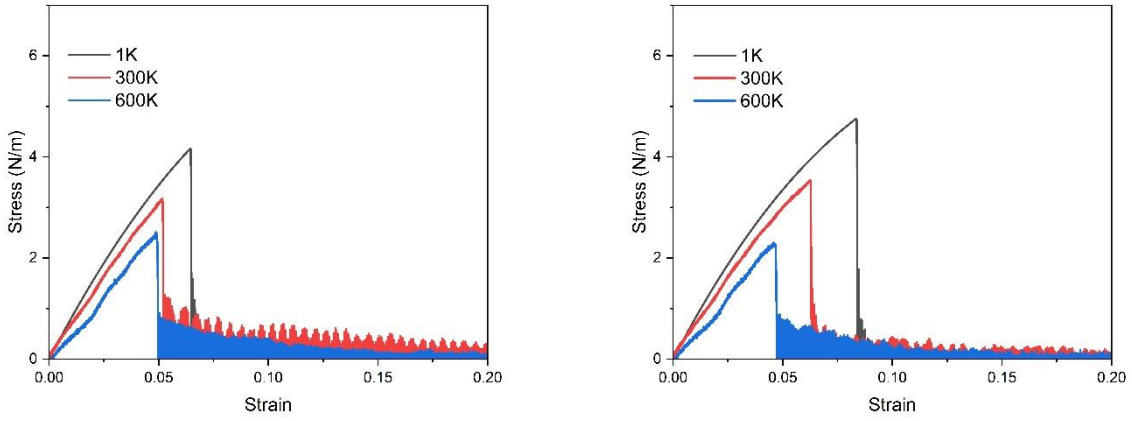

(a) (b)

Figure 31: The uniaxial tensile stress–strain curves of 1T $SLMoTe_2$ with 1 Molybdenum and 6 Tellurium vacancy at different temperatures of 1K, 300K and 600K in (a) armchair, and (b) zigzag directions.

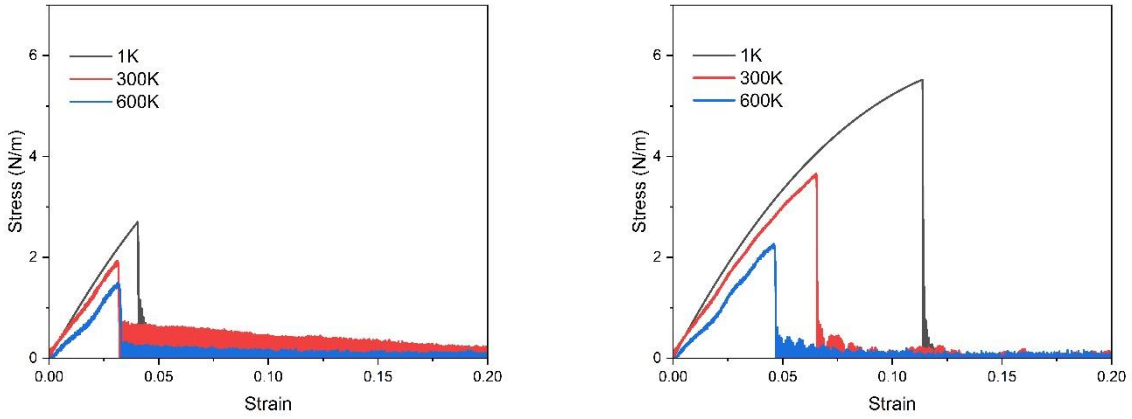

(a) (b)

Figure 32: The uniaxial tensile stress–strain curves of 1T $SLMoTe_2$ pre-crack in zigzag direction at different temperatures of 1K, 300K and 600K in (a) armchair, and (b) zigzag directions.

4.3. Biaxial Tensile Test

In the biaxial tensile test of 2H and 1T $MoTe_2$ using LAMMPS, the specimens were subjected to tensile stress in two perpendicular directions simultaneously. By performing such a test, we can gain insights into the material's mechanical properties within the plane, encompassing attributes like Young's modulus and fracture behavior when exposed to biaxial loading. During the simulations, a strain rate of 10^8/s was implemented, a range commonly observed in experimental settings, thus ensuring a realistic representation of the system. By graphing the stress and strain values collected throughout the simulation (illustrated in Figure 33-44), we were able to visualize and analyze the stress-strain response of the materials.

Table 9: Mechanical Properties of 2H SL$MoTe_2$ determined using biaxial tensile test

	2H $MoTe_2$					
	Strain-Armchair			**Strain-Zigzag**		
	Y_m (N/m)	**FS (%)**	**UTS (N/m)**	**Y_m (N/m)**	**FS (%)**	**UTS (N/m)**
Pristine 2H $MoTe_2$	98.50	15.09	7.86	98.94	15.10	7.85
2 Te Vacancy $MoTe_2$	98.41	11.97	7.29	99.03	11.97	7.29
4 Te Vacancy $MoTe_2$	97.37	8.53	6.10	98.58	8.52	6.12
1 Mo 6 Te Vacancy $MoTe_2$	97.72	9.4	6.47	98.89	9.41	6.46
$MoTe_2$ with Line Defect along Armchair axis	97.09	5.26	4.34	94.98	5.21	4.20
$MoTe_2$ with Line Defect along Zigzag axis	92.03	5.64	4.40	97.03	5.64	4.58

Table 10: Mechanical Properties of 2H SL$MoTe_2$ determined using biiaxial tensile test

	1T $MoTe_2$					
	Strain-Armchair			**Strain-Zigzag**		
	Y_m (N/m)	**FS (%)**	**UTS (N/m)**	**Y_m (N/m)**	**FS (%)**	**UTS (N/m)**
Pristine 2H $MoTe_2$	70.40	7.62	3.60	70.46	7.61	3.61
2 Te Vacancy $MoTe_2$	70.25	5.88	3.14	70.17	5.91	3.16
4 Te Vacancy $MoTe_2$	70.23	5.61	3.04	70.92	5.65	3.03
1 Mo 6 Te Vacancy $MoTe_2$	70.06	5.61	3.03	70.32	5.61	3.03
$MoTe_2$ with Line Defect along Armchair axis	70.31	3.27	2.05	67.08	3.23	1.92
$MoTe_2$ with Line Defect along Zigzag axis	65.71	3.16	1.88	70.58	3.24	2.03

By collecting stress and strain data throughout the simulations, we generated stress-strain plots to visualize and analyze the mechanical response of 2H $MoTe_2$ under biaxial tensile loading. Figure

33 depict the tress-strain plot for pristine structure, providing a comprehensive view of the material's behavior. The later ones Figure 34 to 38 are for defective 2H $MoTe_2$. These plots showcase the relationship between applied stress and resulting strain, highlighting the material's elastic and plastic deformation regions, as well as its ultimate failure point.

The stress-strain plots enable us to extract valuable information about the mechanical properties of 2H $MoTe_2$ subjected to biaxial tensile loading. By analyzing the slope of the stress-strain curve, we can determine the material's Young's modulus, which represents its stiffness. Moreover, the stress at the ultimate failure point and the corresponding strain provide insights into the material's fracture behavior and its ability to withstand biaxial loading.

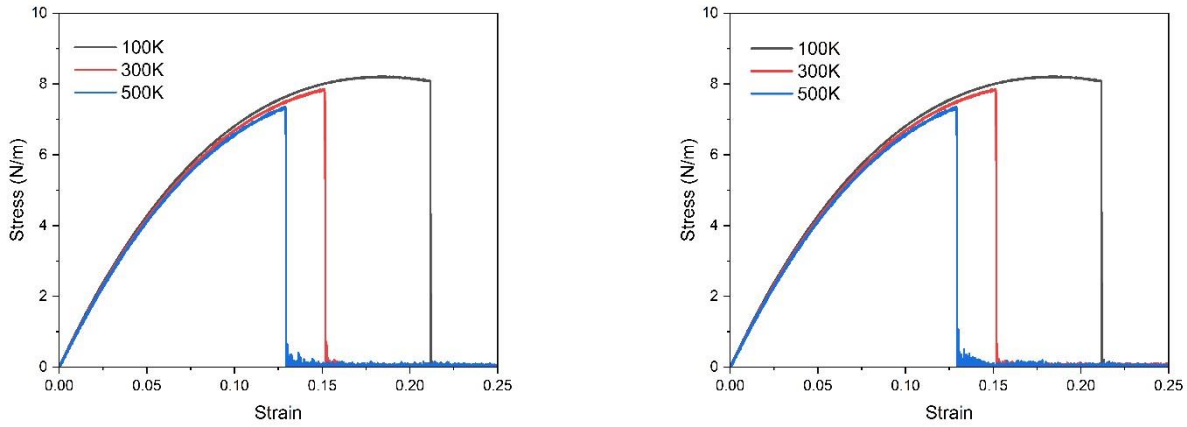

(a) (b)

Figure 33: The biaxial tensile stress–strain curves for pristine 2H $SLMoTe_2$ at different temperatures of 100,300 and 500 K in (a) armchair, and (b) zigzag directions.

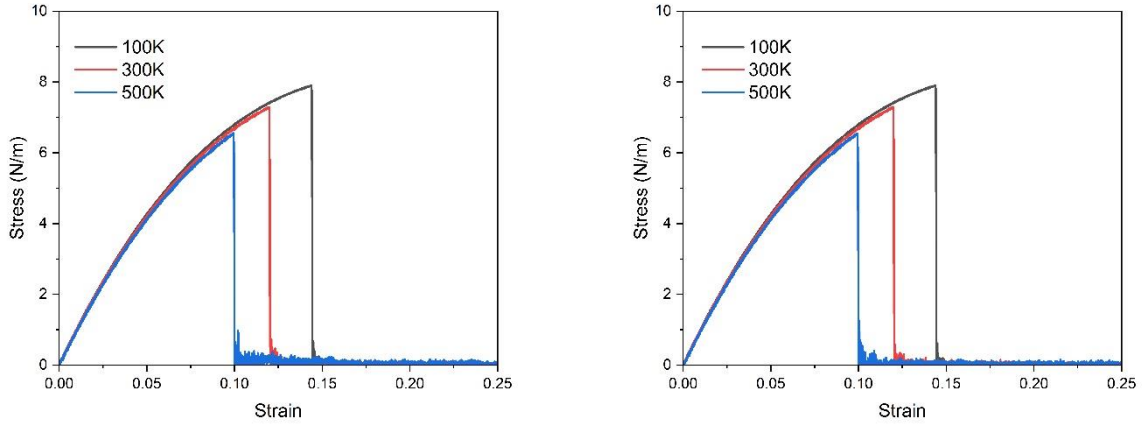

(a) (b)

Figure 34: The biaxial tensile stress–strain curves of 2H SLMoTe$_2$ with with 2 Tellurium vacancy at different temperatures of 100,300 and 500 K in (a) armchair, and (b) zigzag directions.

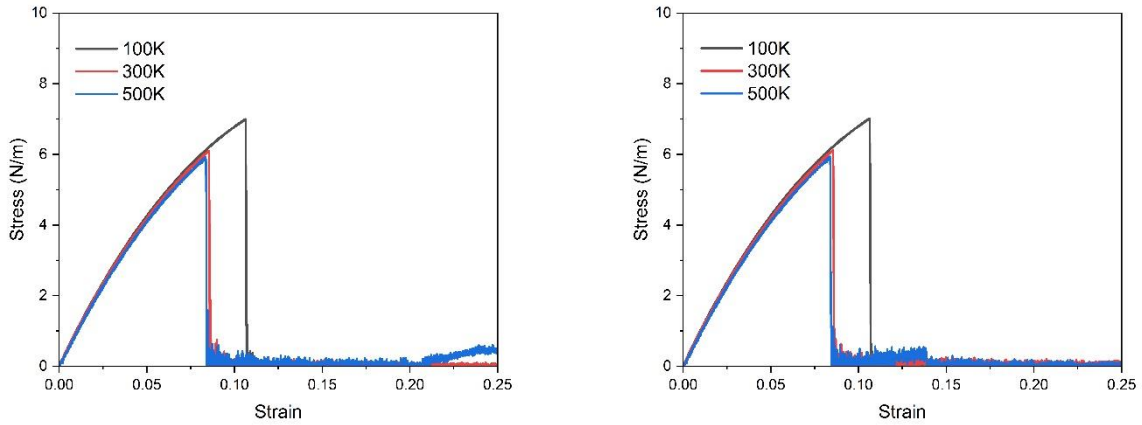

(a) (b)

Figure 35: The biaxial tensile stress–strain curves of 2H SLMoTe$_2$ with 4 Tellurium vacancy at different temperatures of 100,300 and 500 K in (a) armchair, and (b) zigzag directions.

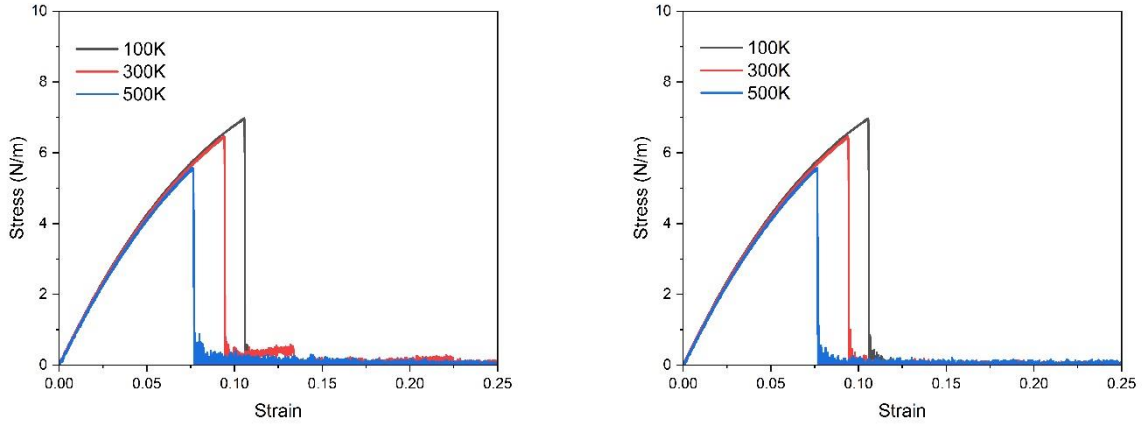

(a) (b)

Figure 36: The biaxial tensile stress–strain curves of 2H $SLMoTe_2$ with 1 Molybdenum and 6 Tellurium vacancy at different temperatures of 100,300 and 500 K in (a) armchair, and (b) zigzag directions.

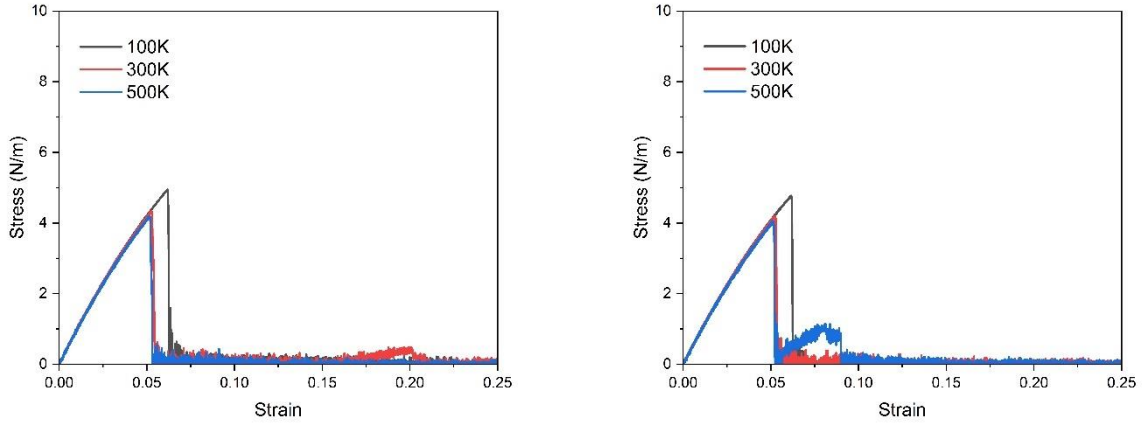

(a) (b)

Figure 37: The biaxial tensile stress–strain curves of 2H $SLMoTe_2$ with pre-crack in armchair direction at different temperatures of 100,300 and 500 K in (a) armchair, and (b) zigzag directions.

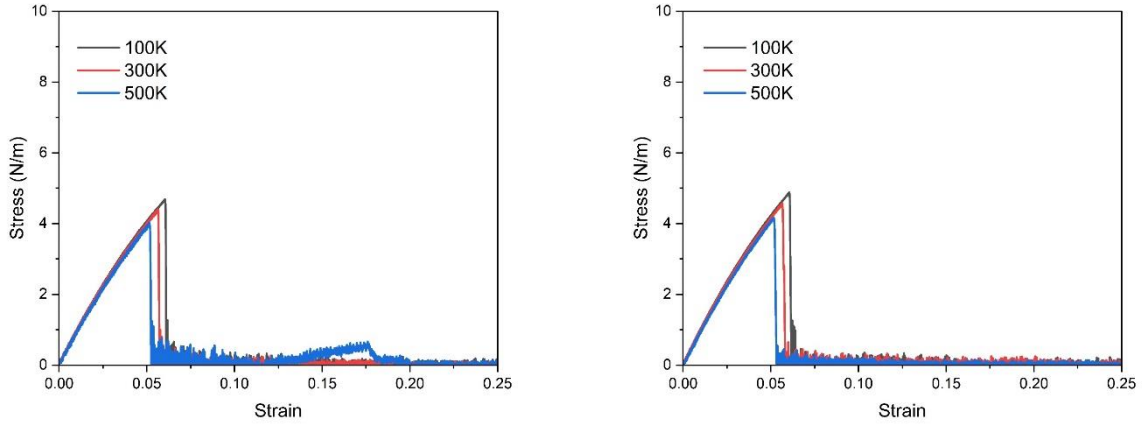

(a) (b)

Figure 38: The biaxial tensile stress–strain curves of 2H SL$MoTe_2$ with pre-crack in zigzag direction at different temperatures of 100,300 and 500 K in (a) armchair, and (b) zigzag directions.

The stress-strain response of 1T $MoTe_2$ under biaxial tensile loading was investigated through the collection of stress and strain data during the simulations. These data were used to generate stress-strain plots, allowing for a comprehensive analysis of the material's mechanical behavior. Figure 39 illustrates the stress-strain plot for the pristine 1T $MoTe_2$ structure, providing an overview of its response to biaxial tensile loading. Subsequent figures (Figure 39 to Figure 44) represent the stress-strain plots for defective 1T $MoTe_2$ structures, showcasing the material's elastic and plastic deformation regions, as well as its ultimate failure point.

The stress-strain plots serve as a valuable tool for extracting essential information about the mechanical properties of 1T $MoTe_2$ under biaxial tensile loading. By analyzing the slope of the stress-strain curve, the material's Young's modulus, which characterizes its stiffness, can be determined. Furthermore, the stress at the ultimate failure point and the corresponding strain provides insights into the fracture behavior of the material and its resistance to biaxial loading.

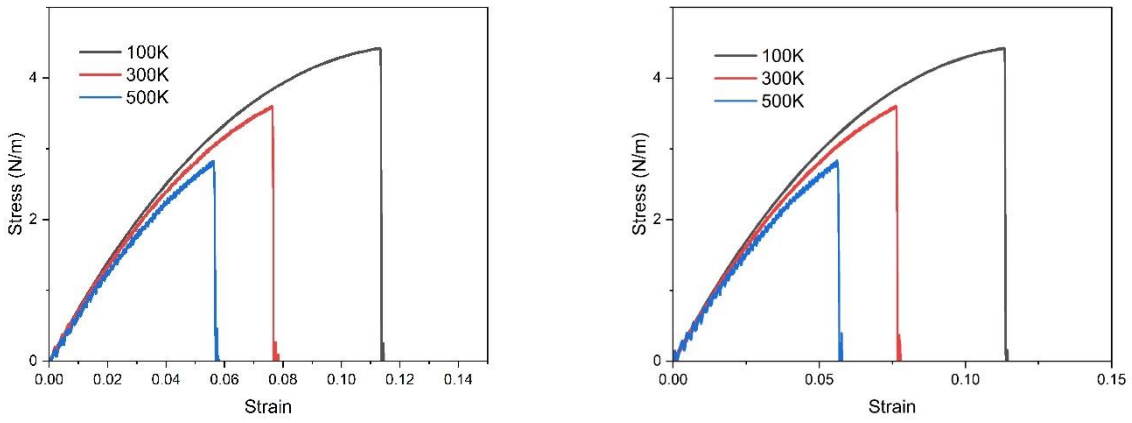

(a) (b)

Figure 39: The biaxial tensile stress–strain curves for pristine 1T SLMoTe$_2$ with at different temperatures of 100,300 and 500 K in (a) armchair, and (b) zigzag directions.

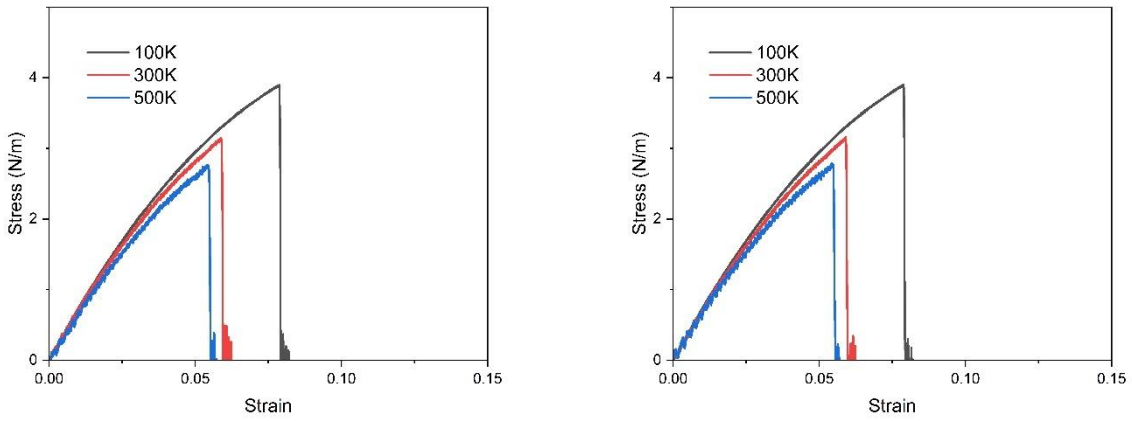

(a) (b)

Figure 40: The biaxial tensile stress–strain curves of 1T SLMoTe$_2$ with 2 Tellurium vacancy at different temperatures of 100,300 and 500 K in (a) armchair, and (b) zigzag directions.

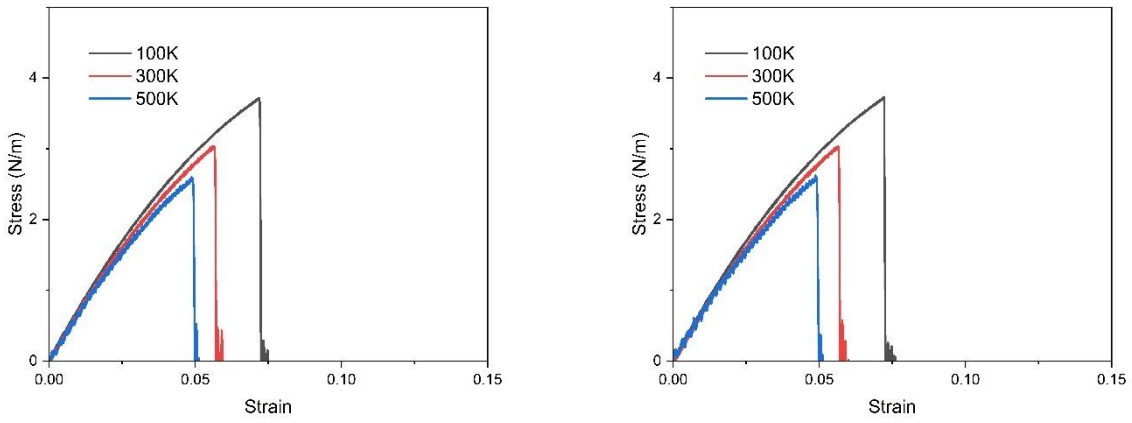

(a) (b)

Figure 41: The biaxial tensile stress–strain curves of 1T SLMoTe$_2$ with 4 Tellurium at different temperatures of 100,300 and 500 K in (a) armchair, and (b) zigzag directions.

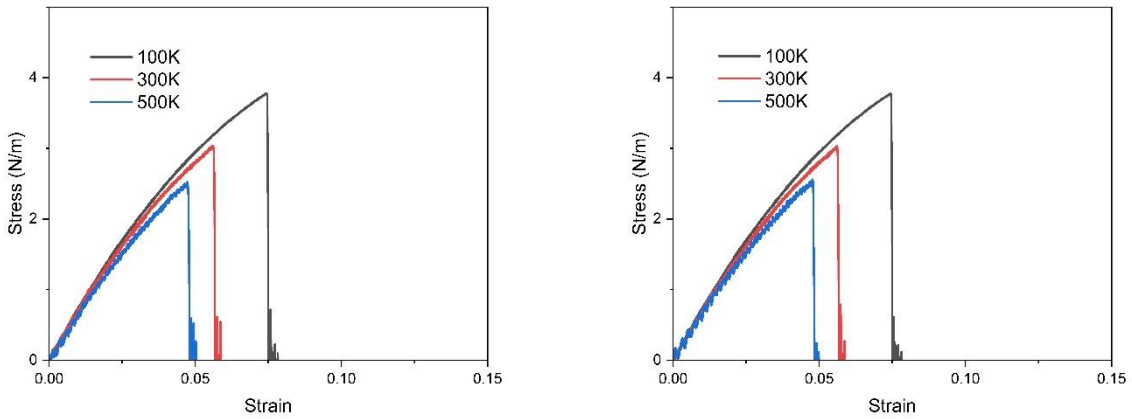

(a) (b)

Figure 42: The biaxial tensile stress–strain curves of 1T SLMoTe$_2$ with 1 Molybdenum and 6 Tellurium vacancy at different temperatures of 100,300 and 500 K in (a) armchair, and (b) zigzag directions.

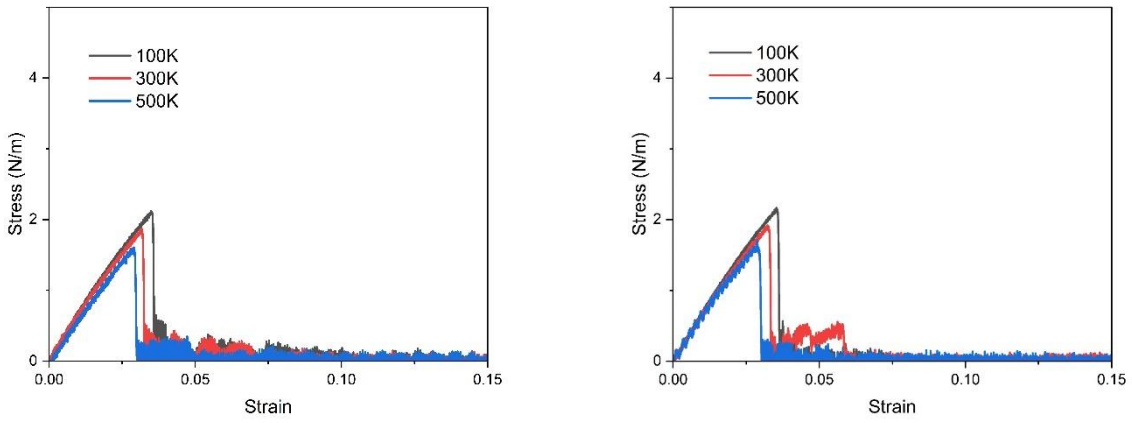

(a) (b)

Figure 43: The biaxial tensile stress–strain curves of 1T $SLMoTe_2$ with pre-crack in armchair direction at different temperatures of 100,300 and 500 K in (a) armchair, and (b) zigzag directions.

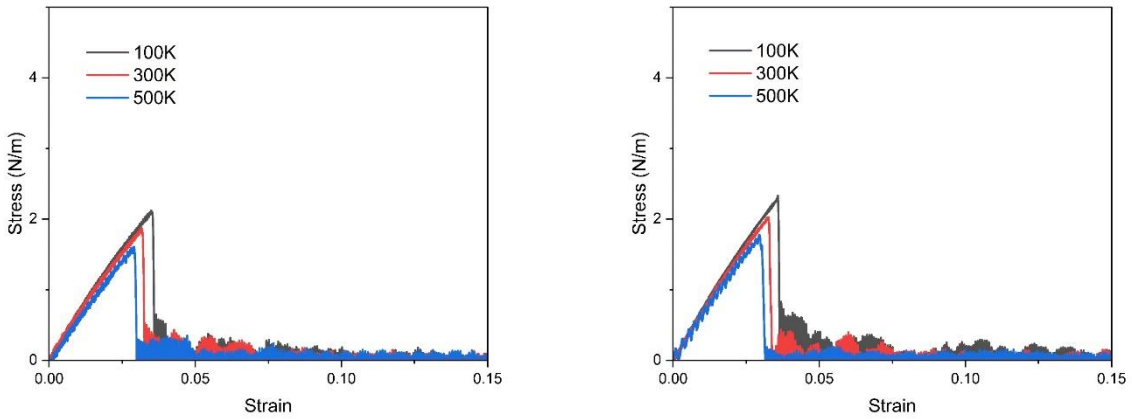

(a) (b)

Figure 44: The biaxial tensile stress–strain curves of 1T $SLMoTe_2$ pre-crack in zigzag direction at different temperatures of 100,300 and 500 K in (a) armchair, and (b) zigzag directions.

4.6. Variation in Strain Rate

Varying the strain rate in molecular dynamics (MD) simulations is done to evaluate the mechanical properties of 2D $MoTe_2$ because it allows us to study the material's response under different loading conditions. By applying different strain rates, we can investigate how the material behaves at different rates of deformation, which provides valuable insights into its mechanical behavior, such as its strength, ductility, and resistance to deformation. The variation in strain rate helps capture the dependence of material properties on the loading rate, providing a more comprehensive understanding of its mechanical response and allowing for the prediction of its behavior under different real-world conditions. We have used 2 strain rates 10e8 and 10e9 (see Figure 45-68) for our analysis.

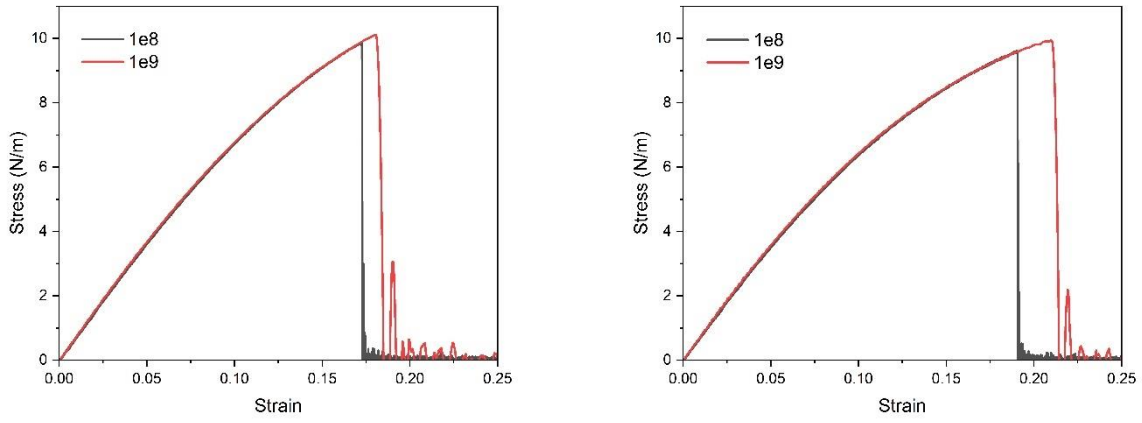

(a) (b)

Figure 45: The uniaxial tensile stress–strain curves of Pristine 2H SL$MoTe_2$ at 300K at strain rates 1e8 and 1e9 in (a) armchair, and (b) zigzag directions.

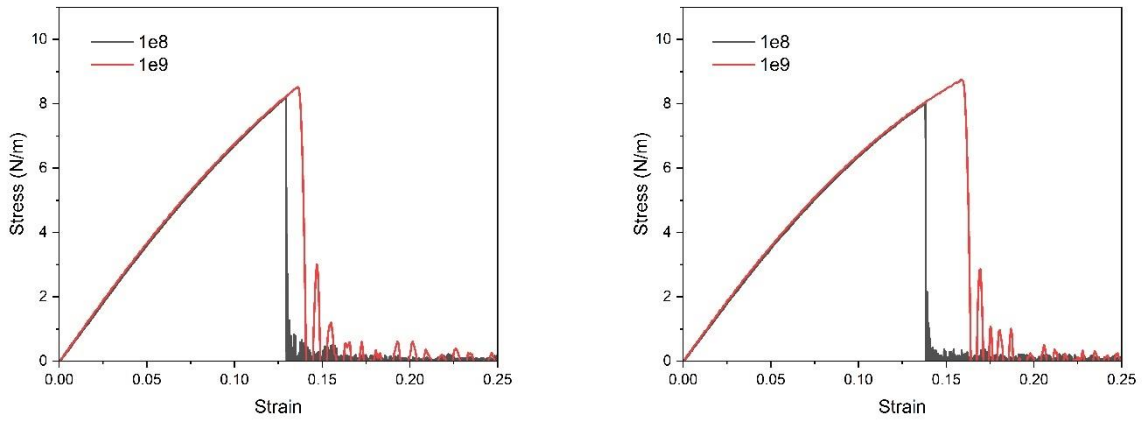

(a) (b)

Figure 46: The uniaxial tensile stress–strain curves of 2H SLMoTe$_2$ with 2 Tellurium vacancy at 300K at strain rates 1e8 and 1e9 in (a) armchair, and (b) zigzag directions.

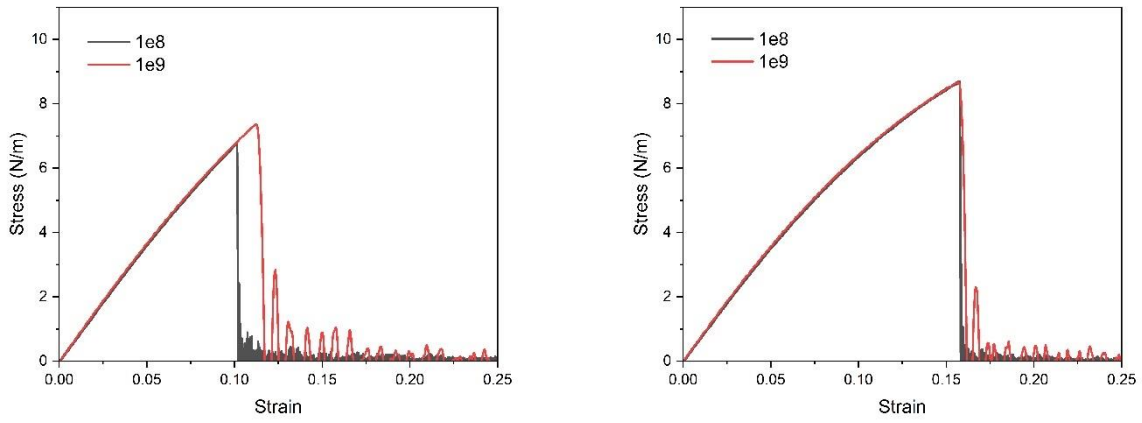

(a) (b)

Figure 47: The uniaxial tensile stress–strain curves of 2H SLMoTe$_2$ with 4 Tellurium vacancy at 300K at strain rates 1e8 and 1e9 in (a) armchair, and (b) zigzag directions.

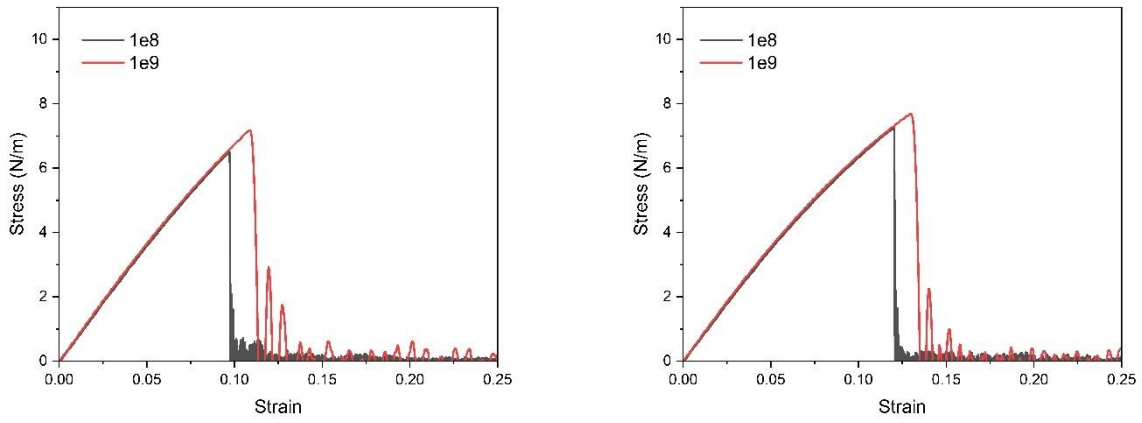

(a) (b)

Figure 48: The uniaxial tensile stress–strain curves of 2H $SLMoTe_2$ with 1 Molybdenum and 4 Tellurium vacancy at 300K at strain rates 1e8 and 1e9 in (a) armchair, and (b) zigzag directions.

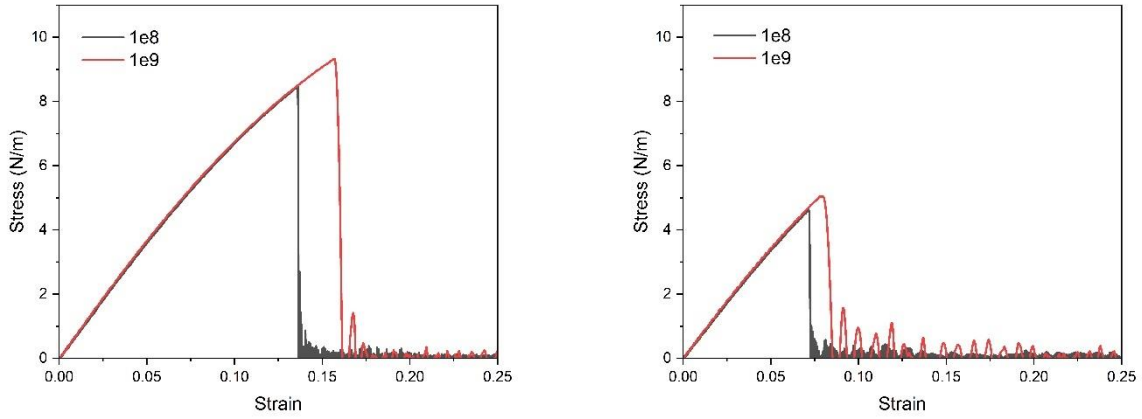

(a) (b)

Figure 49: The uniaxial tensile stress–strain curves of 2H $SLMoTe_2$ with line defect along armchair direction at 300K at strain rates 1e8 and 1e9 in (a) armchair, and (b) zigzag directions.

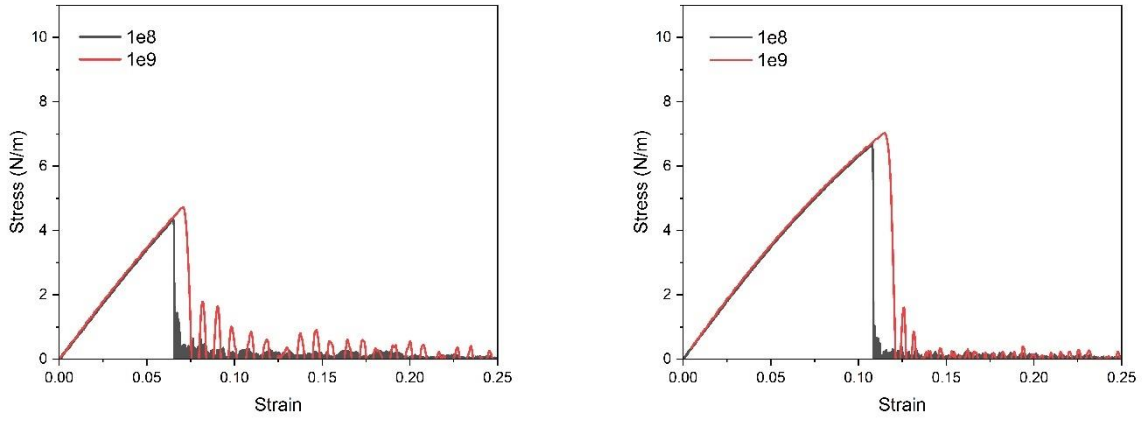

(a) (b)

Figure 50: The uniaxial tensile stress–strain curves of 2H SL$MoTe_2$ with line defect along zigzag direction at 300K at strain rates 1e8 and 1e9 in (a) armchair, and (b) zigzag directions.

To investigate the influence of strain rate on the mechanical behavior of 1T $MoTe_2$, we conducted LAMMPS simulations for uniaxial tensile tests in both the armchair and zigzag axes. By subjecting the material to varying strain rates of 1e8 and 1e9, we aimed to compare the resulting stress-strain behavior and understand how strain rate affects the material's mechanical response. The simulations were performed on the same 1T $MoTe_2$ structure under identical temperature conditions to ensure a consistent comparison. By collecting output data from the simulations, we generated stress-strain plots to visualize and analyze the material's response to different strain rates. These plots, presented in Figure 51 to 56, provide a comprehensive representation of the stress-strain behavior for both strain rates in the armchair and zigzag directions. By juxtaposing the stress-strain plots for the two strain rates, we were able to observe any discernible differences in the mechanical response of 1T $MoTe_2$. This comparative analysis allowed us to gain deeper insights into the material's mechanical properties, including its elastic deformation, plastic deformation, and ultimate failure stength, under varying strain rates.

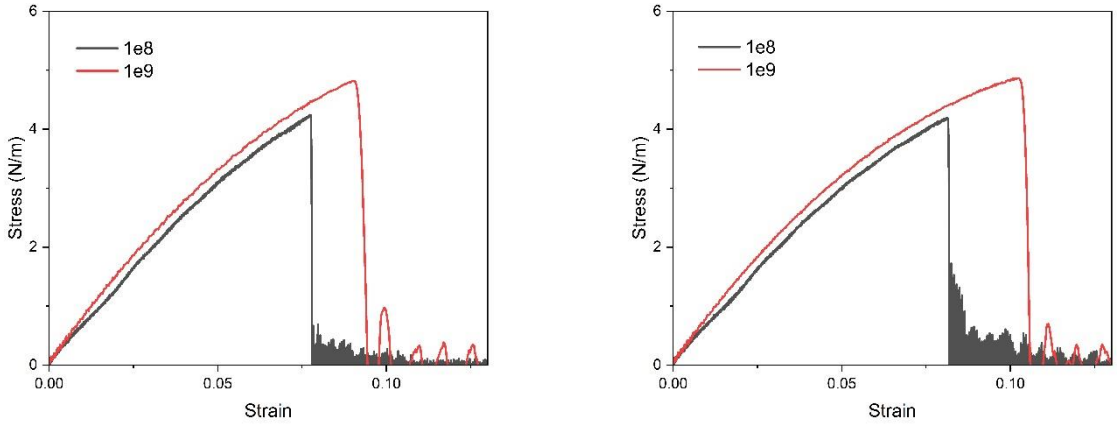

(a) (b)

Figure 51: The uniaxial tensile stress–strain curves of Pristine 1T $SLMoTe_2$ at 300K at strain rates 1e8 and 1e9 in (a) armchair, and (b) zigzag directions.

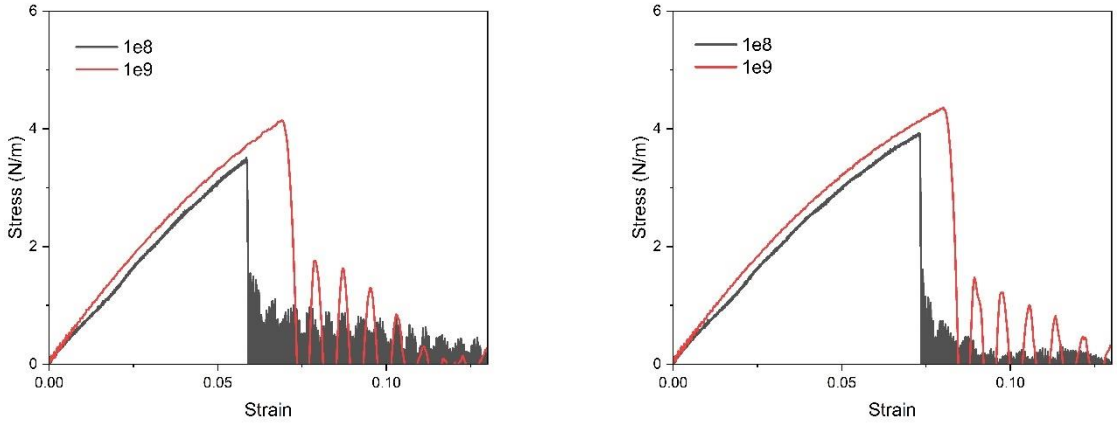

(a) (b)

Figure 52: The uniaxial tensile stress–strain curves of 1T $SLMoTe_2$ with 2 Tellurium vacancy at 300K at strain rates 1e8 and 1e9 in (a) armchair, and (b) zigzag directions.

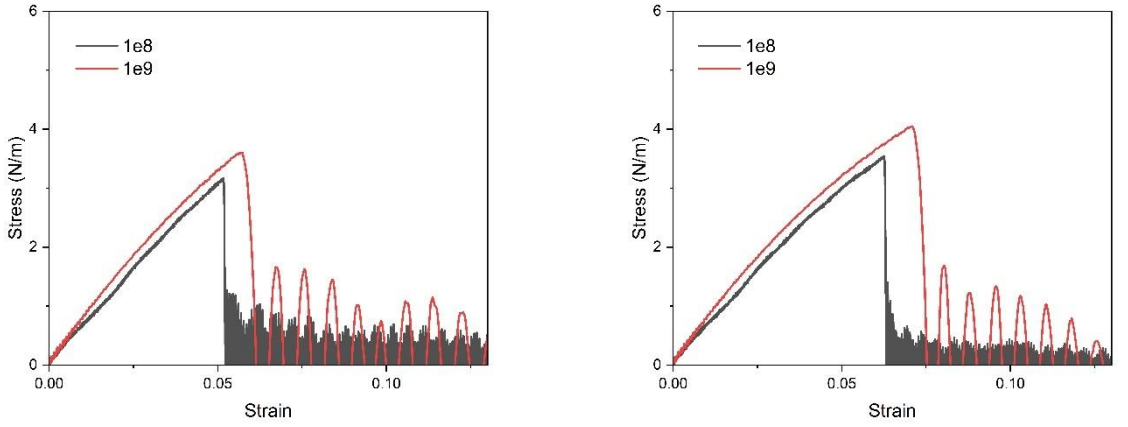

(a) (b)

Figure 53: The uniaxial tensile stress–strain curves of 1T $SLMoTe_2$ with 4 Tellurium vacancy at 300K at strain rates 1e8 and 1e9 in (a) armchair, and (b) zigzag directions.

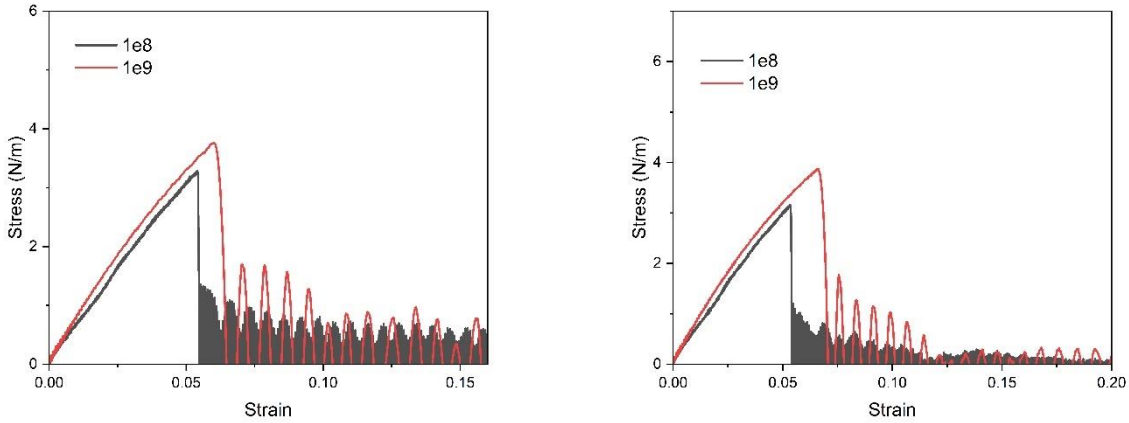

(a) (b)

Figure 54: The uniaxial tensile stress–strain curves of 1T $SLMoTe_2$ with 1 Molybdenum and 6 Tellurium vacancy at 300K at strain rates 1e8 and 1e9 in (a) armchair, and (b) zigzag directions.

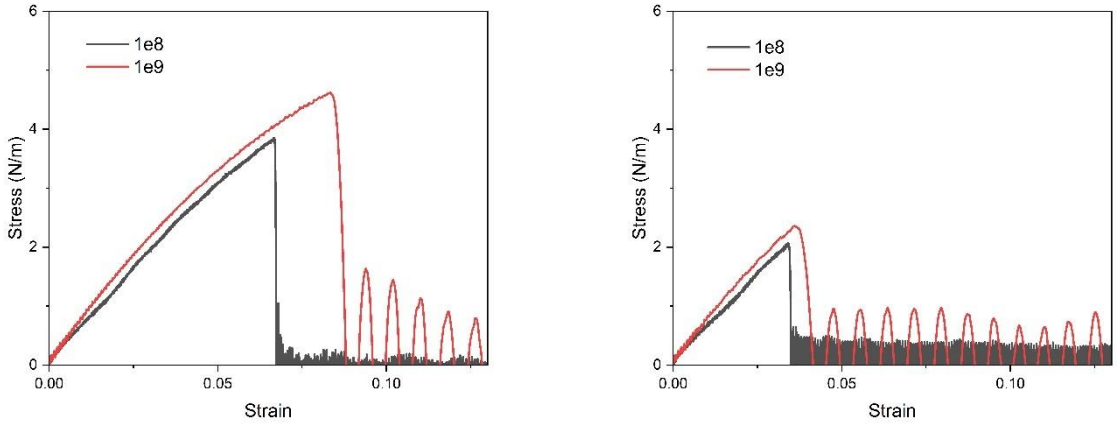

(a) (b)

Figure 55: The uniaxial tensile stress–strain curves of 1T SLMoTe$_2$ with line defect along armchair axis at 300K at strain rates 1e8 and 1e9 in (a) armchair, and (b) zigzag directions.

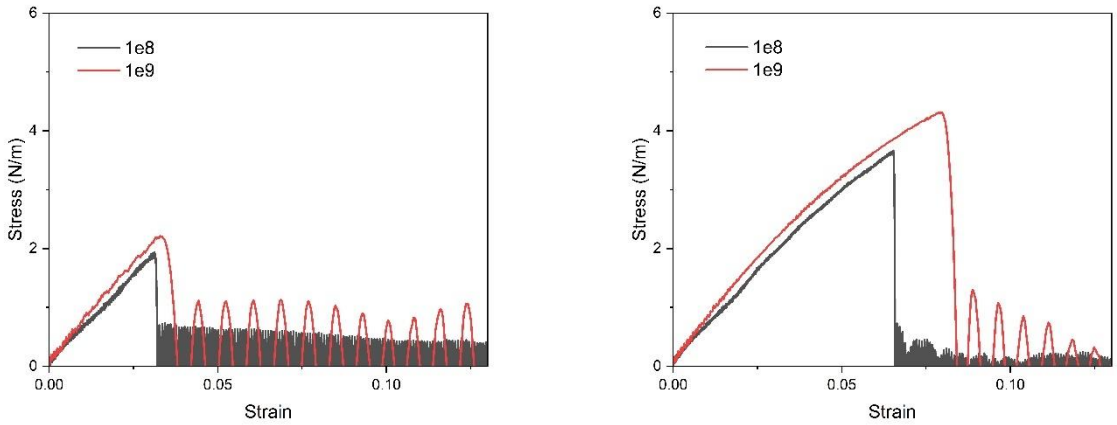

(a) (b)

Figure 56: The uniaxial tensile stress–strain curves of 1T SLMoTe$_2$ with line defect along zigzag axis at 300K at strain rates 1e8 and 1e9 in (a) armchair, and (b) zigzag directions.

Our findings revealed that varying the strain rate had a notable effect on the mechanical response of 2D MoTe$_2$. When the strain rate was increased from 1e8 to 1e9, significant changes were observed in the material's behavior. These changes encompassed various mechanical properties,

such as the ultimate stress, fracture strain, and Young's modulus. In particular, we observed that an increase in the strain rate resulted in alterations in the material's ultimate stress. The ultimate stress, which represents the maximum stress the material can endure before failure, exhibited different values at the two strain rates. Additionally, the fracture strain, which represents the strain at the point of failure, also showed variations with the strain rate.

Moreover, the Young's modulus, which characterizes the material's stiffness, was found to be affected by the strain rate. The modulus values differed between the two strain rates, indicating a change in the material's elastic response. Similar trend is observed in the biaxial tensile test stress strain response for both phases of $MoTe_2$ as shown in the Figure 57 to 68

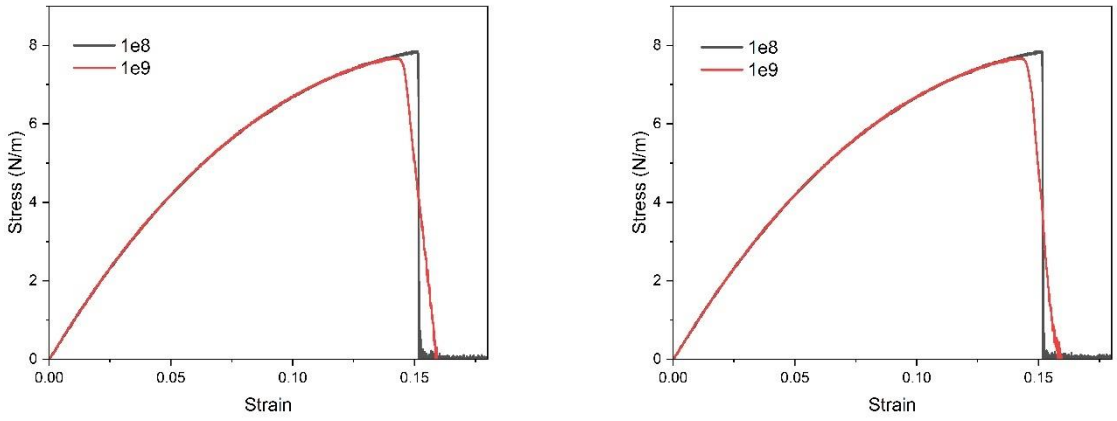

(a) (b)

Figure 57: The biaxial tensile stress–strain curves of Pristine 2H SL$MoTe_2$ at 300K at strain rates 1e8 and 1e9 in (a) armchair, and (b) zigzag directions.

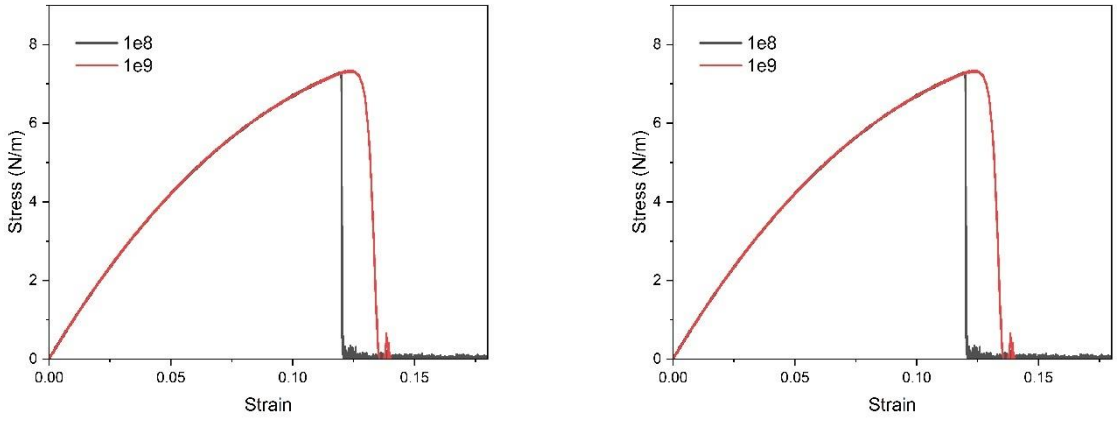

(a) (b)

Figure 58: The biaxial tensile stress–strain curves of 2H SLMoTe$_2$ with 2 Tellurium vacancy at 300K at strain rates 1e8 and 1e9 in (a) armchair, and (b) zigzag directions.

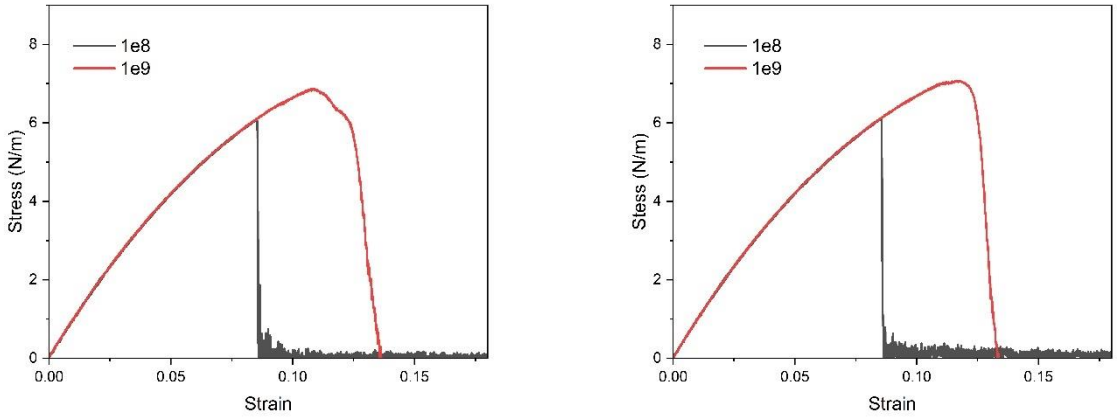

(a) (b)

Figure 59: The biaxial tensile stress–strain curves of 2H SLMoTe$_2$ with 4 Tellurium vacancy at 300K at strain rates 1e8 and 1e9 in (a) armchair, and (b) zigzag directions.

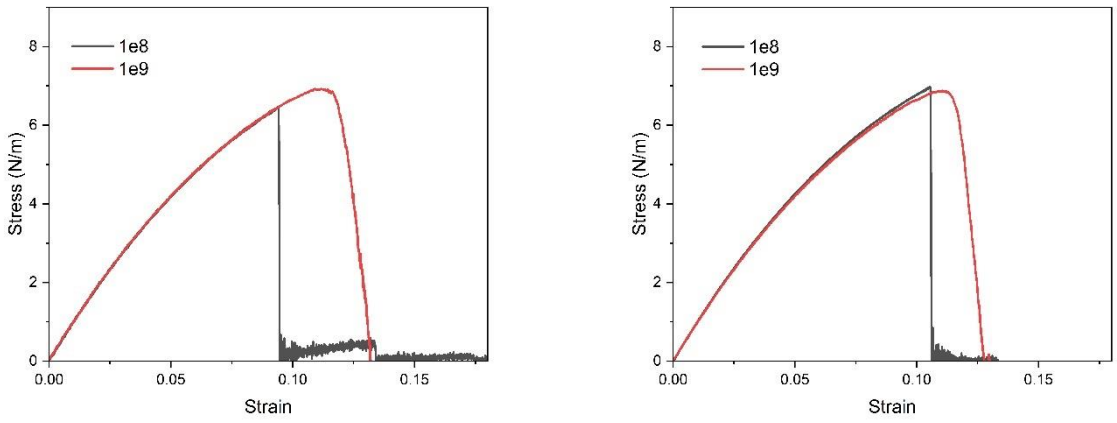

(a) (b)

Figure 60: The biaxial tensile stress–strain curves of 2H $SLMoTe_2$ with 1 Molybdenum and 6 Tellurium vacancy at 300K at strain rates 1e8 and 1e9 in (a) armchair, and (b) zigzag directions.

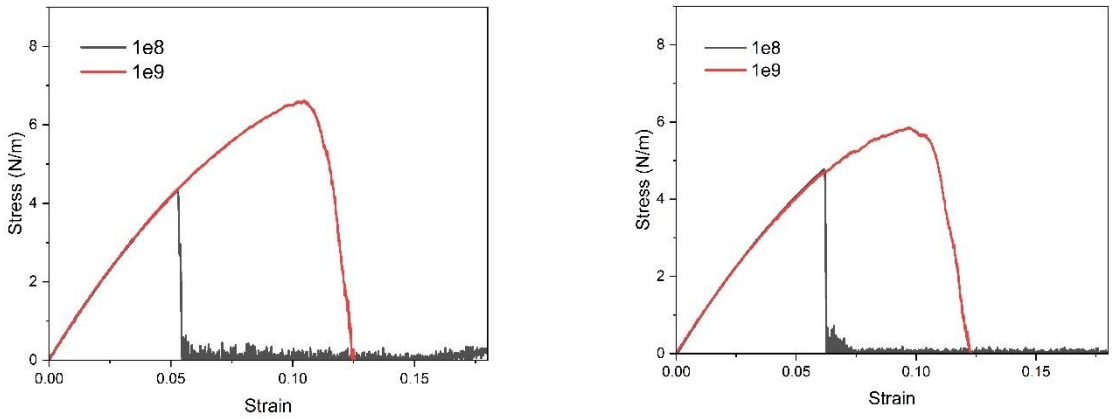

(a) (b)

Figure 61: The biaxial tensile stress–strain curves of 2H $SLMoTe_2$ with line defect along armchair axis at 300K at strain rates 1e8 and 1e9 in (a) armchair, and (b) zigzag directions.

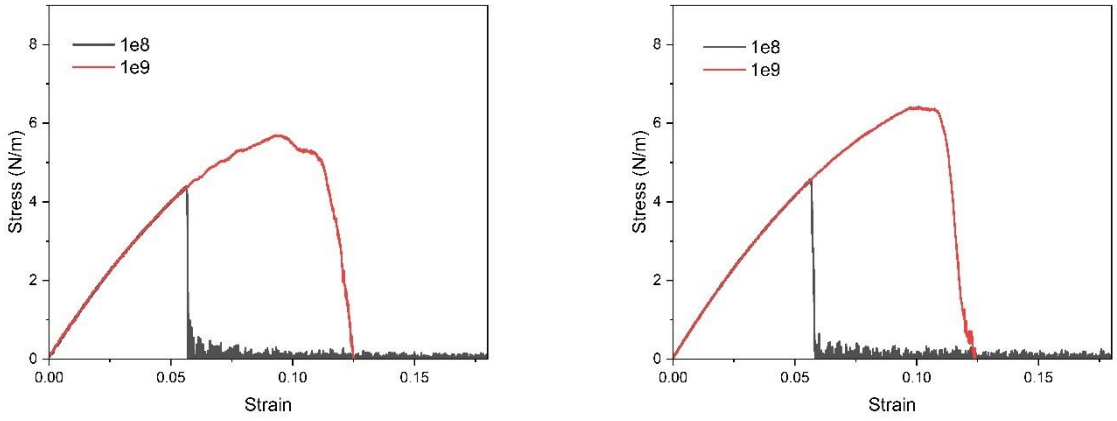

(a) (b)

Figure 62: The biaxial tensile stress–strain curves of 2H SLMoTe$_2$ with line defect along zigzag axis at 300K at strain rates 1e8 and 1e9 in (a) armchair, and (b) zigzag directions.

To investigate the influence of strain rate on the mechanical behavior of 1T MoTe$_2$, we conducted LAMMPS simulations for uniaxial tensile tests in both the armchair and zigzag directions. By subjecting the material to varying strain rates of 1e8 and 1e9, we aimed to compare the resulting stress-strain behavior and understand how strain rate affects the material's mechanical response. The simulations were performed on the same 1T MoTe$_2$ structure under identical temperature conditions to ensure a consistent comparison. By collecting output data from the simulations, we generated stress-strain plots to visualize and analyze the material's response to different strain rates. These plots, presented in Figure 63 to 68, provide a comprehensive representation of the stress-strain behavior for both strain rates in the armchair and zigzag directions. By juxtaposing the stress-strain plots for the two strain rates, we were able to observe any discernible differences in the mechanical response of 1T MoTe$_2$. This comparative analysis allowed us to gain deeper insights into the material's mechanical properties, including its elastic deformation, plastic deformation, and ultimate failure strength, under varying strain rates.

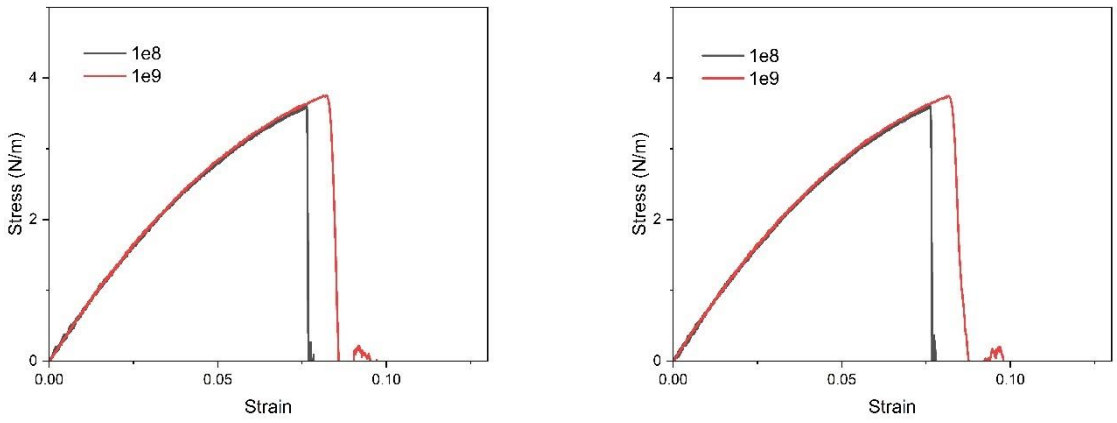

(a) (b)

Figure 63: The biaxial tensile stress–strain curves of Pristine 1T SLMoTe$_2$ at 300K at strain rates 1e8 and 1e9 in (a) armchair, and (b) zigzag directions.

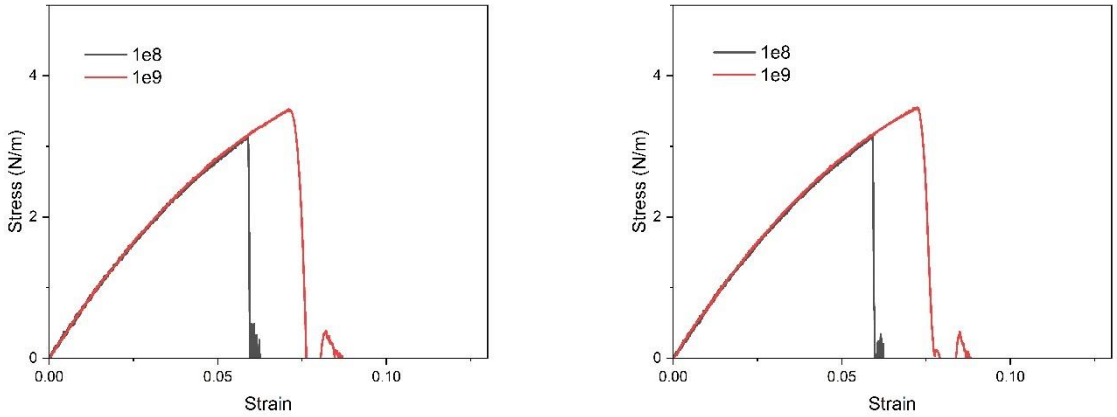

(a) (b)

Figure 64: The biaxial tensile stress–strain curves of 1T SLMoTe$_2$ with 2 Tellurium vacancy at 300K at strain rates 1e8 and 1e9 in (a) armchair, and (b) zigzag directions.

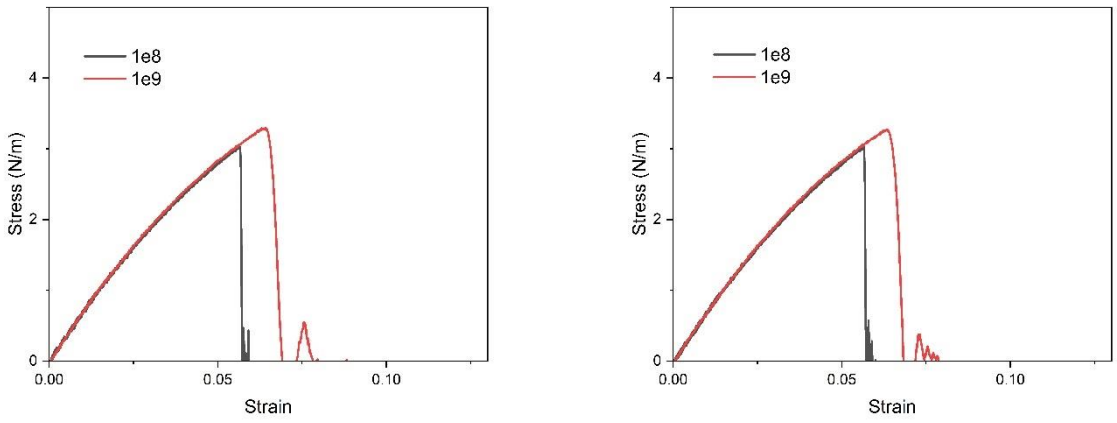

(a) (b)

Figure 65: The biaxial tensile stress–strain curves of 1T SLMoTe$_2$ with 4 Tellurium vacancy at 300K at strain rates 1e8 and 1e9 in (a) armchair, and (b) zigzag directions.

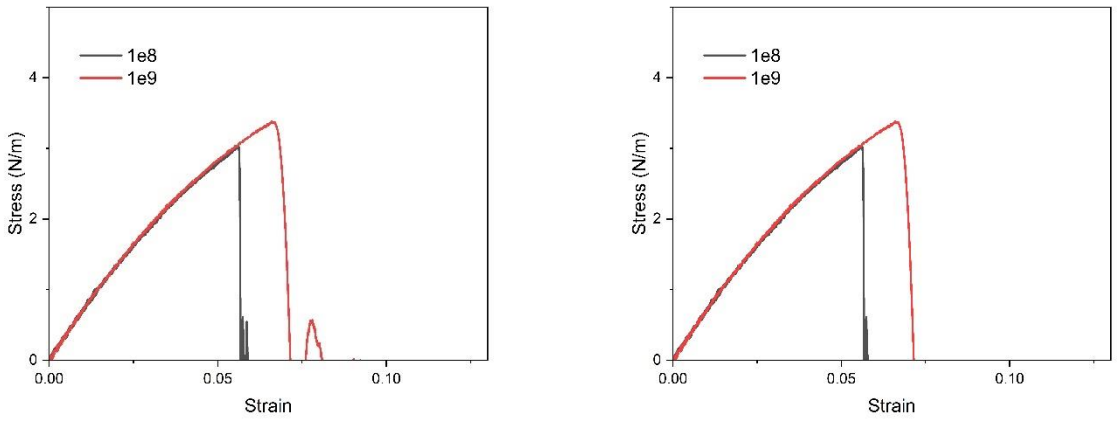

(a) (b)

Figure 66: The biaxial tensile stress–strain curves of 1T SLMoTe$_2$ with 1 Molybdenum and 6 Tellurium vacancy at 300K at strain rates 1e8 and 1e9 in (a) armchair, and (b) zigzag directions.

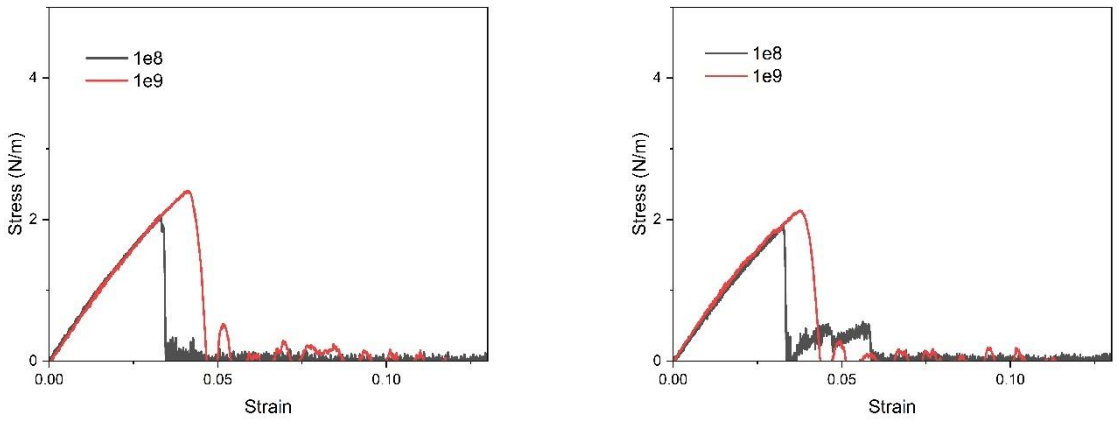

(a) (b)

Figure 67: The biaxial tensile stress–strain curves of 1T SLMoTe$_2$ with line defect along armchair axis at 300K at strain rates 1e8 and 1e9 in (a) armchair, and (b) zigzag directions.

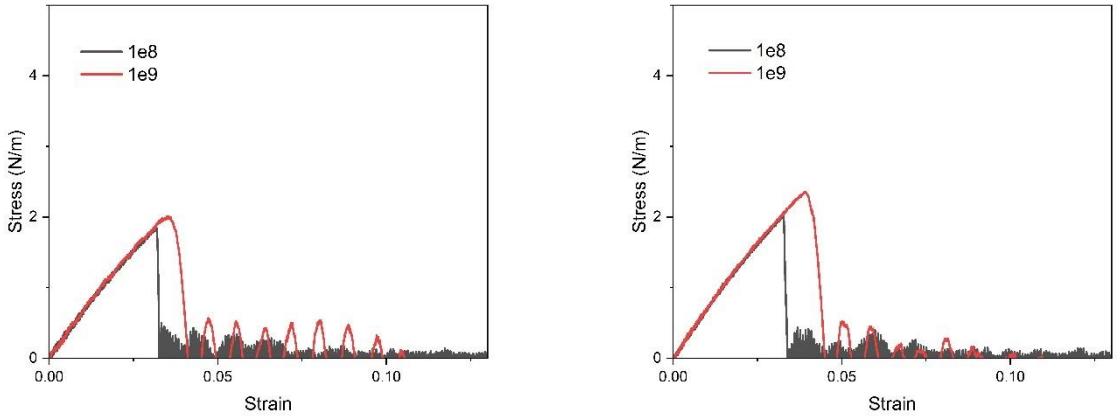

(a) (b)

Figure 68: The biaxial tensile stress–strain curves of 1T SLMoTe$_2$ with line defect along zigzag axis at 300K at strain rates 1e8 and 1e9 in (a) armchair, and (b) zigzag directions.

In the uniaxial tensile tests, a notable change in the mechanical behavior of both 2H-MoTe$_2$ and 1T-MoTe$_2$ was observed when the strain rate was increased from 1e8 to 1e9.. Specifically, higher strain rates led to increased ultimate stress values for both phases. This indicates that the materials

exhibited enhanced strength when subjected to higher strain rates. It is observed that the fracture strain values decreased with increasing strain rate. This suggests that higher strain rates resulted in a reduced ability of the materials to withstand deformation before fracture occurred. It indicates a decreased ductility and increased brittleness at higher strain rates for both 2H-$MoTe_2$ and 1T-$MoTe_2$.

In the biaxial tensile tests, similar trends were observed. Increasing the strain rate from 1e8 to 1e9 led to an increase in the ultimate stress values for both 2H-$MoTe_2$ and 1T-$MoTe_2$. Additionally, the fracture strain values decreased with higher strain rates, indicating reduced ductility and increased brittleness under increased loading rates. These findings highlight the significant influence of strain rate on the mechanical behavior of both $MoTe_2$ phases. The observed trends suggest that the response of these materials to external loading is sensitive to the applied strain rate. It is important to consider the strain rate effects when evaluating the mechanical properties of these materials, as they can have implications for their performance in practical applications.

4.5. Fracture Visualization and Stress Mapping

Uniaxial and biaxial tensile tests were conducted on 2H and 1T $MoTe_2$ using LAMMPS, and stress mapping was performed to study the deformation characteristics of the materials. The stress mapping analysis allowed for the visualization of the stress distribution in the materials under different loading conditions. In uniaxial tensile tests, stress was selectively exerted along one direction, while in biaxial tensile tests, stress was simultaneously applied along two directions. The visualization (see Figure 69-73) was done from the LAMMPS output dump file with the help of 3rd party software OVITO as. Rainbow color coding was applied to indicate stress concentration regions. In Figures 69-71 strain rate used was 1e9 whereas in Figure 72 shows biaxial tensile tests that were done at 1e8 strain rate.

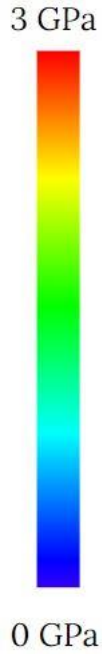

Figure 69:The color coding scale used for indicating stress concentration

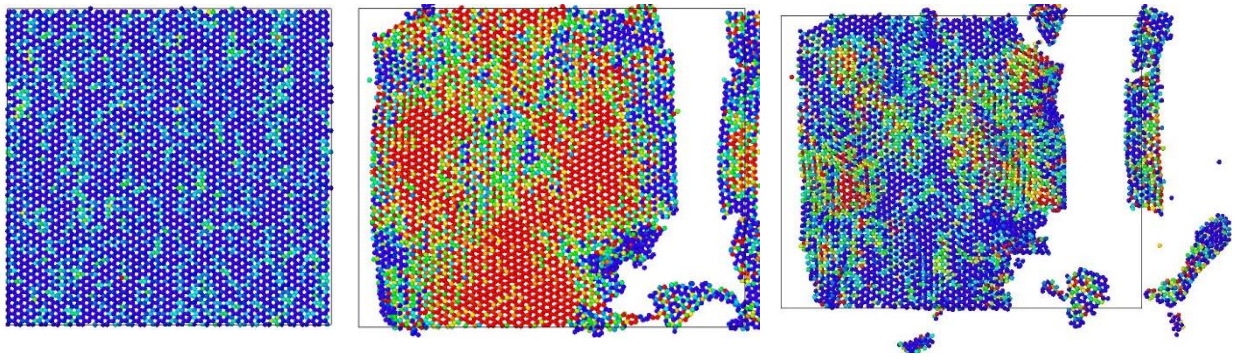

0.00% 19.31% 20.44%

(I)

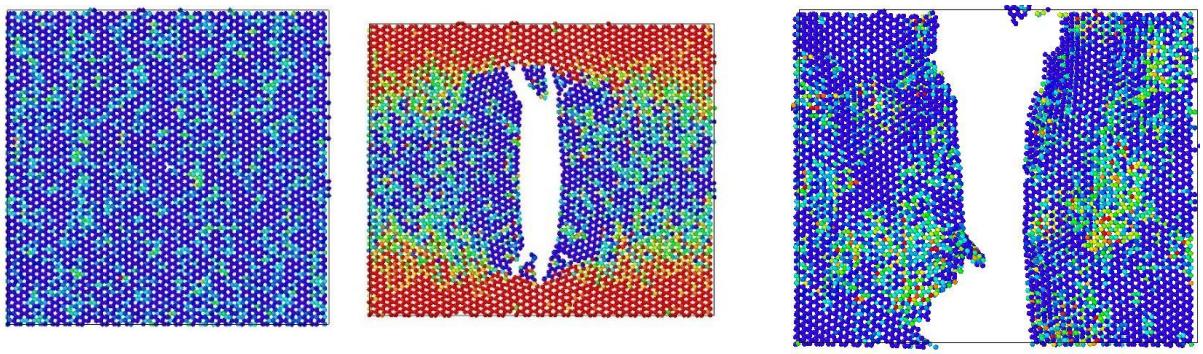

0.00% 14.02% 17.04%

(II)

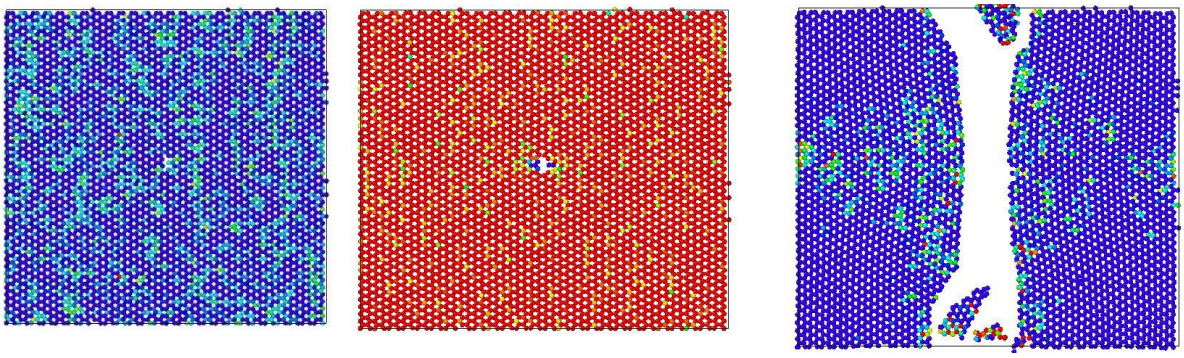

0.00% 11.01% 12.03%

(III)

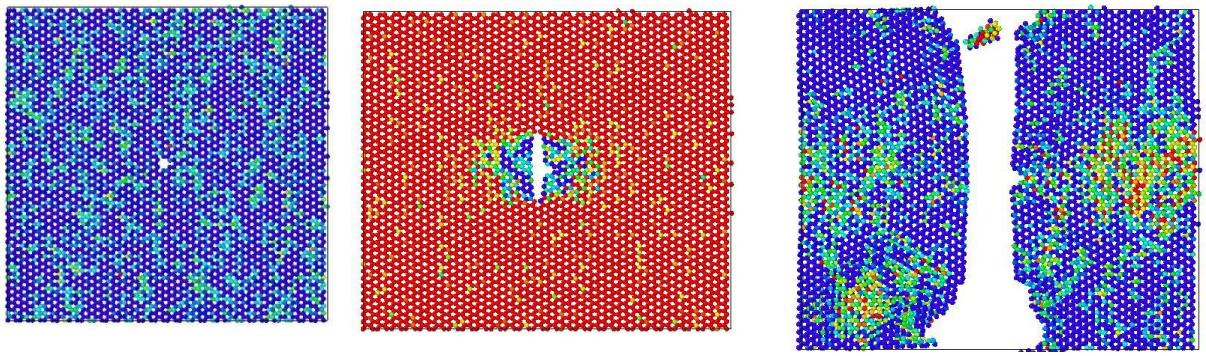

0.00% 11.02% 13.00%

(IV)

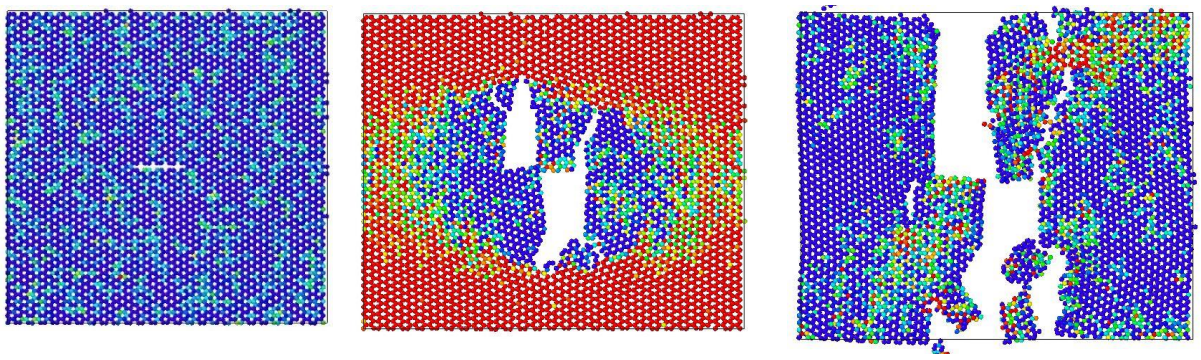

0.00% 16.00% 17.03%

(V)

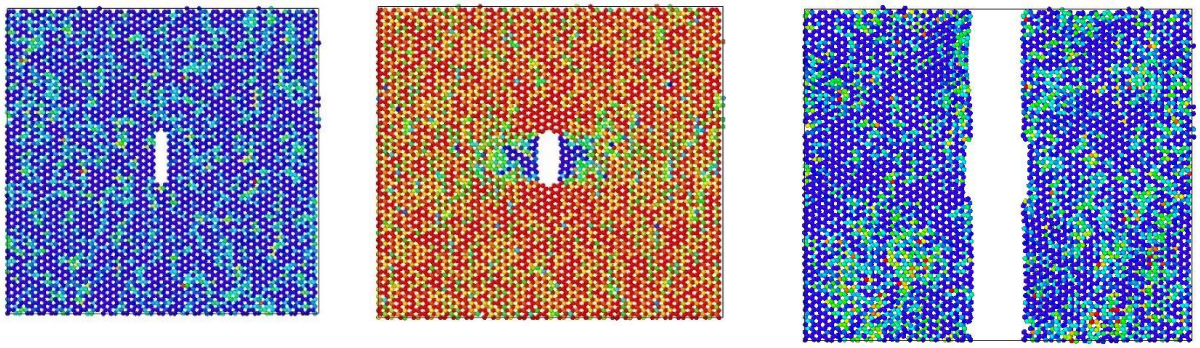

0.00% 7.01% 14.05%

(VI)

Figure 70: Fracture snapshots of 2H SL$MoTe_2$ with and without defect - (I) Pristine structure (II) with 2 Tellurium vacancy (III) with 4 Tellurium vacancy (IV) with 1 Molybdenum 6 Tellurium Vacancy (V) with line defect along armchair direction and (VI) with line defect along zigzag direction, observed under uniaxial tension applied along the armchair direction. Under each snapshot, corresponding strain is mentioned in percentage.

The stress mapping of 2H $MoTe_2$ (Figure 70) revealed interesting patterns and trends in the material's response to uniaxial tensile loading. We observed that the stress was primarily concentrated at the edges and corners of the specimen, indicating the presence of stress concentration zones. These regions experienced higher levels of stress compared to the rest of the material.

Furthermore, as the applied strain increased, the stress distribution underwent changes. The stress concentration zones became more prominent and extended along the edges, highlighting the vulnerability of these areas to higher stress levels and potential failure.

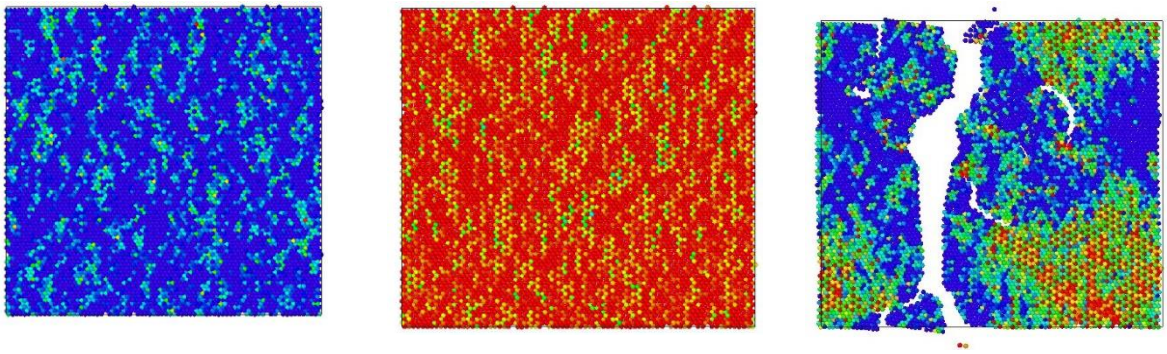

0.00% 9.02% 10.01%

(I)

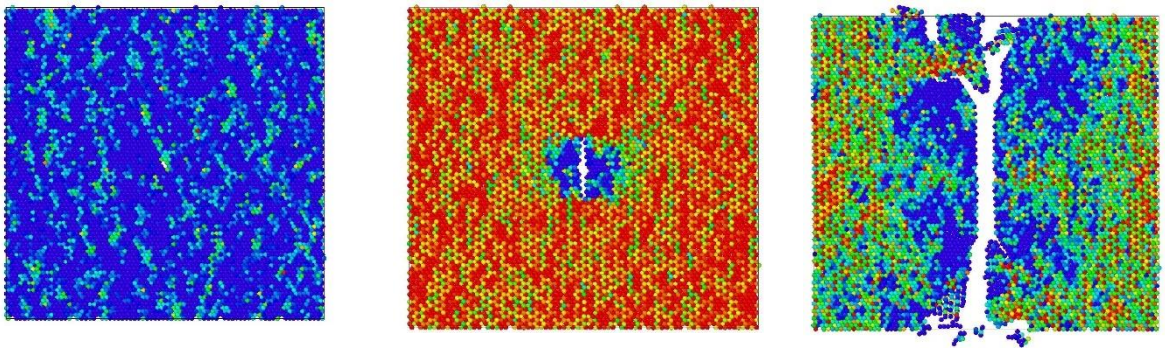

0.00% 7.01% 8.00%

(II)

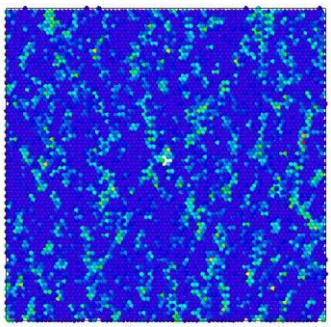

0.00%

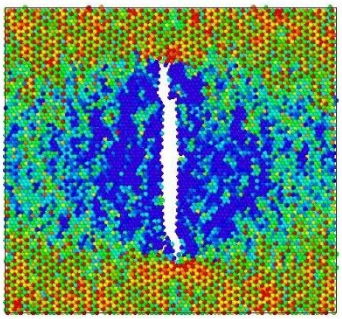

6.04%

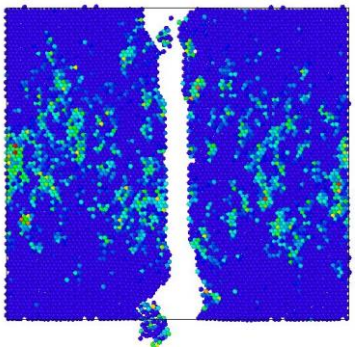

7.00%

(III)

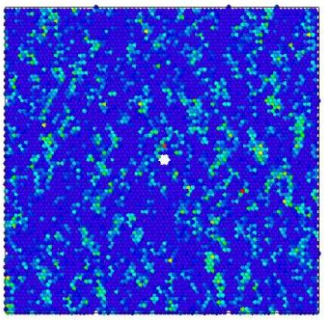

0.00%

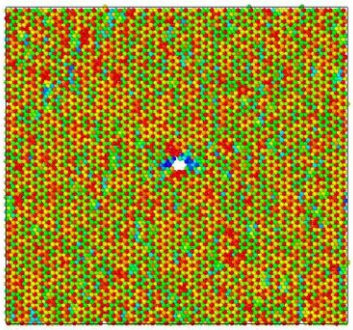

6.03%

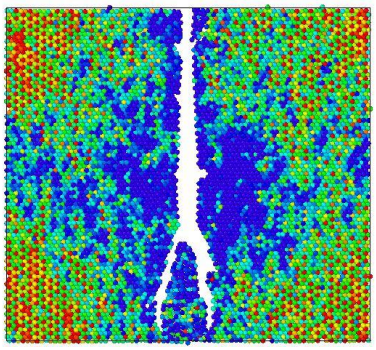

7.09%

(IV)

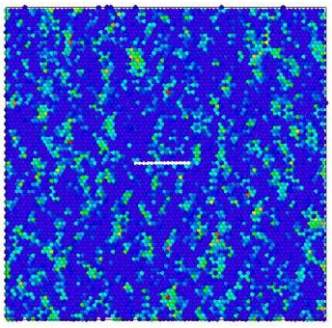

0.00%

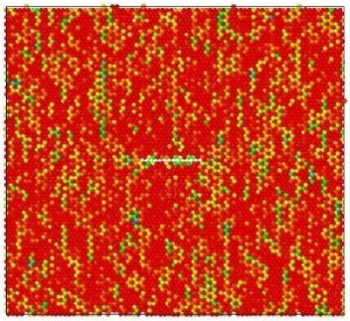

8.02%

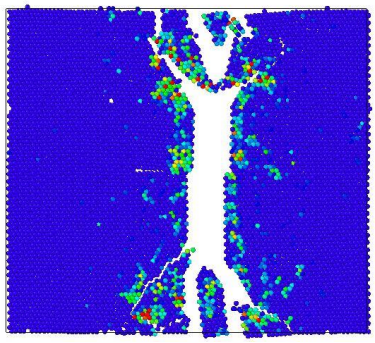

9.05%

(V)

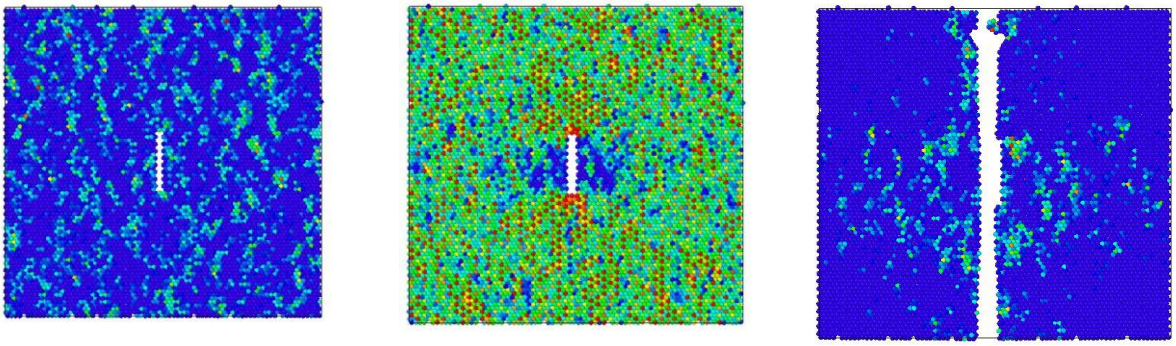

0.00% 3.02% 4.05%

(VI)

Figure 71: Fracture snapshots of 1T SL$MoTe_2$ with and without defect - (I) Pristine structure (II) with 2 Tellurium vacancy (III) with 4 Tellurium vacancy (IV) with 1 Molybdenum 6 Tellurium Vacancy (V) with line defect along armchair direction and (VI) line defect along zigzag direction

The stress mapping analysis of 1T $MoTe_2$ (Figure 71) revealed distinct characteristics that differentiate it from the stress distribution observed in the 2H phase. Unlike the 2H phase, the stress concentration zones in 1T $MoTe_2$ were found to be more evenly distributed throughout the specimen, rather than being primarily concentrated at the edges and corners. During uniaxial tensile loading, we observed that the stress was more uniformly distributed across the 1T $MoTe_2$ specimen. This suggests a more homogeneous stress distribution pattern, indicating a potentially higher resistance to stress concentration and localized failure.

Additionally, the stress mapping analysis showed that the stress concentration zones in 1T $MoTe_2$ were less pronounced compared to the 2H phase. This could be attributed to the structural differences between the two phases, as the 1T phase possesses a different atomic arrangement and bonding characteristics. The differences in stress mapping characteristics between the 1T and 2H phases of $MoTe_2$ highlight the influence of crystal structure on the mechanical behavior of the material. Understanding these distinctions is essential for tailoring the mechanical properties of $MoTe_2$ in specific applications, where the choice between the 1T and 2H phases can have a significant impact on the material's performance.

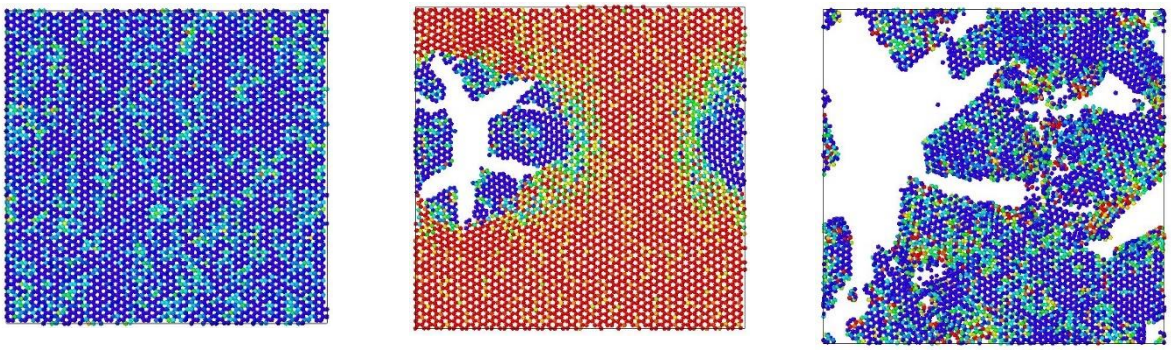

0.00% 15.16% 16.00%

(I)

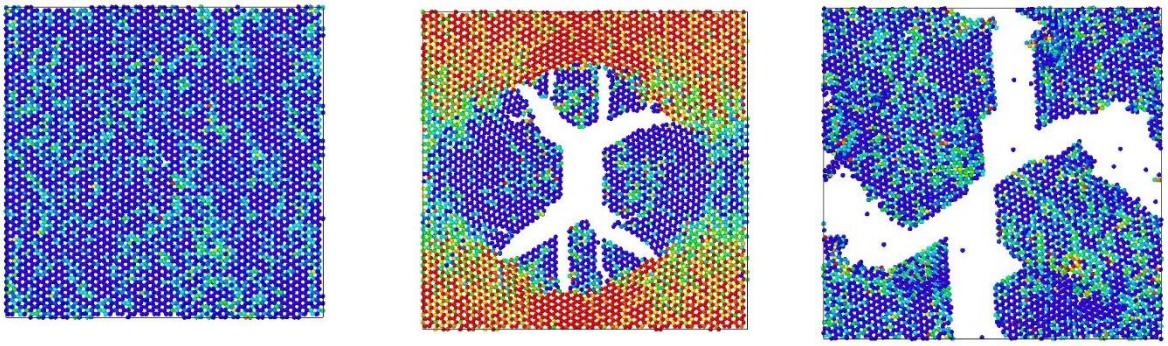

0.00% 12.04% 13.02%

(II)

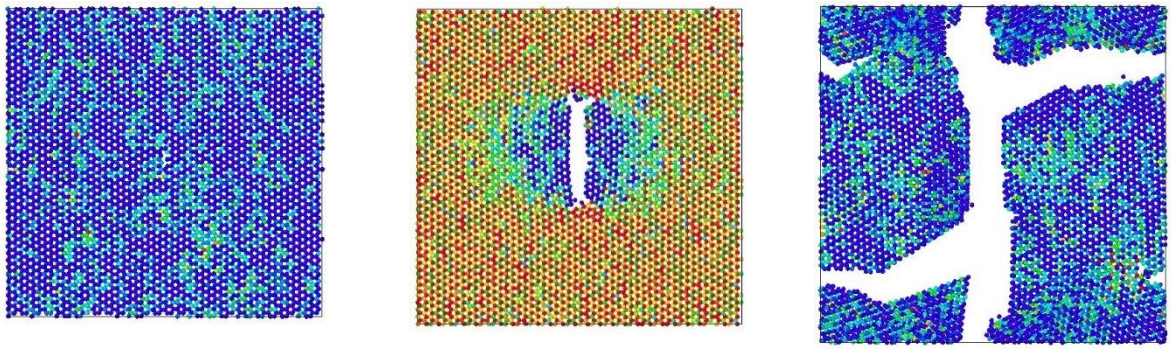

0.00% 8.55% 9.50%

(III)

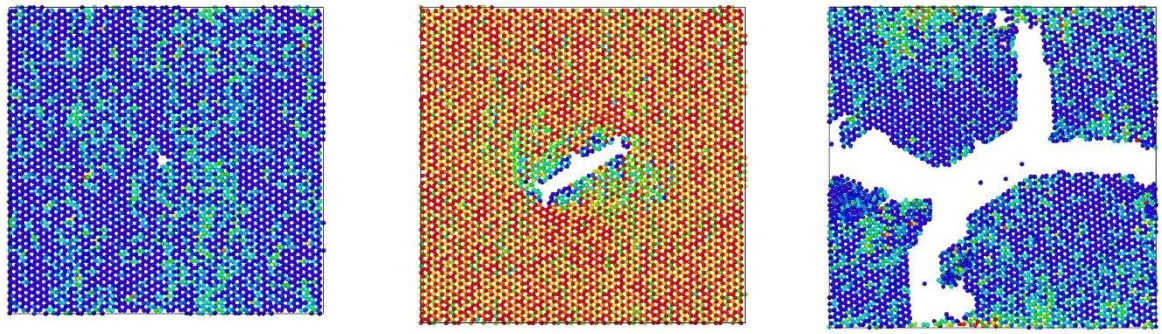

0.00% 9.42% 10.89%

(IV)

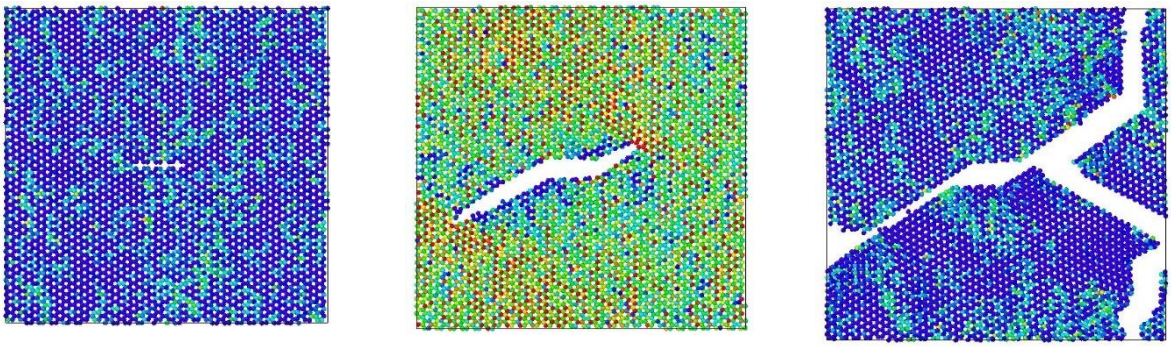

0.00% 5.31% 6.04%

(V)

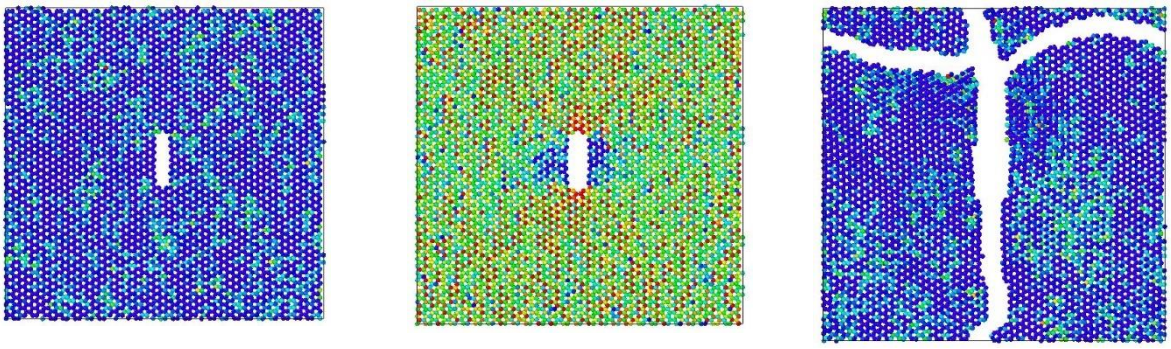

0.00% 5.61% 6.03%

(VI)

Figure 72: Fracture snapshots of 2H SLMoTe$_2$ with and without defect - (I) Pristine structure (II) with 2 Tellurium vacancy (III) with 4 Tellurium vacancy (IV) with 1 Molybdenum 6 Tellurium Vacancy (V) with line defect along armchair direction and (VI) line defect along zigzag direction.

Distinct patterns of stress distribution were observed in $MoTe_2$ during the biaxial tensile test (see Figure 72). The stress mapping analysis revealed that the edges and corners of the specimen exhibited prominent stress concentration zones with higher stress levels compared to the rest of the material. The analysis further indicated that the stress distribution was non-uniform throughout the specimen, displaying an anisotropic behavior. This anisotropy in stress distribution stemmed from the crystal structure and symmetry of $MoTe_2$, resulting in varying stress levels along different directions within the material.

Furthermore, the stress mapping analysis provided valuable insights into the propagation of stress within the material during biaxial tensile loading. It was observed that stress transmission and distribution predominantly occurred along the principal directions of the material, leading to preferential stress concentration and deformation patterns.

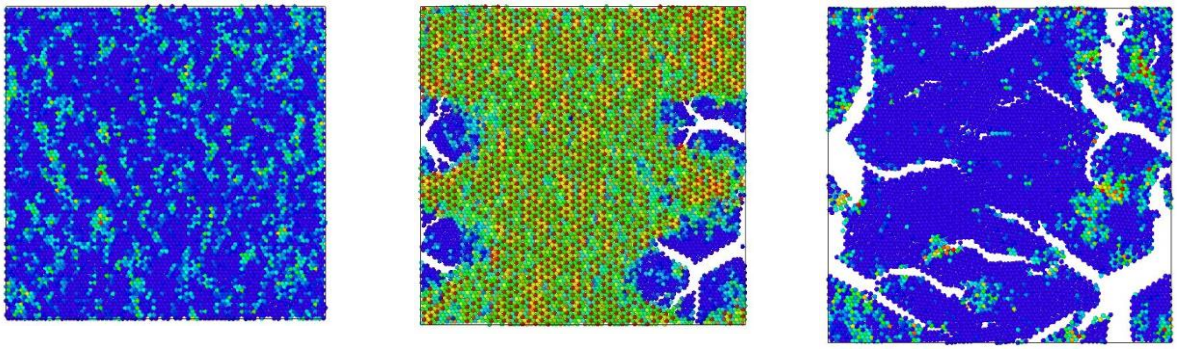

0.00% 8.30% 8.60%

(I)

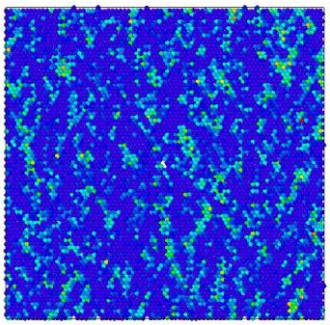

0.00%

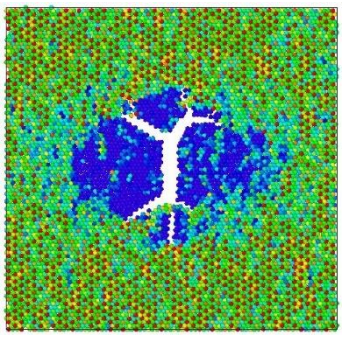

7.30%

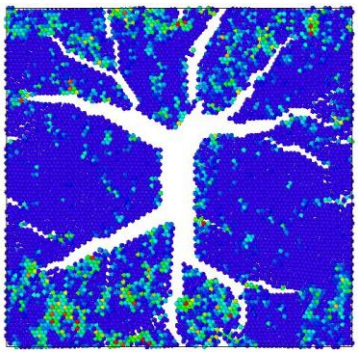

7.60%

(II)

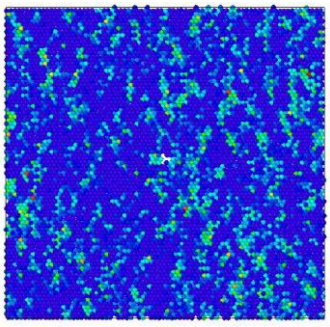

0.00%

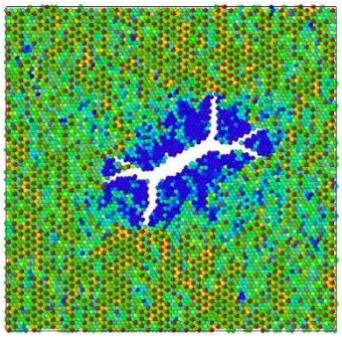

6.53%

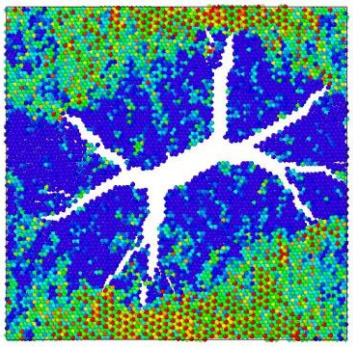

6.72%

(III)

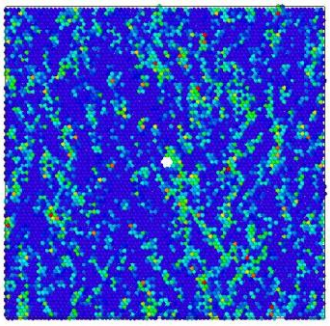

0.00%

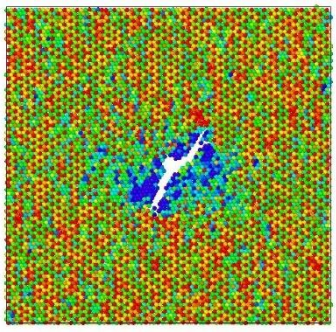

6.77%

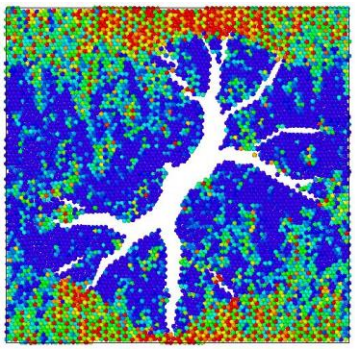

7.02%

(IV)

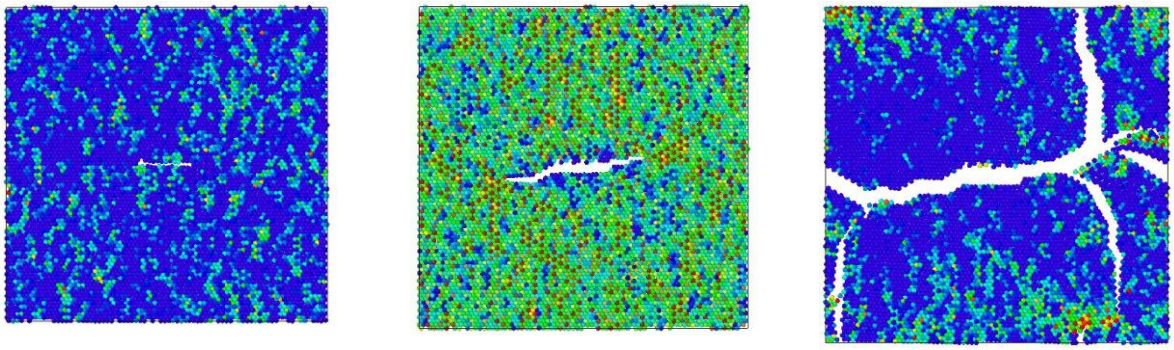

0.00% 3.92% 4.61%

(V)

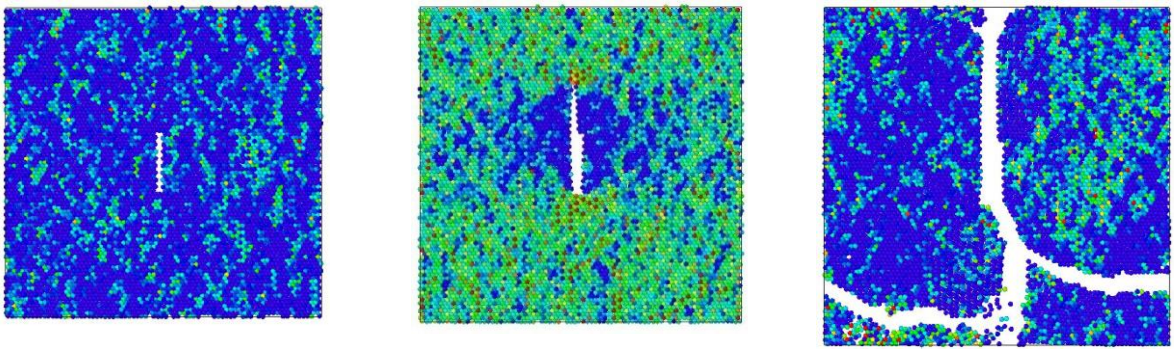

0.00% 3.61% 5.60%

(VI)

Figure 73: Fracture snapshots of 1T SL$MoTe_2$ with and without defect - (I) Pristine structure (II) with 2 Tellurium vacancy (III) with 4 Tellurium vacancy (IV) with 1 Molybdenum 6 Tellurium Vacancy (V) with line defect along armchair direction and (VI) with line defect along zigzag direction, observed under biaxial tension applied along both armchair and zigzag direction. Below each snapshot, corresponding strain is mentioned in percentage.

Mapping the stress distribution in 2H and 1T $MoTe_2$ (Figure 69 to 73) during uniaxial and biaxial tensile tests using LAMMPS software is crucial for gaining insights into the spatial variations of stress and strain within the material during the test. Analyzing this data can offer valuable understanding of the mechanical characteristics of the material, including its tensile strength, ductility, brittleness and fracture behavior. By analyzing stress and strain distribution, it is possible to identify regions where stress is concentrated and where failure is likely to occur, as well as to understand how defects and other factors affect the material's response to deformation. This

information is crucial for developing accurate models of material behavior and designing materials with optimized properties for specific applications.

Our findings revealed that in the uniaxial tensile test along the armchair axis, 2H-$MoTe_2$ exhibited a fracture behavior characterized by the formation of two distinct $MoTe_2$ fragments, indicating cleavage along the armchair direction. Conversely, 1T-$MoTe_2$ displayed a brittle lattice structure, without well-defined fragments, in the armchair axis. Shifting our focus to the zigzag direction in the uniaxial tensile test, a similar brittle trend is identified in the fracture behavior of 2H-MoTe2, although with potential variations in the specific fracture pattern. In contrast, the brittle fracture behavior observed in the armchair direction for 1T-$MoTe_2$ was not consistently observed when the tensile test was conducted along the zigzag axis, indicating a dependence of fracture behavior on the loading direction.

Furthermore, The fracture behavior in biaxial tensile tests was explored along both the armchair and zigzag axes. The stress-strain curves of both 2H and 1T $MoTe_2$ exhibited a non-linear elastic region leading up to the ultimate strength value. Beyond a critical fracture strain, a stress-free region emerged, indicating the rupture of the membranes. Notably, the fracture behavior varied between the 2H and 1T phases, underscoring the influence of crystal structure on fracture behavior under different loading conditions. Our findings yield insightful understanding into the fracture dynamics of 2D $MoTe_2$, highlighting the impact of phase and loading direction on their mechanical behavior. These observations emphasize the anisotropic nature of $MoTe_2$ and its mechanical response's dependency on crystal structure and loading conditions.

4.6. Limitations

1. Computational power: Molecular dynamics simulations of 2D materials like $MoTe_2$ require significant computational power, particularly in cases involving a substantial quantity of atoms. This limitation can restrict the simulation size and duration, which may affect the accuracy of the results obtained.

2. Experimental step: Another limitation is the lack of experimental data on 2D materials, which makes it difficult to validate simulation results. The experimental data can be used to calibrate the model parameters and to confirm the accuracy of the simulation.

3. Assumptions of standard conditions: Most simulations of 2D materials are carried out under idealized standard conditions, which may not reflect the real-world conditions. This limitation can affect the predictive ability of the simulation results.

4. Inherited computational error: The process of MD simulations entails numerically integrating the equations of motion., which can introduce errors in the results. The accumulation of such errors over time can lead to inaccurate results.

5. Approximation in governing equations: The reliability of the simulation results is also contingent on the accuracy of the governing equations used. The approximations and simplifications made in these equations can lead to errors in the results.

6. Random initial conditions: The initial conditions of the simulation, such as initial velocity, relaxation, and energy minimization, can affect the simulation results significantly. Therefore, careful selection of these initial conditions is necessary to ensure accurate results.

7. Time-scale limitation: MD simulations have a constraint in terms of the time-span that can be effectively simulated. Many important phenomena, such as plastic deformation and crack propagation, occur on time-scales that are much longer than what can be simulated using molecular dynamics.

8. Interatomic potentials: The accuracy of the simulation results is highly dependent on the interatomic potentials used to describe the atomic interactions. Different interatomic potentials can produce significantly different results, and the selection of an appropriate potential can be challenging.

9. Size limitation: The dimensions of the simulation cell is also a limitation, as This factor has the potential to impact the fidelity of the results. Small simulation cells can lead to boundary effects, while large cells can require significant computational resources.

10. Temperature limitation: Molecular dynamics simulations at high temperature require careful consideration of temperature control to ensure accurate results. Managing temperature in 2D materials is a demanding task due to their significant surface area and limited thermal conductivity.

4.7. Discussion on Findings

Our MD simulations yield valuable insights into the mechanical response of 2H and 1T $MoTe_2$ during uniaxial and biaxial tensile tests. Our findings indicate that the 1T-$MoTe_2$ phase exhibits greater vulnerability compared to the 2H-$MoTe_2$ phase, as its fracture initiation requires nearly half the critical strain observed in 2H-$MoTe_2$. Additionally, the fracture behavior of 1T-$MoTe_2$ results is brittle in nature, while 2H-$MoTe_2$ generates two distinct $MoTe_2$ fragments. These observations suggest that the layout of chalcogen atoms in the 1T phase significantly influences the structural stability of transition metal dichalcogenides (TMDs).

Our simulations also indicate that the disparity in fracture strains between 2H and 1T $MoTe_2$ is less pronounced when stretching is exerted along the zigzag direction. The brittle fracture behavior observed in 1T-$MoTe_2$ during armchair direction stretching is not observed when stretched in the zigzag direction. Moreover, the stress-strain plots for both 2H and 1T-$MoTe_2$ demonstrate a nonlinear elastic range that precedes the ultimate strength. Subsequently, there is a stress-free region beyond a critical fracture strain, during which the membranes undergo rupture. It is worth mentioning that the ultimate strength values exhibit a slight increase when the tensile stretching is directed along the zigzag axis. Notably, the ultimate strength values are slightly higher when the tensile stretching is applied in the zigzag direction.

It was further observed that an increase in temperature led to a reduction in the ultimate stress, Young modulus and fracture strain of the membrane. However, the elastic modulus does not vary with temperature. The armchair configuration of $MoTe_2$ is found to be stronger than the zigzag configuration, indicating that the $MoTe_2$ membrane is nearly isotropic in mechanical characteristics.

Based on our findings, it is evident that stress accumulates significantly around the hole location during tension, resulting in the rupture of atomic bonds as strain progressively increases. The concentration of stress at these points leads to a decrease in both the failure strain and ultimate strength of the porous sheets compared to those of the pristine sheet.

CHAPTER 5: CONCLUSION

5.1. Findings

In this research, the mechanical response of 2H and 1T $MoTe_2$ was explored through uniaxial and biaxial tensile tests conducted under different temperature conditions. Furthermore, the fracture behavior of these materials was analyzed by studying stress distribution and stress-strain curves. The obtained results suggest potential applications for both 2H and 1T $MoTe_2$ under diverse conditions.

1. The 1T-$MoTe_2$ phase exhibits significantly higher fragility compared to the 2H-$MoTe_2$ phase.
2. The critical strain at which fracture initiates in 1T-$MoTe_2$ is nearly twice as small as that in 2H-$MoTe_2$.
3. When 1T-$MoTe_2$ undergoes fracture, it exhibits brittleness, while 2H-$MoTe_2$ fractures into two separate $MoTe_2$ fragments with well-defined boundaries.
4. The structural stability of TMDs is greatly diminished by how the chalcogen atoms are arranged in the 1T phase.
5. When applying stretching in the zigzag direction, the disparity in fracture strains between 2H and 1T $MoTe_2$ is reduced.
6. Stretching 1T-$MoTe_2$ in the zigzag direction eliminates the brittle behavior observed during fracture, which is evident when stretched in the armchair direction.
7. Both 2H and 1T-$MoTe_2$ exhibit stress-strain curves characterized by a nonlinear elastic region extending up to the ultimate strength point. Beyond a critical fracture strain, a stress-free region occurs where the membranes undergo fracture.
8. The ultimate strength values show a slight improvement when the tensile stretching is performed along the zigzag direction.

9. An escalation in temperature leads to a decline in the ultimate stress, fracture strain and Young's modulus of the membrane.
10. The Elastic Modulus does not vary with temperature.
11. The armchair configuration of $MoTe_2$ is stronger than the zigzag configuration, suggesting near isotropy in its mechanical characteristics.
12. The outcomes imply that as the strain increases, stress becomes highly localized around the vacancy position during tension, causing the disruption of atomic bonds in that area. This stress concentration at the hole positions results in a reduction in the failure strain and ultimate strength of the porous sheets when compared to the defectless sheet.
13. In summary, this study reveals important insights into the fracture mechanics of 2H-$MoTe_2$ and 1T-$MoTe_2$ and provides a basis for further investigations into the mechanical properties of transition metal dichalcogenides.

To conclude, our research provides our study offers valuable perspectives on the mechanical characteristics of 2D $MoTe_2$ and the impact of defects on its behavior. The implications of these findings can contribute to the prediction of mechanical characteristics in TMDs for industrial applications, contributing to the development of advanced materials in various fields.

5.2. Future Recommendations

Based on the study of the mechanical properties of 2H and 1T $MoTe_2$, several promising future directions and areas of exploration can be identified. These include:

1. Investigation of band gap and band structures: Further research can be conducted to explore the impact of vacancy-induced defects on the band gap and band structures of $MoTe_2$. This will offer significant understanding into the electronic characteristics and possible utility of these materials.
2. Doping effects on fracture and electrical properties: The influence of doping on the fracture behavior and electrical properties of transition metal dichalcogenides (TMDs), including

$MoTe_2$, can be studied. This will help understand the role of dopants in modulating the mechanical and electrical characteristics of these materials, opening up possibilities for tailored applications.

3. Exploration of composite 2D heterostructures: The fracture points of composite 2D heterostructures, involving combinations of $MoTe_2$ with other 2D materials, can be investigated. This research can focus on understanding the mechanical properties, such as fracture toughness and interfacial strength, of these heterostructures, which will contribute to the design and fabrication of advanced 2D materials with enhanced mechanical performance.

4. Characterization of mechanical, thermal, and electronic properties of TMD nanowires: The mechanical, electronic and thermal properties of TMD nanowires, including $MoTe_2$ nanowires, can be comprehensively studied. This research can provide valuable insights into the unique properties and potential applications of TMD nanowires, such as nanoscale sensors and high-performance nanoelectronics.

5. Exploration of other TMD materials: Beyond $MoTe_2$, the properties of other TMD materials can be investigated. This includes studying the mechanical, thermal, and electronic characteristics of different TMDs, such as MoS_2, WS_2, and WSe_2. Understanding the diverse properties of TMD materials will expand the knowledge base and enable the development of a wider range of TMD-based devices and technologies.

REFERENCE

[1] S. H. Mir, V. K. Yadav, J. K. Singh, and J. K. Singh, "Recent Advances in the Carrier Mobility of Two-Dimensional Materials: A Theoretical Perspective," *ACS Omega*, vol. 5, no. 24. 2020. doi: 10.1021/acsomega.0c01676.

[2] D. Akinwande *et al.*, "A review on mechanics and mechanical properties of 2D materials—Graphene and beyond," *Extreme Mechanics Letters*, vol. 13. 2017. doi: 10.1016/j.eml.2017.01.008.

[3] Z. Xiong, L. Zhong, H. Wang, and X. Li, "Structural defects, mechanical behaviors and properties of two-dimensional materials," *Materials*, vol. 14, no. 5. 2021. doi: 10.3390/ma14051192.

[4] W. Choi, N. Choudhary, G. H. Han, J. Park, D. Akinwande, and Y. H. Lee, "Recent development of two-dimensional transition metal dichalcogenides and their applications," *Materials Today*, vol. 20, no. 3. Elsevier B.V., pp. 116–130, Apr. 01, 2017. doi: 10.1016/j.mattod.2016.10.002.

[5] S. A. Han, R. Bhatia, and S. W. Kim, "Synthesis, properties and potential applications of two-dimensional transition metal dichalcogenides," *Nano Convergence*, vol. 2, no. 1. 2015. doi: 10.1186/s40580-015-0048-4.

[6] K. Kim, J. Y. Choi, T. Kim, S. H. Cho, and H. J. Chung, "A role for graphene in silicon-based semiconductor devices," *Nature*, vol. 479, no. 7373. 2011. doi: 10.1038/nature10680.

[7] Alsema and M. J. E. De Wild-Scholten, "Reduction of the environmental impacts in crystalline silicon module manufacturing," *22nd Eur. Photovolt. Sol. Energy Conf.*, 2007.

[8] X. Duan, C. Wang, A. Pan, R. Yu, and X. Duan, "Two-dimensional transition metal dichalcogenides as atomically thin semiconductors: Opportunities and challenges," *Chemical Society Reviews*, vol. 44, no. 24. 2015. doi: 10.1039/c5cs00507h.

[9] E. Singh, K. S. Kim, G. Y. Yeom, and H. S. Nalwa, "Two-dimensional transition metal dichalcogenide-based counter electrodes for dye-sensitized solar cells," *RSC Advances*, vol. 7, no. 45. 2017. doi: 10.1039/c7ra03599c.

[10] Y. Tan *et al.*, "Controllable 2H-to-1T′ phase transition in few-layer $MoTe_2$," *Nanoscale*, vol. 10, no. 42, 2018, doi: 10.1039/c8nr06115g.

[11] Z. Wu and Z. Ni, "Spectroscopic investigation of defects in two-dimensional materials," *Nanophotonics*, vol. 6, no. 6. 2017. doi: 10.1515/nanoph-2016-0151.

[12] N. Khossossi, D. Singh, A. Ainane, and R. Ahuja, "Recent progress of defect chemistry on 2D materials for advanced battery anodes," *Chemistry - An Asian Journal*, vol. 15, no. 21. 2020. doi: 10.1002/asia.202000908.

[13] V. Sorkin, Q. X. Pei, and Y. W. Zhang, "Modelling of Defects and Failure in 2D Materials: Graphene and Beyond," in *Handbook of Materials Modeling*, 2018. doi: 10.1007/978-3-319-50257-1_45-1.

[14] K. Kumar Gupta, T. Mukhopadhyay, A. Roy, and S. Dey, "Probing the compound effect of spatially varying intrinsic defects and doping on mechanical properties of hybrid graphene monolayers," *J. Mater. Sci. Technol.*, vol. 50, 2020, doi: 10.1016/j.jmst.2020.03.004.

[15] S. Plimpton, "LAMMPS documentation," *... . cs. sandia. gov/~ sjplimp/lammps/doc/Manual. html*, 2007.

[16] M. Chhowalla, H. S. Shin, G. Eda, L. J. Li, K. P. Loh, and H. Zhang, "The chemistry of two-dimensional layered transition metal dichalcogenide nanosheets," *Nature Chemistry*, vol. 5, no. 4. 2013. doi: 10.1038/nchem.1589.

[17] B. Mortazavi, G. R. Berdiyorov, M. Makaremi, and T. Rabczuk, "Mechanical responses of two-dimensional $MoTe_2$; pristine 2H, 1T and 1T′ and 1T′/2H heterostructure," *Extrem. Mech. Lett.*, vol. 20, 2018, doi: 10.1016/j.eml.2018.01.005.

[18] Y. Wang *et al.*, "Structural phase transition in monolayer $MoTe_2$ driven by electrostatic doping," *Nature*, vol. 550, no. 7677, 2017, doi: 10.1038/nature24043.

[19] F. Ling *et al.*, "Enhancing hydrogen evolution on the basal plane of transition metal dichacolgenide van der Waals heterostructures," *npj Comput. Mater.*, vol. 5, no. 1, 2019, doi: 10.1038/s41524-019-0161-8.

[20] N. R. Pradhan *et al.*, "Hall and field-effect mobilities in few layered p-WSe_2 field-effect

transistors," *Sci. Rep.*, vol. 5, 2015, doi: 10.1038/srep08979.

[21] Y. F. Lin *et al.*, "Ambipolar $MoTe_2$ transistors and their applications in logic circuits," *Adv. Mater.*, vol. 26, no. 20, 2014, doi: 10.1002/adma.201305845.

[22] J. C. Park *et al.*, "Phase-Engineered Synthesis of Centimeter-Scale 1T′- and 2H-Molybdenum Ditelluride Thin Films," *ACS Nano*, vol. 9, no. 6, 2015, doi: 10.1021/acsnano.5b02511.

[23] W. Zhang, M. H. Chiu, C. H. Chen, W. Chen, L. J. Li, and A. T. S. Wee, "Role of metal contacts in high-performance phototransistors based on WSe2 monolayers," *ACS Nano*, vol. 8, no. 8, 2014, doi: 10.1021/nn503521c.

[24] S. Cho *et al.*, "Phase patterning for ohmic homojunction contact in $MoTe_2$," *Science (80-.).*, vol. 349, no. 6248, 2015, doi: 10.1126/science.aab3175.

[25] R. Kappera *et al.*, "Phase-engineered low-resistance contacts for ultrathin MoS_2 transistors," *Nat. Mater.*, vol. 13, no. 12, 2014, doi: 10.1038/nmat4080.

[26] K. A. N. Duerloo, Y. Li, and E. J. Reed, "Structural phase transitions in two-dimensional Mo-and W-dichalcogenide monolayers," *Nat. Commun.*, vol. 5, 2014, doi: 10.1038/ncomms5214.

[27] K. A. N. Duerloo and E. J. Reed, "Structural phase transitions by design in monolayer alloys," *ACS Nano*, vol. 10, no. 1, 2016, doi: 10.1021/acsnano.5b04359.

[28] Y. Li, K. A. N. Duerloo, K. Wauson, and E. J. Reed, "Structural semiconductor-to-semimetal phase transition in two-dimensional materials induced by electrostatic gating," *Nat. Commun.*, vol. 7, 2016, doi: 10.1038/ncomms10671.

[29] C. Zhang *et al.*, "Charge Mediated Reversible Metal-Insulator Transition in Monolayer $MoTe_2$ and $W_xMo_{1-x}Te_2$ Alloy," *ACS Nano*, vol. 10, no. 8, 2016, doi: 10.1021/acsnano.6b00148.

[30] X. Qian, J. Liu, L. Fu, and J. Li, "Quantum spin hall effect in two - Dimensional transition metal dichalcogenides," *Science (80-.).*, vol. 346, no. 6215, 2014, doi: 10.1126/science.1256815.

[31] D. H. Keum *et al.*, “Bandgap opening in few-layered monoclinic $MoTe_2$,” *Nat. Phys.*, vol. 11, no. 6, 2015, doi: 10.1038/nphys3314.

[32] A. A. Soluyanov *et al.*, “Type-II Weyl semimetals,” *Nat. 2015 5277579*, vol. 527, no. 7579, pp. 495–498, Nov. 2015, doi: 10.1038/nature15768.

[33] Y. Sun, S.-C. Wu, M. N. Ali, C. Felser, and B. Yan, “Prediction of Weyl semimetal in orthorhombic $MoTe_2$,” *Phys. Rev. B*, vol. 92, no. 16, 2015.

[34] Z. Wang *et al.*, “$MoTe_2$: A Type-II Weyl Topological Metal,” *Phys. Rev. Lett.*, vol. 117, no. 5, 2016, doi: 10.1103/PhysRevLett.117.056805.

[35] H. Weng, C. Fang, Z. Fang, B. Andrei Bernevig, and X. Dai, “Weyl semimetal phase in noncentrosymmetric transition-metal monophosphides,” *Phys. Rev. X*, vol. 5, no. 1, 2015, doi: 10.1103/PhysRevX.5.011029.

[36] S. Y. Xu *et al.*, “Discovery of a Weyl fermion semimetal and topological Fermi arcs,” *Science (80-.).*, vol. 349, no. 6248, 2015, doi: 10.1126/science.aaa9297.

[37] G. Bian *et al.*, “Topological nodal-line fermions in spin-orbit metal $PbTaSe_2$,” *Nat. Commun.*, vol. 7, 2016, doi: 10.1038/ncomms10556.

[38] L. Huang *et al.*, “Spectroscopic evidence for a type II Weyl semimetallic state in $MoTe_2$,” *Nat. Mater.*, vol. 15, no. 11, 2016, doi: 10.1038/nmat4685.

[39] X. Xu *et al.*, “Millimeter-Scale Single-Crystalline Semiconducting $MoTe_2$ via Solid-to-Solid Phase Transformation,” *J. Am. Chem. Soc.*, vol. 141, no. 5, 2019, doi: 10.1021/jacs.8b12230.

[40] W. Hou *et al.*, “Strain-based room-temperature non-volatile $MoTe_2$ ferroelectric phase change transistor,” *Nat. Nanotechnol.*, vol. 14, no. 7, 2019, doi: 10.1038/s41565-019-0466-2.

[41] G. Y. Bae, J. Kim, J. Kim, S. Lee, and E. Lee, “$MoTe_2$ field-effect transistors with low contact resistance through phase tuning by laser irradiation,” *Nanomaterials*, vol. 11, no. 11, 2021, doi: 10.3390/nano11112805.

[42] N. R. Pradhan *et al.*, “Field-effect transistors based on few-layered α-$MoTe_2$,” *ACS Nano*,

vol. 8, no. 6, 2014, doi: 10.1021/nn501013c.

[43] C. Ruppert, O. B. Aslan, and T. F. Heinz, "Optical properties and band gap of single- and few-layer $MoTe_2$ crystals," *Nano Lett.*, vol. 14, no. 11, 2014, doi: 10.1021/nl502557g.

[44] M. Zhu, W. Luo, N. Wu, X. A. Zhang, and S. Qin, "Engineering few-layer $MoTe_2$ devices by Co/hBN tunnel contacts," *Appl. Phys. Lett.*, vol. 112, no. 18, 2018, doi: 10.1063/1.5027586.

[45] Q. Li *et al.*, "Sub-5 nm Gate Length Monolayer $MoTe_2$ Transistors," *J. Phys. Chem. C*, vol. 125, no. 35, 2021, doi: 10.1021/acs.jpcc.1c01754.

[46] D. J. Frank, R. H. Dennard, E. Nowak, P. M. Solomon, Y. Taur, and H. S. P. Wong, "Device scaling limits of Si MOSFETs and their application dependencies," *Proc. IEEE*, vol. 89, no. 3, 2001, doi: 10.1109/5.915374.

[47] J. M. Pimbley and J. D. Meindl, "MOSFET Scaling Limits Determined by Subthreshold Conduction," *IEEE Trans. Electron Devices*, vol. 36, no. 9, 1989, doi: 10.1109/16.34233.

[48] R. Kappera *et al.*, "Metallic 1T phase source/drain electrodes for field effect transistors from chemical vapor deposited MoS_2," *APL Mater.*, vol. 2, no. 9, 2014, doi: 10.1063/1.4896077.

[49] S. Song, D. H. Keum, S. Cho, D. Perello, Y. Kim, and Y. H. Lee, "Room Temperature Semiconductor-Metal Transition of $MoTe_2$ Thin Films Engineered by Strain," *Nano Lett.*, vol. 16, no. 1, 2016, doi: 10.1021/acs.nanolett.5b03481.

[50] N. A. Pertsev, A. G. Zembilgotov, and A. K. Tagantsev, "Effect of Mechanical Boundary Conditions on Phase Diagrams of Epitaxial Ferroelectric Thin Films," *Phys. Rev. Lett.*, vol. 80, no. 9, 1998, doi: 10.1103/PhysRevLett.80.1988.

[51] J. H. Haeni *et al.*, "Room-temperature ferroelectricity in strained $SrTiO_3$," *Nature*, vol. 430, no. 7001, 2004, doi: 10.1038/nature02773.

[52] J. Cao *et al.*, "Strain engineering and one-dimensional organization of metal-insulator domains in single-crystal vanadium dioxide beams," *Nat. Nanotechnol.*, vol. 4, no. 11, 2009, doi: 10.1038/nnano.2009.266.

[53] H. Takahashi, K. Igawa, K. Arii, Y. Kamihara, M. Hirano, and H. Hosono,

"Superconductivity at 43 K in an iron-based layered compound $LaO_{1-x}F_xFeAs$," *Nature*, vol. 453, no. 7193, 2008, doi: 10.1038/nature06972.

[54] L. Gao *et al.*, "Superconductivity up to 164 K in $HgBa_2Ca_{m-1}Cu_mO_{2m+2+\delta}$ (m=1, 2, and 3) under quasihydrostatic pressures," *Phys. Rev. B*, vol. 50, no. 6, 1994, doi: 10.1103/PhysRevB.50.4260.

[55] Y. Wang, X. Ren, K. Otsuka, and A. Saxena, "Temperature-stress phase diagram of strain glass $Ti_{48.5}Ni_{51.5}$," *Acta Mater.*, vol. 56, no. 12, 2008, doi: 10.1016/j.actamat.2008.02.032.

[56] P. May, U. Khan, and J. N. Coleman, "Reinforcement of metal with liquid-exfoliated inorganic nano-platelets," *Appl. Phys. Lett.*, vol. 103, no. 16, 2013, doi: 10.1063/1.4825279.

[57] B. R. Rano, I. M. Syed, and S. H. Naqib, "Ab initio approach to the elastic, electronic, and optical properties of $MoTe_2$ topological Weyl semimetal," *J. Alloys Compd.*, vol. 829, 2020, doi: 10.1016/j.jallcom.2020.154522.

[58] Y. Sun *et al.*, "Elastic Properties and Fracture Behaviors of Biaxially Deformed, Polymorphic $MoTe_2$," *Nano Lett.*, vol. 19, no. 2, 2019, doi: 10.1021/acs.nanolett.8b03833.

[59] D. ÇakIr, F. M. Peeters, and C. Sevik, "Mechanical and thermal properties of h -MX_2 (M = Cr, Mo, W; X = O, S, Se, Te) monolayers: A comparative study," *Appl. Phys. Lett.*, vol. 104, no. 20, 2014, doi: 10.1063/1.4879543.

[60] J. Li, N. V. Medhekar, and V. B. Shenoy, "Bonding charge density and ultimate strength of monolayer transition metal dichalcogenides," *J. Phys. Chem. C*, vol. 117, no. 30, 2013, doi: 10.1021/jp403986v.

[61] M. K. Jana *et al.*, "A combined experimental and theoretical study of the structural, electronic and vibrational properties of bulk and few-layer Td-WTe_2," *J. Phys. Condens. Matter*, vol. 27, no. 28, 2015, doi: 10.1088/0953-8984/27/28/285401.

[62] *Handbook of Stillinger-Weber Potential Parameters for Two-Dimensional Atomic Crystals*. 2017. doi: 10.5772/intechopen.71767.

[63] M. L. Pereira Júnior *et al.*, "On the elastic properties and fracture patterns of MoX_2 (X = S, Se, Te) membranes: A reactive molecular dynamics study," *Condens. Matter*, vol. 5, no. 4,

2020, doi: 10.3390/condmat5040073.

[64] S. A. Chowdhury *et al.*, “Mechanical Properties and Strain Transfer Behavior of Molybdenum Ditelluride ($MoTe_2$) Thin Films,” *J. Eng. Mater. Technol.*, vol. 144, no. 1, 2022, doi: 10.1115/1.4051306.

[65] S. Shao, H. M. Zbib, I. Mastorakos, and D. F. Bahr, “Effect of interfaces in the work hardening of nanoscale multilayer metallic composites during nanoindentation: A molecular dynamics investigation,” *J. Eng. Mater. Technol.*, vol. 135, no. 2, 2013, doi: 10.1115/1.4023672.

[66] J. W. Jiang and H. S. Park, “Mechanical properties of MoS_2/graphene heterostructures,” *Appl. Phys. Lett.*, vol. 105, no. 3, 2014, doi: 10.1063/1.4891342.

[67] F. Ma, Y. J. Sun, D. Y. Ma, K. W. Xu, and P. K. Chu, “Reversible phase transformation in graphene nano-ribbons: Lattice shearing based mechanism,” *Acta Mater.*, vol. 59, no. 17, 2011, doi: 10.1016/j.actamat.2011.07.036.

[68] F. H. Stillinger and T. A. Weber, “Computer simulation of local order in condensed phases of silicon,” *Phys. Rev. B*, vol. 31, no. 8, 1985, doi: 10.1103/PhysRevB.31.5262.

[69] T. Liang, S. R. Phillpot, and S. B. Sinnott, “Parametrization of a reactive many-body potential for Mo-S systems,” *Phys. Rev. B - Condens. Matter Mater. Phys.*, vol. 79, no. 24, 2009, doi: 10.1103/PhysRevB.79.245110.

[70] J. Tersoff, “Modeling solid-state chemistry: Interatomic potentials for multicomponent systems,” *Phys. Rev. B*, vol. 39, no. 8, 1989, doi: 10.1103/PhysRevB.39.5566.

[71] M. Z. Hossain, T. Hao, and B. Silverman, “Stillinger-Weber potential for elastic and fracture properties in graphene and carbon nanotubes,” *J. Phys. Condens. Matter*, vol. 30, no. 5, 2018, doi: 10.1088/1361-648X/aaa3cc.

[72] K. Burke, “Perspective on density functional theory,” *J. Chem. Phys.*, vol. 136, no. 15, 2012, doi: 10.1063/1.4704546.

[73] A. J. Cohen, P. Mori-Sánchez, and W. Yang, “Insights into current limitations of density functional theory,” *Science*, vol. 321, no. 5890. 2008. doi: 10.1126/science.1158722.

[74] P. and W. K. Hohenberg, “Inhomogeneous Electron Gas. Physical Review,” *Am. Phys. Soc.*, vol. 136(3B), no. p. B864-B871., 1964.

[75] M. K. Harbola and V. Sahni, “Quantum-mechanical interpretation of the exchange-correlation potential of kohn-sham density-functional theory,” *Phys. Rev. Lett.*, vol. 62, no. 5, 1989, doi: 10.1103/PhysRevLett.62.489.

[76] G. E. W. Bauer, “General operator ground-state expectation values in the Hohenberg-Kohn-Sham density-functional formalism,” *Phys. Rev. B*, vol. 27, no. 10, 1983, doi: 10.1103/PhysRevB.27.5912.

[77] S. Alavi, “Statistical Mechanics: Theory and Molecular Simulation. By Mark E. Tuckerman.,” *Angew. Chemie Int. Ed.*, vol. 50, no. 51, 2011, doi: 10.1002/anie.201105752.

[78] A. Rahman, “Correlations in the motion of atoms in liquid argon,” *Phys. Rev.*, vol. 136, no. 2A, 1964, doi: 10.1103/PhysRev.136.A405.

[79] M. Born, K. Huang, and M. Lax, “Dynamical Theory of Crystal Lattices,” *Am. J. Phys.*, vol. 23, no. 7, 1955, doi: 10.1119/1.1934059.

[80] T. Luo and J. R. Lloyd, “Equilibrium molecular dynamics study of lattice thermal conductivity/conductance of Au-SAM-Au junctions,” *J. Heat Transfer*, vol. 132, no. 3, 2010, doi: 10.1115/1.4000047.

[81] R. M. Betz and R. C. Walker, “Paramfit: Automated optimization of force field parameters for molecular dynamics simulations,” *J. Comput. Chem.*, vol. 36, no. 2, 2015, doi: 10.1002/jcc.23775.

[82] S. L. Mayo, B. D. Olafson, and W. A. Goddard, “DREIDING: A generic force field for molecular simulations,” *J. Phys. Chem.*, vol. 94, no. 26, 1990, doi: 10.1021/j100389a010.

[83] A. K. Rappé, C. J. Casewit, K. S. Colwell, W. A. Goddard, and W. M. Skiff, “UFF, a Full Periodic Table Force Field for Molecular Mechanics and Molecular Dynamics Simulations,” *J. Am. Chem. Soc.*, vol. 114, no. 25, 1992, doi: 10.1021/ja00051a040.

[84] A. D. MacKerell *et al.*, “All-atom empirical potential for molecular modeling and dynamics studies of proteins,” *J. Phys. Chem. B*, vol. 102, no. 18, 1998, doi: 10.1021/jp973084f.

[85] W. D. Cornell *et al.*, " A Second Generation Force Field for the Simulation of Proteins, Nucleic Acids, and Organic Molecules J . Am . Chem . Soc . 1995 , 117 , 5179−5197 ," *J. Am. Chem. Soc.*, vol. 118, no. 9, 1996, doi: 10.1021/ja955032e.

[86] C. Oostenbrink, A. Villa, A. E. Mark, and W. F. Van Gunsteren, "A biomolecular force field based on the free enthalpy of hydration and solvation: The GROMOS force-field parameter sets 53A5 and 53A6," *J. Comput. Chem.*, vol. 25, no. 13, 2004, doi: 10.1002/jcc.20090.

[87] W. L. Jorgensen, D. S. Maxwell, and J. Tirado-Rives, "Development and testing of the OPLS all-atom force field on conformational energetics and properties of organic liquids," *J. Am. Chem. Soc.*, vol. 118, no. 45, 1996, doi: 10.1021/ja9621760.

[88] H. Sun, "Compass: An ab initio force-field optimized for condensed-phase applications - Overview with details on alkane and benzene compounds," *J. Phys. Chem. B*, vol. 102, no. 38, 1998, doi: 10.1021/jp980939v.

[89] J.-W. Jiang and Y.-P. Zhou, "Parameterization of Stillinger-Weber Potential for Two-Dimensional Atomic Crystals," in *Handbook of Stillinger-Weber Potential Parameters for Two-Dimensional Atomic Crystals*, InTech, 2017. doi: 10.5772/intechopen.71929.

[90] Y. Y. Zhang, Q. X. Pei, J. W. Jiang, N. Wei, and Y. W. Zhang, "Thermal conductivities of single- and multi-layer phosphorene: A molecular dynamics study," *Nanoscale*, vol. 8, no. 1, 2016, doi: 10.1039/c5nr05451f.

[91] M. Ghorbani-Asl, A. N. Enyashin, A. Kuc, G. Seifert, and T. Heine, "Defect-induced conductivity anisotropy in MoS 2 monolayers," *Phys. Rev. B - Condens. Matter Mater. Phys.*, vol. 88, no. 24, 2013, doi: 10.1103/PhysRevB.88.245440.

[92] S. Ippolito and P. Samorì, "Defect Engineering Strategies Toward Controlled Functionalization of Solution-Processed Transition Metal Dichalcogenides," *Small Sci.*, vol. 2, no. 4, 2022, doi: 10.1002/smsc.202100122.

[93] R. Addou, L. Colombo, and R. M. Wallace, "Surface Defects on Natural MoS_2," *ACS Appl. Mater. Interfaces*, vol. 7, no. 22, 2015, doi: 10.1021/acsami.5b01778.

[94] F. Cleri, S. R. Phillpot, D. Wolf, and S. Yip, "Atomistic simulations of materials fracture

and the link between atomic and continuum length scales," *J. Am. Ceram. Soc.*, vol. 81, no. 3, 1998, doi: 10.1111/j.1151-2916.1998.tb02368.x.

[95] R. A. S. I. Subad, T. S. Akash, P. Bose, and M. M. Islam, "Engineered defects to modulate fracture strength of single layer MoS_2: An atomistic study," *Phys. B Condens. Matter*, vol. 592, no. October 2019, p. 412219, Sep. 2020, doi: 10.1016/j.physb.2020.412219.

[96] T. Sun *et al.*, "Defect chemistry in 2D materials for electrocatalysis," *Materials Today Energy*, vol. 12. 2019. doi: 10.1016/j.mtener.2019.01.004.

[97] T. Wang, J. Li, H. Jin, and Y. Wei, "Tuning the electronic and magnetic properties of InSe nanosheets by transition metal doping," *Phys. Chem. Chem. Phys.*, vol. 20, no. 11, 2018, doi: 10.1039/c8cp00219c.

[98] N. Zhang and M. Asle Zaeem, "Role of grain boundaries in determining strength and plastic deformation of yttria-stabilized tetragonal zirconia bicrystals," *J. Mater. Sci.*, vol. 53, no. 8, 2018, doi: 10.1007/s10853-017-1595-3.

[99] S. J. Plimpton and C. Knight, "Rendezvous algorithms for large-scale modeling and simulation," *J. Parallel Distrib. Comput.*, vol. 147, pp. 184–195, Jan. 2021, doi: 10.1016/J.JPDC.2020.09.001.

[100] A. Stukowski, "Visualization and analysis of atomistic simulation data with OVITO-the Open Visualization Tool," *Model. Simul. Mater. Sci. Eng.*, vol. 18, no. 1, 2010, doi: 10.1088/0965-0393/18/1/015012.

[101] T. Li, "Ideal strength and phonon instability in single-layer MoS_2," *Phys. Rev. B*, vol. 85, no. 23, p. 235407, Jun. 2012, doi: 10.1103/PhysRevB.85.235407.

[102] M. M. Islam *et al.*, "ReaxFF molecular dynamics simulations on lithiated sulfur cathode materials," *Phys. Chem. Chem. Phys.*, vol. 17, no. 5, pp. 3383–3393, 2015, doi: 10.1039/C4CP04532G.

[103] L. Yu, Q. Yan, and A. Ruzsinszky, "Negative Poisson's ratio in 1T-type crystalline two-dimensional transition metal dichalcogenides," *Nat. Commun.*, vol. 8, 2017, doi: 10.1038/ncomms15224.

[104] H. Jin *et al.*, “Emerging Two-Dimensional Nanomaterials for Electrocatalysis,” *Chemical Reviews*, vol. 118, no. 13. 2018. doi: 10.1021/acs.chemrev.7b00689.

[105] J.-W. Jiang, “Parametrization of Stillinger–Weber potential based on valence force field model: application to single-layer MoS_2 and black phosphorus,” *Nanotechnology*, vol. 26, no. 31, p. 315706, Jul. 2015, doi: 10.1088/0957-4484/26/31/315706.

turnitin

Similarity Report ID: oid:22779:36786720

PAPER NAME

Thesis Draft Final 2_180011216.docx

WORD COUNT	CHARACTER COUNT
22210 Words	**124752 Characters**
PAGE COUNT	FILE SIZE
129 Pages	**18.2MB**
SUBMISSION DATE	REPORT DATE
Jun 4, 2023 1:20 AM GMT+6	**Jun 4, 2023 1:22 AM GMT+6**

19% Overall Similarity

The combined total of all matches, including overlapping sources, for each database.

- 14% Internet database
- 14% Publications database
- Crossref database
- Crossref Posted Content database
- 12% Submitted Works database

Excluded from Similarity Report

- Bibliographic material